

FROST-CLUSTERS – III. Metallicity-dependent intermediate mass black hole formation by runaway collisions in dense star clusters

Antti Rantala^{1,2,3}*, Thorsten Naab¹, Natalia Lahén^{1,4}, Klaus Reuter⁵, Markus Rampp⁵, Martyna Chruścińska⁶, Bastián Reinoso⁷

¹Max-Planck-Institut für Astrophysik, Karl-Schwarzschild-Str. 1, D-85748, Garching, Germany

²Institute of Astronomy, University of Cambridge, Madingley Road, Cambridge CB3 0HA, UK

³Kavli Institute for Cosmology, Cambridge (KICC), University of Cambridge, Madingley Road, Cambridge CB3 0HA, UK

⁴Zentrum für Astronomie der Universität Heidelberg, Astronomisches Rechen-Institut, Mönchhofstr. 12–14, D-69120 Heidelberg

⁵Max Planck Computing and Data Facility (MPCDF), D-85748, Garching, Germany

⁶European Southern Observatory, Karl-Schwarzschild-Str. 2, D-85748 Garching, Germany

⁷Department of Physics, University of Helsinki, P.O. Box 64, Gustaf Hällströmin katu 2, FI-00014, University of Helsinki, Finland

Accepted XXX. Received YYY; in original form ZZZ

ABSTRACT

We explore the formation of intermediate mass black holes (IMBHs), potential seeds for supermassive black holes (SMBHs), via runaway stellar collisions for a wide range of star cluster (surface) densities ($4 \times 10^3 M_\odot \text{ pc}^{-2} \lesssim \Sigma_h \lesssim 4 \times 10^6 M_\odot \text{ pc}^{-2}$) and metallicities ($0.01 Z_\odot \lesssim Z \lesssim 1.0 Z_\odot$). Our sample of isolated (> 1400) and hierarchical (30) simulations of young, massive star clusters with up to $N = 1.8 \times 10^6$ stars includes collisional stellar dynamics, stellar evolution, and post-Newtonian equations of motion for black holes using the BIFROST code. High stellar wind rates suppress IMBH formation at high metallicities ($Z \gtrsim 0.2 Z_\odot$) and low collision rates prevent their formation at low densities ($\Sigma_h \lesssim 3 \times 10^4 M_\odot \text{ pc}^{-2}$). The assumptions about stellar wind loss rates strongly affect the maximum final IMBH masses ($M_\bullet \sim 6000 M_\odot$ vs. $25000 M_\odot$). The total stellar mass loss from collisions and collisionally boosted winds before $t = 3$ Myr can together reach up to 5–10% of the final cluster mass. We present fitting formulae for IMBH masses as a function of host star cluster Σ_h and Z , and formulate a model for the cosmic IMBH formation rate density. Depending on the cluster birth densities, the IMBH formation rates peak at $z \sim 2$ –4 at up to $\sim 10^{-7} \text{ yr}^{-1} \text{ cMpc}^{-3}$. As more than 50% form below $z \lesssim 1.5$ –3, the model challenges a view in which all local IMBHs are failed early Universe SMBH seeds.

Key words: gravitation – celestial mechanics – methods: numerical – galaxies: star clusters: general – stars: black holes

1 INTRODUCTION

The origin of supermassive black holes (SMBHs; $M_\bullet \geq 10^6 M_\odot$) remains a major unsolved puzzle in modern astrophysics (Rees 1984; Inayoshi et al. 2020; Volonteri et al. 2021). Recently, the *James Webb Space Telescope* (*JWST*) observations of active galactic nuclei (AGN) powered by accreting SMBHs at redshifts above $z \gtrsim 6$ –10 (Maiolino et al. 2024a,b; Juodžbalis et al. 2024; Scholtz et al. 2024; Übler et al. 2024) have only deepened the conundrum of the SMBH origins. The majority of theoretical SMBH seed formation scenarios (Pop-III stars, direct collapse clouds, runaway Pop-II col-

lisions) rely on the low metallicity environments of the high redshift ($z > 10$) galaxies. Primordial Pop-III stars can only occur at metallicities below $Z \lesssim 10^{-4} Z_\odot$ (Bromm et al. 2001), direct collapse gas clouds require low metallicities to avoid fragmentation (e.g. Regan et al. 2017) while massive stars built up by runaway Pop-II stellar collisions (Portegies Zwart et al. 2004) must avoid high wind loss rates (e.g. Mapelli 2016) to produce a massive black hole remnant. In most SMBH and galaxy stellar mass build up scenarios, possibly excluding primordial black holes (Dayal & Maiolino 2025), the galaxies themselves are expected to become metal enriched (e.g. Tassis et al. 2012) during their assembly. From this point of view, the recently observed near pristine *JWST* SMBH host galaxies (Maiolino et al. 2025; Juodžbalis et al. 2025) appear especially puz-

* E-mail: anttiran@mpa-garching.mpg.de

zling. Nevertheless, it is not uncommon for the early ($6 \lesssim z \lesssim 11$) *JWST* AGN and galaxies to show metallicities of $Z \sim 0.10 Z_{\odot}$ or even higher (Bunker et al. 2023; Isobe et al. 2023). The observed nitrogen enrichment at low metallicities and high star formation densities of the early *JWST* galaxies and AGN (e.g. Bunker et al. 2023; Cameron et al. 2023; Ji et al. 2024; Schaefer et al. 2024; Isobe et al. 2025; Ji et al. 2025; Naidu et al. 2025) may point to dense low-metallicity environments in which stellar collisions can frequently occur (Gieles et al. 2018; Charbonnel et al. 2023; Marques-Chaves et al. 2024; Schaefer et al. 2025; Ebihara et al. 2026), indicating the stellar collisional picture for the SMBH seed formation may be indeed feasible for at least a subset of early galaxies. Moreover, archaeological studies of the initial build-up phase of the Milky Way suggest highly clumpy and clustered formation environments for the early low metallicity ($[\text{Fe}/\text{H}] < -1.3$) stars of our Galaxy (Belokurov & Kravtsov 2022).

While especially common during the first gigayear, clumpy low metallicity star formation (Adamo et al. 2024; Fujimoto et al. 2024; Mowla et al. 2024; Bradač et al. 2025; Abdurro'uf et al. 2025; Yanagisawa et al. 2026, see also e.g. van Donkelaar et al. 2026) is not restricted to the redshift $z > 6$ Universe (Claeysens et al. 2025). Giant star forming clumps have been observed to be very common in more evolved massive gas-rich disk galaxies around cosmic noon at redshifts $1 \lesssim z \lesssim 3$ (e.g. Elmegreen & Elmegreen 2005; Genzel et al. 2008; Elmegreen et al. 2009; Genzel et al. 2011). Cosmological simulations suggest that 20% of the stars with metallicities $Z < 0.10 Z_{\odot}$ have formed since $z = 2$ (Pakmor et al. 2022). However, for $Z < 0.01 Z_{\odot}$ the fraction is considerably lower, only 3%. In general, the simulation models are in broad agreement with observation-based frameworks (e.g. Chruścińska & Nelemans 2019). Recent observation-based models (Chruścińska et al. 2024, 2025) indicate that up to $\sim 6\text{--}60\%$ of the total stellar mass formed at low metallicities below $Z < 0.1 Z_{\odot}$ since $z = 10$. The relatively large model uncertainties originate from the ambiguities in the absolute metallicity scale, the evolution in the star formation–mass relation and the low-mass end of the galaxy mass function. In any case the overall fraction of extremely low metallicity stars ($Z \lesssim 0.01 Z_{\odot}$) is less than $< 5\%$.

Today, the star cluster population of the Milky Way and the Magellanic clouds consists of two broad sub-populations. Ancient (> 10 Gyr) globular clusters (GCs) show very low metallicities below $Z \lesssim 0.04 Z_{\odot}$ while young massive star clusters (YMCs) with ages less than 1 Gyr show a higher and somewhat broader metallicity distribution in the range of $0.10 Z_{\odot} \lesssim Z \lesssim 1.0 Z_{\odot}$ (e.g. Mackey & Gilmore 2003). The local star clusters follow a relatively shallow mass-radius relation (Brown & Gnedin 2021) while older clusters typically show extended sizes compared to their recently formed counterparts (Portegies Zwart et al. 2010) attributed to internal and tidally driven star cluster evolution. However, the typical present-day stellar (surface) densities of the local YMCs are several orders of magnitude lower than in the $z \sim 10$ *JWST* proto GC star clusters (Adamo et al. 2024; Abdurro'uf et al. 2025) that can reach surface densities of $\Sigma_h \gtrsim 10^5 M_{\odot} \text{ pc}^{-2}$. Despite their relatively low densities, the local YMCs contain some of the most massive known individual stars: the R136 star cluster in the Large Magellanic Cloud (LMC) with a half mass surface density of $\Sigma_h \sim 3.6 \times 10^2 M_{\odot} \text{ pc}^{-2}$ (McLaughlin & van der Marel 2005) at $Z \sim 0.5 Z_{\odot}$ hosts several very massive stars with masses likely above $\gtrsim 150 M_{\odot}$ (Crowther et al. 2010).

Metallicity plays a defining role in stellar physics due to its interconnected effects on stellar nuclear reaction pathways, gas opacities and wind loss rates (e.g. Kippenhahn et al. 2013). Consequently,

metallicity has a major impact on the astrophysics of star clusters and black hole remnant formation as well. The earliest metal-free Pop-III star formation might have produced light SMBH seeds (Madau & Rees 2001; Schneider et al. 2002) from early stellar populations with a top-heavy or even logarithmically flat initial mass function (IMF; Marks et al. 2012; Chon et al. 2022) and very weak winds (Mujres et al. 2012). For the metal-enriched Pop-II stellar population, the properties of the compact remnant mass function depend on the metallicity of the stars (Fryer & Kalogera 2001; Fryer et al. 2012) with more massive stellar black holes (BHs) forming at low metallicities (Belczynski et al. 2010; Spera & Mapelli 2017; Belczynski & Banerjee 2020; Dorozsmai & Toonen 2024). This directly results in the formation of more massive BH-BH binaries in low metallicity stellar populations (Mapelli et al. 2013; Ziosi et al. 2014; Chatterjee et al. 2017; Cao et al. 2018; Giacobbo & Mapelli 2018; Giacobbo et al. 2018; Di Carlo et al. 2020b). Thus, gravitational wave (GW) observations of merging BHs with component masses $> 30 M_{\odot}$ suggest that their stellar progenitors may have formed in low metallicity environments. Together with low measured redshifts of a number of massive GW events, such as GW150914 and GW170104 ($z \sim 0.1\text{--}0.2$), the GW events imply either ongoing low metallicity star formation at low redshifts, long delay times for BH-BH mergers or their hierarchical dynamical assembly (Abbott et al. 2017). The GW merger population properties may also evolve with redshift (e.g. Rinaldi et al. 2024), which, if confirmed with future data, would suggest a metallicity trend or contribution from multiple channels for stellar BH-BH mergers.

Besides individual stars and stellar binaries, metallicity can affect the global evolution of entire star clusters as well (Chattopadhyay et al. 2022). If the cluster core collapse timescale t_{cc} exceeds the lifetimes of massive stars ($t_{\text{life}} \lesssim 3$ Myr), the post core collapse bounce is weaker at low metallicities (Mapelli & Bressan 2013). This is due to the lower wind mass losses, and results in somewhat higher central post collapse densities of the low metallicity clusters. In initially denser clusters, t_{cc} may be shorter than t_{life} , promoting stronger dynamical interactions, and heating of the cluster core by more massive metal-poor stars that have experienced weaker wind losses (Trani et al. 2014).

Analytic arguments, cluster Monte Carlo models (Hénon 1971) and direct N -body simulations (Aarseth 2003; Spurzem & Kamlah 2023) have demonstrated that massive star clusters ($M_{\text{cl}} \gtrsim 10^4 M_{\odot}$) that have half mass surface densities above $\Sigma_h \gtrsim 10^4 M_{\odot} \text{ pc}^{-2} - 10^5 M_{\odot} \text{ pc}^{-2}$ and low metallicities ($Z \lesssim 0.1 Z_{\odot}$) can build up increasingly massive stars by stellar collisions (Portegies Zwart et al. 1999; Miller & Hamilton 2002; Portegies Zwart et al. 2004; Fregeau et al. 2004; Gürkan et al. 2004; Freitag et al. 2006; Goswami et al. 2012; Fujii & Portegies Zwart 2013; Mapelli 2016; Reinoso et al. 2018; Rizzato et al. 2021; González Prieto et al. 2022; Arca Sedda et al. 2024; Rantala et al. 2024; Barber & Antonini 2025; Ugolini 2025; Vergara et al. 2025a). Following the massive star taxonomy of Gieles et al. (2025), we use the following classification of collisionally grown stars: very massive stars: (VMSs; $100 M_{\odot} \lesssim m_{\star} \lesssim 1000 M_{\odot}$), extremely massive stars (EMSs; $1000 M_{\odot} \lesssim m_{\star} \lesssim 10000 M_{\odot}$ and finally supermassive stars (SMSs; $m_{\star} \gtrsim 10000 M_{\odot}$). Numerical simulations indicate that the final mass of the collisionally grown stars sensitively depends on the mass, density, rotation, virial state and degree of fractality of its host cluster as well as its stellar population including the IMF, metallicity and binary fraction. In addition, gas likely plays a role in the collisional growth process as well (e.g. Reinoso et al. 2023; Fujii et al. 2024; Lahén et al. 2025a).

At the end of their lives, massive stars, formed either through

single-star evolution or via collision cascades, may collapse into massive stellar black holes (Di Carlo et al. 2020a; Kremer et al. 2020; Costa et al. 2022) in the pulsational pair-instability ((P)PISN) mass gap ($50\text{--}70 M_{\odot} \lesssim M_{\bullet} \lesssim 130\text{--}160 M_{\odot}$; Woosley & Heger 2021) or above it as intermediate-mass black holes (IMBHs; Greene et al. 2020; $10^2 M_{\odot} \lesssim M_{\bullet} \lesssim 10^5 M_{\odot}$). However, considerable uncertainties surround modelling the collisions and winds of VMSs and especially EMSs and SMSs. For a number of wind loss prescriptions the stellar mass loss rates can be high even at low metallicities, which may have an impact on the later evolution of the massive stars (e.g. Sabhahit et al. 2023; Shepherd et al. 2025; Simonato et al. 2025; Torniamenti et al. 2025). In the extreme case very high wind mass loss rates might inhibit the runaway stellar collisional IMBH formation channel altogether (Belkus et al. 2007; Yungelson et al. 2008; Glebbeek et al. 2009; Pauldrach et al. 2012). In addition, especially extended and weakly bound EMSs and SMSs might suffer from catastrophic mass loss in a subset of stellar collisions (Ramírez-Galeano et al. 2025) that result in net mass loss, not growth, in the collisions.

Even though theoretical arguments suggest that SMS formation could be possible up to $Z \sim 0.01 Z_{\odot}$ (Nandal & Chon 2025), thus far no supermassive star candidates have been observed in the local Universe (Kuruvanthodi et al. 2023). Similarly, despite a growing number of (P)PISN candidates (e.g. Schulze et al. 2024), none of them are thus far unambiguous (P)PISN events (Angus et al. 2024). Notwithstanding substantial observational effort (Gebhardt et al. 2002; Ibata et al. 2009; Noyola et al. 2010; van der Marel & Anderson 2010; Lützgendorf et al. 2011; Jalali et al. 2012; Lanzoni et al. 2013; Kamann et al. 2016; Baumgardt 2017; Pechetti et al. 2022; Della Croce et al. 2024), IMBHs in bona fide GCs of the Local Group also remain elusive. The strongest IMBH candidate thus far (Häberle et al. 2024) is located at the centre of ω Centauri, a likely stripped nucleus of a dwarf galaxy (e.g. Lee et al. 1999; Bekki & Freeman 2003). This dynamically detected IMBH candidate with $M_{\bullet} > 8200 M_{\odot}$ lies in the mass range of the inferred IMBH population in X-ray selected AGN in dwarf galaxies (Greene & Ho 2007; Dong et al. 2012; Chilingarian et al. 2018; Mezcua et al. 2018; Greene et al. 2020; Reines 2022) and overlaps the proposed mass range of $200 M_{\odot} \lesssim M_{\bullet} \lesssim 10^5 M_{\odot}$ of IMBHs (Colbert & Mushotzky 1999; Kaaret et al. 2001; Matsumoto et al. 2001; Strohmayer & Mushotzky 2003; Patruno et al. 2006; Farrell et al. 2009; Mezcua et al. 2013; Pasham et al. 2014; Mezcua et al. 2015; Kim et al. 2020) in ultra or hyper-luminous X-ray emitters (ULXs, HLXs).

Supporting the electromagnetic searches for IMBHs, ground-based gravitational wave observations with *Laser Interferometer Gravitational-Wave Observatory (LIGO)*, Virgo and *Kamioka Gravitational Wave Detector (KAGRA)* continue to reveal increasingly massive BH-BH mergers events. Still, the thus far heaviest GW mergers with the total mass of $M_{\bullet,\text{tot}} \sim 190 M_{\odot}\text{--}265 M_{\odot}$ (Abac et al. 2025b) are relatively close to the low mass end of the IMBH regime. At higher BH binary masses above $M_{\bullet,\text{tot}} \gtrsim 1000 M_{\odot}$ the current detectors are not sufficiently sensitive due to noise levels below ~ 10 Hz. However, IMBH mergers with a total mass of $500 M_{\odot} \lesssim M_{\bullet,\text{tot}} \lesssim 1000 M_{\odot}$ could be observable with the current *LIGO/Virgo/KAGRA* detectors with a sufficient signal-to-noise ratio of $S/N \sim 8$ to cosmological distances up to \sim a few Gpc, or to redshifts $z \lesssim 1$ (e.g. Mazzolo et al. 2014; Haster et al. 2016; Mehta et al. 2022; Fragione et al. 2022). Next generation ground-based GW detectors such as the Einstein Telescope and the Cosmic Explorer will be sensitive to GW mergers with total masses $M_{\bullet,\text{tot}} \lesssim 1000 M_{\odot}$ up to $z \lesssim 10$ (Reali et al. 2024; Abac et al. 2025a). In addition, the

future *Laser Interferometer Space Antenna (LISA)* will be able to observe merging high mass IMBHs with $M_{\bullet,\text{tot}} > 10^4 M_{\odot}$ including high redshift mergers above $z > 10$ (Amaro-Seoane et al. 2012).

A theoretical picture has emerged regarding IMBHs as left-over SMBH seeds that failed to grow at high redshifts $z \gtrsim 6$ (e.g. Mezcua 2017). Within this framework, finding and characterizing the local IMBH population and measuring their mass function could reveal invaluable information about the high redshift SMBH seeding mechanism. However, the picture relies on a number of crucial assumptions. First, the failed population of IMBHs has to be totally failed, i.e. not grown in mass since formation. While most of present day SMBH mass originates from gas accretion (Soltan 1982), growing especially low mass IMBHs into the SMBH mass regime via accretion in low mass galaxies seems indeed challenging (e.g. Partmann et al. 2025; Shin et al. 2025; Petersson et al. 2025). Meanwhile, IMBH growth by tidal disruption events in dense stellar environments such as nuclear star clusters (NSCs) seems difficult to avoid (Alexander & Bar-Or 2017a; Rizzato et al. 2023). Second, the "failed seeds" picture assumes that all (or at least the vast majority) of SMBH seeds formed at high redshifts. This is certainly true at least for the progenitors of the $6 \lesssim z \lesssim 12$ AGN population (e.g. Inayoshi et al. 2020), however, it has been proposed that individual SMBHs might form in extreme conditions also at lower redshifts (van Dokkum et al. 2025a,b). Finally, a population of IMBHs that formed at redshifts $z \lesssim 6$ might challenge, or at least complicate, the interpretation of the low redshift IMBH population as failed high redshift SMBH seeds. This is the key motivation of our study. We investigate whether IMBHs could form in young massive star clusters at redshifts below $z \lesssim 6\text{--}10$ and in the local Universe besides the $z > 10$ early proto GC like environments that we have explored in the previous studies of the FROST-CLUSTERS project (I: Rantala et al. 2024; II: Rantala et al. 2025).

In this work we explore if IMBHs can form in isolated and hierarchically assembling star clusters across a wide range of cluster densities up to $\rho_h \sim 6.5 \times 10^7 M_{\odot} \text{ pc}^{-3}$ and metallicities ($0.01 Z_{\odot} \lesssim Z \lesssim 1.0 Z_{\odot}$). The effect of metallicity on IMBH formation in individual cluster models has been examined in the literature (Mapelli 2016). While the cluster mass and density parameter space has been thoroughly explored at least for isolated clusters (e.g. Arca Sedda et al. 2024; González Prieto et al. 2024), however, IMBH formation through runaway collisions has not been systematically studied in models that vary both the initial star cluster densities and metallicities in their initial conditions.

We present an updated version of the **BIFROST** code including the support for AMD GPU hardware and new improved treatments for EMS and SMS models including their metallicity dependent radii and wind mass loss rates. Furthermore, we now include mass loss in stellar collisions from the colliding stars which can lead to substantial stellar mass loss in addition to the wind losses. Based on a novel sample of more than 1440 N -body simulations performed with the updated version of the **BIFROST** code, we provide practical fitting formulas for the IMBH masses $M_{\bullet} = M_{\bullet}(\Sigma_h, Z)$ as a function of their host cluster metallicity and surface density, and present a simple model to estimate the volumetric IMBH formation rate density at different redshifts based on our simulations. Our results can be used to seed black holes into star clusters in high resolution cosmological zoom-in simulations, and in semi-analytic models of galaxy formation.

The article is structured as follows. After the introduction we present the updated **BIFROST** code and our initial conditions in Section 2. We detail the metallicity and density dependent results of our isolated and hierarchical models focusing on the masses

of extremely massive stars and IMBHs in Section 3 and Section 4. Next, we examine the potential for wind and collisional ejecta enrichment in our models in Section 5, and present our calculation for the volumetric IMBH formation rate in Section 6. Finally, we summarize our results and conclude in Section 7.

2 NUMERICAL METHODS AND INITIAL CONDITIONS

2.1 Numerical methods: the updated BIFROST code

For the numerical simulations of this study we use the GPU accelerated direct summation N -body code BIFROST (Rantala et al. 2023) coupled with the rapid stellar population synthesis code SEVN (Iorio et al. 2023). BIFROST has been updated since the previous study of the FROST-CLUSTERS project (Rantala et al. 2025). The key improvements include models for mass loss in stellar collisions, supermassive stars and the ability to perform simulations on AMD accelerated processing unit (APU) hardware. In the following we briefly describe these main code updates.

2.1.1 Gravitational dynamics

Gravitational dynamics in the BIFROST code is modelled using the hierarchical variant (Rantala et al. 2021) of the fourth order forward symplectic integrator (Chin 1997; Chin & Chen 2005; Chin 2007; Dehnen & Hernandez 2017; Bernard et al. 2025). The time integration technique is momentum conserving and efficient for multi scale dynamical systems with a large dynamical range. For calculating the so-called gradient acceleration term responsible for cancelling the leading second order error terms we use the displacement approximation of Omelyan (2006) which simplifies the implementation of the algorithm especially on GPUs (Rantala et al. 2024). For strongly interacting small scale few-body systems including binaries, fly-bys, short-lived triple interactions, hierarchical triples as well as small clusters around massive BHs we use both secular and regularised integration techniques (Wang et al. 2020b; Rantala et al. 2020, 2023, 2024) including post-Newtonian (PN) equations of motion for BHs up to the order PN3.5.

2.1.2 Hardware acceleration and algorithmic updates

BIFROST performs the direct summation calculations for determining the particle accelerations and potential energies on GPUs, where the $O(N^2)$ double loops over the particles are mapped onto the massively parallel grid-like architecture (Rantala et al. 2021) using the CUDA programming standard for Nvidia GPUs. We have extended BIFROST with support for AMD GPUs based on the HIP programming model and the ROCm software stack. To avoid code duplication, the original CUDA based implementation is kept as the single source code, only a special C header file redefines the CUDA calls into HIP calls on-the-fly when compiling for a HIP target, a technique referred to as *hipify*. Hardware-specific parameters such as the configuration of the computational grid are defined at compile-time via preprocessor macros. Moreover, to reduce the number of copies of the particle ensemble, BIFROST makes use of node-local MPI shared memory windows which enable multiple MPI ranks to access the same single copy of the ensemble on a shared memory compute node, reducing the volume of the network communication and the number of messages exchanged.

2.1.3 Stellar evolution

BIFROST is coupled with the fast stellar population synthesis code SEVN (Iorio et al. 2023; Mapelli et al. 2020; Spera et al. 2015; Spera & Mapelli 2017). In SEVN we use the PARSEC-based (Bressan et al. 2012; Chen et al. 2015; Costa et al. 2021; Nguyen et al. 2022; Costa et al. 2025) stellar tracks SEVNtracks_parsec_ov04_AGB with the overshooting parameter $\lambda = 0.4$ ranging in stellar mass from $2.2 M_{\odot} \leq m_{\star} \leq 600 M_{\odot}$. For stripped pure He stars we select the SEVNtracks_parsec_pureHe36 tracks. In this study we consider nine different logarithmically spaced stellar metallicities from $Z = 0.0002 = 0.01 Z_{\odot}$ to $Z = 0.02 = 1.0 Z_{\odot}$.

Due to their large number (~ 1400), the simulations for this study were performed during the first half of 2025 using the most stable development branch of BIFROST at that time. This code branch did not include the SEVN binary stellar evolution coupling of BIFROST which we have used in our recent studies (Rantala & Naab 2025; Rantala et al. 2025). Thus, binary stars in the simulations of this study evolve as single stars. We still include initial (primordial) binary star populations in our models as they significantly enhance the stellar collision rates in star clusters (Fregeau et al. 2004; Gaburov et al. 2008; Rantala et al. 2025) due to their larger collision cross sections compared to single stars. Typically only a single star can considerably grow via collisions in isolated clusters (Baumgardt & Klessen 2011; Fujii & Portegies Zwart 2013; Rantala et al. 2024, 2025). For this rapid runaway stellar collisional channel (e.g. Greene et al. 2020 and references therein) the growing stars rapidly ($\lesssim 1$ –2 Myr) reach masses above $m_{\star} \gtrsim 600 M_{\odot}$, above the maximum stellar mass in the current SEVN stellar tracks. For these extremely massive stars and their collisions we use simplified evolution routines outlined in the following sections.

2.1.4 Collisions involving compact objects

Stars with masses m_{\star} and radii R_{\star} within the tidal disruption radius R_t (Kochanek 1992) defined as

$$R_t = 1.3 \left(\frac{M_{\bullet}}{m_{\star}} \right)^{1/3} R_{\star} \quad (1)$$

from any BH in the simulation will tidally disrupt. The BH accretes 50% of the stellar material while the other half is instantaneously removed from the simulation. Gravitational wave driven BH-BH mergers occur at the separation when the innermost stable circular orbits of the BHs overlap. For the BHs in our simulations this separation is always very small, less than $< 1 R_{\odot}$. At the moment of the BH-BH merger, the remnant experiences relativistic gravitational wave mass loss, and receives a gravitational wave recoil kick based on fitting functions to numerical relativity (Zlochower & Lousto 2015). For additional details of the compact object collision procedures see Rantala et al. (2024) and Rantala et al. (2025).

2.2 Stellar collisions and collision products

2.2.1 Mass loss in stellar collisions

Due to its simplicity, mass conservation in stellar collisions remains a common but not necessarily a well motivated assumption in N -body simulations (e.g. Lombardi et al. 2002; Glebbeek & Pols 2008; Glebbeek et al. 2009, 2013). Hydrodynamical stellar collision simulations of Glebbeek et al. (2013) suggest that the collisional

mass loss can be parametrized as

$$f_{\text{loss}} = \frac{Cq}{(q+1)^2} \quad (2)$$

in which $q = m_2/m_1 < 1$ and C is a constant that may depend on the structure of the stars. We use a mass loss prescription that is simplified and only depends on the mass ratio of the merging stars. In this work we set $C = 0.3$ (Glebbeek et al. 2013) yielding $f_{\text{loss,max}} = 7.5\%$ for equal mass stellar mergers. In the limit of $q \rightarrow 0$ there is no mass loss. The final mass of the collision product is thus $m_{\text{remnant}} = (m_1 + m_2)(1 - f_{\text{loss}}) = m_1 + m_2 - f_{\text{loss}}m_1 - f_{\text{loss}}m_2$. The lost mass $m_{\text{loss}} = (m_1 + m_2)f_{\text{loss}}$ is instantly removed from the N-body simulation. The mass loss recipe always satisfies $m_1 + m_2 - m_{\text{lost}} \geq m_1$. We note that recent work on extremely massive stellar collisions (e.g. Ramírez-Galeano et al. 2025) suggests that this assumption may not be always valid and the primary stars may suffer from catastrophic mass loss especially if they have marginally bound extended envelopes.

We note that in N -body simulations it is common to ignore the mass loss $f_{\text{loss}}m_1$ from the primary star. As we include this term, the total lost mass in N_{coll} collisions when building up a massive star may result in a cumulative mass loss larger than what would be possible for a single collision, i.e. $f_{\text{loss,cumu}} > f_{\text{loss,max}} = 7.5\%$. This is because each collision repeatedly removes mass from the primary star. We elaborate this process in detail in Appendix A and show that when doubling an initial mass of $m_{1,\text{init}}$ via collisions with $q \ll 1$ using the mass loss recipe of Eq. (2) and $C = 0.3$, we have $f_{\text{loss,cumu}} \sim 0.214 \sim 2.85 \times f_{\text{loss,max}}$. Such efficient cumulative collisional mass loss cannot occur in models that only include mass loss from the secondary star.

2.2.2 Massive stellar collision product radii

The radii of the very and extremely massive stars in our models exceeding $m_{\star} \gtrsim 600 M_{\odot}$ are modelled by extrapolating the zero age main sequence (ZAMS) radii of the massive stars from the PARSEC stellar tracks (Costa et al. 2025) including the metallicity dependence of the radii. We fit power-law relations of the form

$$\frac{R_{\star}}{1 R_{\odot}} = a(Z) \left(\frac{m_{\star}}{100 M_{\odot}} \right)^{\delta(Z)} \quad (3)$$

to ZAMS stellar radii in the mass range of $400 M_{\odot} \lesssim m \lesssim 600 M_{\odot}$, and obtain the coefficients $a(Z)$ and $\delta(Z)$ for nine different metallicities between $0.01 Z_{\odot}$ and $1.0 Z_{\odot}$. In BIFROST, given m and Z we linearly interpolate $a(Z)$ and $\delta(Z)$ from tabulated values to calculate R_{\star} . The coefficients $a(Z)$ and $\delta(Z)$ are listed in Table 1. We note that even though stars of higher metallicity initially have larger radii, their higher wind mass loss rates especially above $Z \gtrsim 0.5 Z_{\odot}$ result in initially low metallicity stars have larger radii towards the end of their lives.

We note that our massive stars have relatively small radii compared to the proposed protostar like models of extremely massive and supermassive stars. These stars can have extended radii depending on their gas accretion rates \dot{m}_{acc} , potentially reaching several orders of magnitude larger sizes compared to Eq. (3) for high \dot{m}_{acc} (e.g. Haemmerlé et al. 2018). Our relatively compact EMS and SMS sizes are consistent with low gas accretion rates of $\dot{m}_{\text{acc}} \lesssim 10^{-3} M_{\odot} \text{yr}^{-1}$ (Hosokawa et al. 2012), and by a factor of ~ 3 smaller compared to Gieles et al. (2018). At higher accretion rates, the increased sizes of the stars enhance their collision cross sections, but on the other hand may facilitate collisional mass loss from their diffuse envelopes (e.g.

Z / Z_{\odot}	$a(Z)$	$\delta(Z)$	R_{\star} for a $10^3 M_{\odot}$ star [R_{\odot}]
0.010	9.588	0.562	35.0
0.018	9.878	0.571	36.8
0.032	10.276	0.584	39.4
0.056	10.571	0.606	42.7
0.100	10.154	0.686	49.2
0.178	9.940	0.765	57.8
0.316	8.689	0.960	79.3
0.562	5.533	1.458	158.9
1.000	5.793	1.814	377.0

Table 1. The coefficients for the ZAMS mass size relation of Eq. (3) for stars exceeding $\gtrsim 600 M_{\odot}$ in mass. The radii of an example star of $10^3 M_{\odot}$ are provided at nine different metallicities.

Reinoso et al. 2023). For additional discussion of the massive stellar radii see Rantala et al. (2025).

2.2.3 Massive stellar collision product wind loss rates

Stellar wind mass loss by line driven winds (Castor et al. 1975; Abbott 1982; Garmany & Conti 1985) plays a fundamental role in the evolution of massive stars (Puls et al. 2008; Vink 2011). The wind mass loss rates dm_{wind}/dt depend on the mass, radius, temperature, luminosity and metallicity of the stars (e.g. Nieuwenhuijzen & de Jager 1990). The metallicity dependence of the wind loss rates of massive stars is commonly expressed as

$$\frac{dm_{\text{wind}}}{dt} \propto \left(\frac{Z}{Z_{\odot}} \right)^p, \quad (4)$$

in which the power law index is within the range of $0.5 \lesssim p \lesssim 0.94$ (Vink et al. 2001). For this study use the wind loss recipe of Vink (2018)

$$\log \left(\frac{dm_{\text{wind}}}{dt} \Big/ \frac{M_{\odot}}{\text{yr}} \right) = -9.13 + 2.1 \log(m_{\star}/M_{\odot}) + 0.74 \log(Z/Z_{\odot}), \quad (5)$$

which assumes relatively cool ($T_{\text{eff}} = 15000$ K) inflated very massive stars with large Eddington factors in the mass and metallicity ranges of $100 M_{\odot} \lesssim m_{\star} \lesssim 900 M_{\odot}$ and $0.01 \lesssim Z/Z_{\odot} \lesssim 1.0$. We note that Eq. (5) is used in our models beyond $m_{\star} \gtrsim 900 M_{\odot}$. The wind model or very similar recipes have been recently used both in analytic models (Gieles et al. 2018) and hydrodynamical simulations including collisional N -body dynamics (Fujii et al. 2024). The wind loss rates for extremely massive stars in this study are higher than in our previous studies (Rantala et al. 2024; Rantala & Naab 2025; Rantala et al. 2025) where we assumed a simple power-law scaling from the most massive PARSEC stellar tracks. In addition, together with the included mass loss in stellar collisions, we expect somewhat lower maximum stellar and IMBH masses at comparable star cluster densities compared to our earlier models.

We note that the Vink (2018) wind recipe we have adopted is not the only commonly used wind loss rate formulation used in N -body and cluster Monte Carlo simulations of runaway stellar collisional IMBH formation. In general, the adopted wind recipes in N -body simulations make up a substantial difference in the resultant wind mass loss rates especially for sub-solar metallicities (Banerjee et al. 2020). In the updated level C main sequence stellar evolution formulation of the NBODY6++GPU code, Kamlah et al. (2022) and Vergara et al. (2025a) assume the wind models of Vink

et al. (2001) for optically thin, line-driven outflows for hot and massive O and B type stars. Their massive and extremely luminous stars beyond the Humphreys-Davidson limit (Humphreys & Davidson 1994) ($L_\star/L_\odot > 6 \times 10^5$ and $10^{-5} \times R_\star/R_\odot (L/L_\odot)^{1/2} > 1$) undergo luminous blue variable (LBV) like mass loss with wind loss rates of $\dot{m}_{\text{LBV}} = f_{\text{LBV}} \times 10^{-4} \text{ M}_\odot \text{ yr}^{-1}$ (Belczynski et al. 2010) with $f_{\text{LBV}} \sim 1.5$. This LBV like wind loss rate effectively behaves as a maximum wind rate in the model. For our wind rate recipe $\dot{m} = 1.5 \times 10^{-4} \text{ M}_\odot \text{ yr}^{-1}$ is reached at $\sim 1700 \text{ M}_\odot$ for $Z = 0.01 \text{ Z}_\odot$ and $\sim 760 \text{ M}_\odot$ at $Z = 0.10 \text{ Z}_\odot$. As such, the wind rate estimations of the models in NBODY6++GPU and BIFROST considerably differ for extremely massive and supermassive stars. This has important implications for the final IMBH masses in the simulations and for the amount of enriched material produced by the extremely massive stars during their lifetimes.

2.2.4 Massive collision product ages and lifetimes

Stellar mergers¹ may provide a fresh supply of fuel into the centres of evolved stars (e.g. Leonard 1989; Lombardi et al. 2002). This stellar rejuvenation process is commonly treated in N -body simulations using parametrized age assignment formulas for the collision products depending on the types, ages and the masses of the merging stars (e.g. Hurley et al. 2002). Recently, Vergara et al. (2025a) demonstrated that widely used rejuvenation formulas can result in excessive rejuvenation when low mass stars collide with extremely massive and supermassive stars. We instead follow the rejuvenation prescription of Mapelli (2016) which cannot lead to such an excessive rejuvenation. We introduce a small modification to the prescription to take into account the mass loss in the collisions. For a primary star with a mass m_1 merging with a secondary star with a mass of m_2 ($m_1 \geq m_2$) and a collisional mass loss of m_{loss} , the age of the collision product is $A(m_1 + m_2 - m_{\text{loss}}) = f_{\text{rej}}(m_1, m_2, m_{\text{loss}})A(m_1)$. Here A is the age of the star in its current evolutionary stage (main sequence or evolved phase) and f_{rej} is the rejuvenation factor. For the age assignment procedure we group together the SEVN stellar evolution phases 1–3 (core hydrogen burning phases) and 4–6 (core helium burning phases). We define the rejuvenation factor as

$$f_{\text{rej}}(m_1, m_2, m_{\text{loss}}) = \frac{m_1}{m_1 + m_2 - m_{\text{loss}}} \frac{T(m_1 + m_2 - m_{\text{loss}})}{T(m_1)} \quad (6)$$

which adds the collisional mass loss m_{loss} into the recipe of Mapelli (2016). Here T is the total duration of the current stellar evolutionary stage. Note that in the limit of $q = m_2/m_1 \rightarrow 0$ the rejuvenation factor $f_{\text{rej}} \rightarrow 1$, so multiple collisions with low mass secondary stars do not excessively rejuvenate the collision product.

We determine the lifetimes of collisionally formed stars after which above $m_\star \gtrsim 600 \text{ M}_\odot$ they collapse into IMBHs using extrapolated PARSEC stellar tracks similarly to our extremely massive star radius determination procedure. Together with the rejuvenation procedure, the lifetimes T_{life} of our extremely massive stars are typically in the range of $2.5 \text{ Myr} \lesssim T_{\text{life}} \lesssim 5.0 \text{ Myr}$, consistent with N -body and Cluster Monte Carlo models in the literature (e.g. Vergara et al. 2025a).

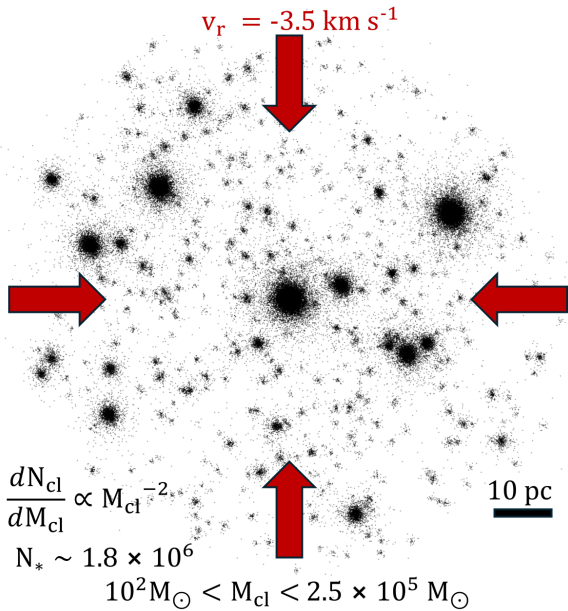


Figure 1. A schematic illustration of the initial conditions for the hierarchically assembling cluster setups.

2.3 Initial conditions

2.3.1 Isolated models

We construct idealised, isolated, spherically symmetric star cluster models following the Plummer (1911) density profile. For the isolated models we use three different cluster masses of $M_{\text{cl}} = 2.3 \times 10^4 \text{ M}_\odot$, $M_{\text{cl}} = 5.9 \times 10^4 \text{ M}_\odot$ and $M_{\text{cl}} = 1.5 \times 10^5 \text{ M}_\odot$ corresponding to $3.9 \times 10^4 \lesssim N \lesssim 2.5 \times 10^5$ individual stars. As in our previous FROST-CLUSTERS studies, we parametrise the initial mass-size relation of the star clusters as

$$\frac{r_h}{\text{pc}} = \frac{f_h R_4}{1.3} \left(\frac{M_\star}{10^4 M_\odot} \right)^\beta, \quad (7)$$

in which r_h is the 3D half mass radius. We set $\beta = 0.180 \pm 0.028$ and $R_4 = 2.365 \pm 0.106$ following Brown & Gnedin (2021). In Rantala et al. (2024) and Rantala et al. (2025), we used the normalisation parameter $f_h = 0.125$ to capture the small observed birth radii of embedded clusters (e.g. Marks & Kroupa 2012). For young local clusters (Brown & Gnedin 2021) $f_h = 1.0$, and for $z \sim 10$ JWST clusters (Adamo et al. 2024) $f_h \sim 0.15\text{--}0.20$, however, we note that these most likely differ from the birth radii of the clusters. For the isolated simulation sample we use five different normalisations of the cluster mass size relation in the range of $0.125 \leq f_h \leq 0.580$. For a fixed cluster mass M_{cl} this corresponds to a span of two orders of magnitude in the central Plummer model density ρ_c . With the three different cluster masses and five different densities, our isolated cluster models span a range of ~ 7 in cluster mass M_{cl} , a factor of ~ 70 in half mass surface density up to $\Sigma_h = 2.9 \times 10^5 \text{ M}_\odot \text{ pc}^{-2}$ and a factor of ~ 240 in central stellar density up to $\rho_c = 1.6 \times 10^6 \text{ M}_\odot \text{ pc}^{-3}$.

Besides the star cluster densities, we also extend our previous

¹ In this numerical work we use terms stellar collision and stellar merger interchangeably. To be precise, in the real Universe, a stellar collision can lead to either a common envelope episode, or a collision in which the two stars merge and mix into one.

Isolated models	N	M_{cl} [M_{\odot}]	$m_{\text{max},0}$ [M_{\odot}]	f_h	r_h [pc]	ρ_c [$10^5 M_{\odot} \text{ pc}^{-3}$]	Σ_h [$10^4 M_{\odot} \text{ pc}^{-2}$]	N_{metal}	N_{random}
IM1D1Z[1–9]	3.9×10^4	2.3×10^4	123.1	0.580	1.23	0.07	0.41	9	10
IM1D2Z[1–9]	3.9×10^4	2.3×10^4	123.1	0.395	0.84	0.21	0.89	9	10
IM1D3Z[1–9]	3.9×10^4	2.3×10^4	123.1	0.269	0.57	0.65	1.91	9	10
IM1D4Z[1–9]	3.9×10^4	2.3×10^4	123.1	0.184	0.39	2.07	4.11	9	10
IM1D5Z[1–9]	3.9×10^4	2.3×10^4	123.1	0.125	0.26	6.54	8.86	9	10
IM2D1Z[1–9]	1.0×10^5	5.9×10^4	150.0	0.580	1.45	0.10	0.75	9	10
IM2D2Z[1–9]	1.0×10^5	5.9×10^4	150.0	0.395	0.99	0.32	1.62	9	10
IM2D3Z[1–9]	1.0×10^5	5.9×10^4	150.0	0.269	0.67	1.01	3.49	9	10
IM2D4Z[1–9]	1.0×10^5	5.9×10^4	150.0	0.184	0.46	3.19	7.52	9	10
IM2D5Z[1–9]	1.0×10^5	5.9×10^4	150.0	0.125	0.31	10.09	16.20	9	10
IM3D1Z[1–9]	2.5×10^5	1.5×10^5	150.0	0.580	1.72	0.16	1.37	9	10
IM3D2Z[1–9]	2.5×10^5	1.5×10^5	150.0	0.395	1.17	0.49	2.94	9	10
IM3D3Z[1–9]	2.5×10^5	1.5×10^5	150.0	0.269	0.80	1.55	6.34	9	10
IM3D4Z[1–9]	2.5×10^5	1.5×10^5	150.0	0.184	0.54	4.90	13.66	9	10
IM3D5Z[1–9]	2.5×10^5	1.5×10^5	150.0	0.125	0.37	15.50	29.43	9	10

Table 2. The sample of 1350 N -body simulations of isolated models of this study (label I) including three different star cluster masses M_{cl} (labels M1–M3), five different normalizations of the cluster mass radius relation f_h i.e. different cluster densities (labels D1–D5), and nine different metallicities (labels Z1–Z9). Ten random realizations of each cluster model are performed. In the table, we also list the number of stars in the clusters N , their initial IMF cut-off mass $m_{\text{max},0}$, their 3D half-mass radii r_h as well as their 3D central densities ρ_c and 2D half-mass surface densities Σ_h .

studies in metallicity. In Rantala et al. (2024) and Rantala et al. (2025) we assumed a fixed stellar metallicity of $Z = 0.0002 = 0.01Z_{\odot}$. For the isolated simulation sample we explore nine different logarithmically spaced metallicities from $Z = 0.01Z_{\odot}$ to $1.0Z_{\odot}$. Finally, we run $N_{\text{random}} = 10$ random realisations of each isolated cluster model, and our full isolated cluster sample consists of in total 1350 N -body models. The main isolated cluster setups of this study with their key physical properties are listed in Table 2. Each isolated simulation (I) is labelled according to their mass (label M; 1–3), density (D; 1–5) and metallicity (Z; 1–9). We do not indicate the individual random realizations of the model in the labels.

2.3.2 Stellar populations

We assume coeval zero age main sequence stellar populations following the Kroupa (2001) initial mass function. The maximum initial stellar mass $m_{\text{max},0}$ depends on the cluster mass M_{cl} following Weidner & Kroupa (2006) and Yan et al. (2023) with the upper limit $m_{\text{max},0} = 150 M_{\odot}$ for massive clusters (Rantala et al. 2025). The binary star populations are initialised as described in Rantala et al. (2025) with the binary population properties observed by Moe & Di Stefano (2017), Winters et al. (2019) and Offner et al. (2023). The model results in an initial binary fraction of $f_b \sim 0.29$ with most of the massive stars initially in binaries. Unlike in Rantala et al. (2025), in this work we do not consider an initial triple star population.

Each isolated model is run until $t = 7.5$ Myr at which point all the massive BH progenitor stars have already ended their lives. We use BIFROST accuracy parameters of $\eta = 0.2$ for free-fall, fly-by and gradient time-step criteria (Rantala et al. 2023), few-body subsystem radii of $r_{\text{ngb}} = 5$ mpc as well as tolerance parameters $\eta_{\text{GBS}} = 10^{-8}$ and $\eta_{\text{endtime}} = 10^{-3}$ for algorithmically regularised few-body integration.

2.3.3 Hierarchically assembling cluster models

The initial conditions for our hierarchical star cluster assembly regions are set up as in Rantala et al. (2024) and Rantala & Naab (2025). A schematic illustration of a representative system is provided in Fig. 1. Individual star cluster masses up to $M_{\text{cl}} \sim 2.5 \times 10^5 M_{\odot}$ are sampled from the universal power-law cluster mass function with a slope of -2 (Elmegreen & Efremov 1996; Zhang & Fall 1999; Adamo et al. 2020; Lahén et al. 2020). The total mass of the hierarchical assembly region is $M_{\text{region}} = 10^6 M_{\odot}$ corresponding to $N \sim 1.8 \times 10^6$ individual stars in the clustered setups. We use the scatter of Brown & Gnedin (2021) in Eq. (7) for our initial cluster mass size relation in the hierarchical setups leading to somewhat different initial cluster densities in different random realizations of the models.

Motivated by the structure of hierarchical star cluster formation regions in the solar mass resolution hydrodynamical star burst simulations of Lahén et al. (2020), the centre-of-masses of the individual star clusters ($N_{\text{cl}} \leq 960$) are sampled within a uniform sphere with a radius of $r_{\text{region}} = 50$ pc. The hierarchical region is collapsing with a radial velocity component of $v_r = -3.5$ km/s and a random component of the same magnitude. The most massive sub-cluster is placed at the origin with a zero initial velocity. We further ensure that all sub-clusters are initially gravitationally bound to the hierarchically clustered region. For additional details of the structure of the hierarchical region setup see Rantala et al. (2024).

In this work we extend the study of hierarchically assembling star clusters to previously unexplored low density and extremely dense models beyond our fiducial star cluster mass radius relation normalization of $f_h = 0.125$. In total, we model nine different normalizations of the initial star cluster mass size relation. The maximum initial half mass densities of individual sub-clusters reach $\rho_h \sim 6.5 \times 10^7 M_{\odot} \text{ pc}^{-3}$ corresponding to maximum half mass surface densities of $\Sigma_h \sim 3.9 \times 10^6 M_{\odot} \text{ pc}^{-2}$. These densities considerably exceed the observed densities of YMCs in the local Universe (Krumholz et al. 2019), and even the densities of the $z \sim 10$ JWST

proto GCs with $R_e \sim 1$ pc and $M_{\text{cl}} \sim 10^6 M_\odot$ (Adamo et al. 2024). However, these are not necessarily the birth densities of the clusters, and it has been shown that dense star clusters can rapidly expand by a factor up to ~ 10 in their size (e.g. Arca Sedda et al. 2024; Lahén et al. 2025b) in their early evolution. For the Cosmic Gems clusters this argument yields maximum birth surface densities of $\Sigma_h \sim 1.6 \times 10^7 M_\odot \text{ pc}^{-2}$, a factor of ~ 4 higher than our densest model. Thus, our sub-cluster densities cover most of the plausible densities expected for forming star clusters in the Universe, except potentially the very extreme end. Each hierarchical model is simulated at $Z = 0.1 Z_\odot$ while we additionally run the densest models also at $Z = 0.01 Z_\odot$. Three random realizations of each model are generated resulting in total of 27 models at $Z = 0.1 Z_\odot$ and three extremely dense models with $Z = 0.01 Z_\odot$. We summarize the key properties of the central sub-clusters of the models with $M_{\text{cl}} = 2.5 \times 10^5 M_\odot$ in Table 3. Similarly to the isolated models, each hierarchical setup (H) is labelled according to their density (D; 1–9) and metallicity (Z; 1–2). Each hierarchical model is run until $t = 7.5$ Myr just as the isolated models with the same user given accuracy parameters.

3 RUNAWAY STELLAR COLLISIONS ACROSS STAR CLUSTER METALLICITIES AND DENSITIES: ISOLATED MODELS

3.1 Runaway collisions and star cluster metallicity

We present the mass growth histories of selected stars that considerably grew by stellar collisions in the isolated simulations models IM3D5Z1–9 with $M_{\text{cl}} = 1.5 \times 10^5 M_\odot$ and $\Sigma_h = 2.9 \times 10^5 M_\odot \text{ pc}^{-2}$ in Fig. 2. Each growth history represents a massive star that obtained the highest mass in its simulation as a star before collapsing into an IMBH. In a small number of simulations the most massive star is disrupted by a BH, or the IMBH is ejected after merging with a stellar BH due to a relativistic GW recoil kick. The low metallicity models IM3D5Z1 behave qualitatively similarly as our isolated setups in Rantala et al. (2024) and Rantala et al. (2025) despite the somewhat higher stellar wind mass loss rates for $\geq 600 M_\odot$ stars and the now included mass loss in collisions. At $Z = 0.01 Z_\odot$, the collision cascades commence between $t \sim 0.7$ –2.4 Myr. The growth of the stars by collisions is almost monotonic, and results in the collisional build-up of stars with masses in the range of $982 M_\odot \lesssim m_\star \lesssim 1583 M_\odot$. After the collapse of the stars into IMBHs until the end of the simulations at $t = 7.5$ Myr the further mass growth mainly proceeds via TDEs. By $t = 7.5$ Myr, the IMBHs have grown into the mass range of $1055 M_\odot \lesssim M_\bullet \lesssim 1870 M_\odot$, up to $\sim 20\%$ from their mass just after their formation. We note that the IMBH growth via TDEs can be artificially boosted in simplified, isolated models of young massive star clusters. In more realistic hierarchically assembling models, the clusters increase in size and decrease in mean density due to cluster mergers (Rantala et al. 2025) which can be understood in terms of virial arguments (e.g. Naab et al. 2009). Thus, the 20% IMBH mass growth by TDEs in $\lesssim 5$ Myr should be regarded as an optimistic upper limit. Between $t = 3$ –4 Myr and $t = 7.5$ Myr the mass growth via IMBH-BH mergers is minor, and IMBH-IMBH mergers are rare in isolated monolithic cluster setups (Rantala & Naab 2025).

At somewhat higher metallicities between $0.02 Z_\odot \lesssim Z \lesssim 0.10 Z_\odot$ the overall picture remains qualitatively similar to $Z = 0.01 Z_\odot$. After the collision cascades begin, the stellar mass growth is almost monotonic. Most cluster models form an IMBH which

further grow via TDEs. However, due to higher wind mass loss rates of extremely massive stars, the peak collisional stellar masses are somewhat lower. At $Z = 0.10 Z_\odot$ the maximum stellar masses are in the range of $558 M_\odot \lesssim m_\star \lesssim 1221 M_\odot$, 23–43% lower compared to the models with $Z = 0.01 Z_\odot$. Nevertheless, our results demonstrate that IMBH formation through stellar collisions remains viable even at moderate metallicities of $Z = 0.10 Z_\odot$ at fixed initial cluster mass and half-mass density. The final IMBH masses at $Z = 0.10 Z_\odot$ are in range between $694 M_\odot \lesssim M_\bullet \lesssim 1513 M_\odot$.

At higher metallicities above $Z > 0.1 Z_\odot$ the picture described above qualitatively changes. High wind mass loss rates at metallicities above $Z \gtrsim 0.2 Z_\odot$ efficiently prevent stellar mass growth, even though the runaway collision cascades still proceed. This results in non-monotonic growth histories for the stars. Instead, the mass growth histories of the stars $m_\star(t)$ show a maximum followed by a decline, a feature which becomes more prominent towards higher metallicities. Before forming IMBHs at the end of their lives, the high wind mass loss rates of the stars cannot be balanced with collisional mass gain, and the massive stars can substantially lose mass before the end of their lives (e.g. Mapelli 2016). Still, almost every dense cluster model forms an IMBH above a few hundred solar masses up to $Z \sim 0.5 Z_\odot$. At $Z = 0.56 Z_\odot$, the maximum collisional stellar masses reach $529 M_\odot \lesssim m_\star \lesssim 946 M_\odot$ while the formed IMBHs have masses of $376 M_\odot \lesssim M_\bullet \lesssim 705 M_\odot$ with up to $\sim 250 M_\odot$ of stellar material lost via strong winds.

Finally, at solar metallicity, IMBHs rarely form. With $Z = 1.0 Z_\odot$ only two random realizations out of 10 produce an IMBH in the models IM3D5Z9. The maximum collisional stellar masses achieved are $200 M_\odot \lesssim m_\star \lesssim 588 M_\odot$ as high stellar wind rates quench the mass growth. Thus, in most of the solar metallicity models the maximum final BH mass is in the stellar mass BH range. We note that IMBHs cannot form at $Z = 1.0 Z_\odot$ from stars with ZAMS masses of $m_\star \lesssim 600 M_\odot$ through isolated single stellar evolution.

3.2 Runaway collisions and star cluster density

3.2.1 The fraction of clusters that form an IMBH

Next, we explore the effect of the star cluster density on the fraction of the clusters that form an IMBH, and the masses of the IMBHs that form. The IMBH formation fraction is calculated as a fraction of random realizations that formed an IMBH out of $N_{\text{random}} = 10$ of each star cluster model. For this analysis we adopt an IMBH mass threshold of $M_\bullet > 2 \times m_{\text{max},0} = 300 M_\odot$ for runaway collisional IMBHs, and required that the IMBH is retained in the cluster until $t = 7.5$ Myr. The adopted runaway IMBH mass threshold excludes low mass IMBHs formed through a single merger of the components of a massive binary system. We will discuss these low mass binary merger IMBHs more in detail below. We focus on the isolated cluster models IM3D[1–5]Z[1–9] which all have $M_{\text{cl}} = 1.5 \times 10^5 M_\odot$. The half-mass surface densities of the models lie in the range of $1.4 \times 10^4 M_\odot \text{ pc}^{-2} \leq \Sigma_h \leq 2.9 \times 10^5 M_\odot \text{ pc}^{-2}$ while their metallicities are $0.01 Z_\odot \leq Z \leq 1.0 Z_\odot$. We present the IMBH fraction f_{IMBH} via a collision cascade for each model in Fig. 3. In the models IM3D[1–2]Z[1–9] with half-mass surface densities below $\Sigma_h \lesssim 2.9 \times 10^4 M_\odot \text{ pc}^{-2}$ no runaway IMBHs form at any metallicity as very few collisions occur in the low density models. Increasing the cluster densities, the models IM3D3Z[1–9] with $\Sigma_h = 6.3 \times 10^4 M_\odot \text{ pc}^{-2}$ are dense enough for forming runaway IMBHs with $f_{\text{IMBH}} \sim 0.1$ –0.4 (mean $f_{\text{IMBH}} \sim 0.22$) when $Z \leq 0.10 Z_\odot$, but not at higher metallicities. Towards in-

Hierarchical model central cluster	f_h	min r_h pc	max r_h pc	min–max ρ_c [$10^5 M_\odot pc^{-3}$]	min–max ρ_h [$10^5 M_\odot pc^{-3}$]	min–max Σ_h [$10^5 M_\odot pc^{-2}$]
HD1 (3 models)	0.580	1.67	2.16	0.03–0.06	0.03–0.06	0.05–0.08
HD2 (3 models)	0.395	1.14	1.47	0.08–0.18	0.09–0.20	0.11–0.18
HD3 (3 models)	0.269	0.78	1.00	0.27–0.58	0.30–0.64	0.23–0.39
HD4 (3 models)	0.184	0.53	0.68	0.85–1.84	0.94–2.02	0.51–0.84
HD5 (3 models)	0.125	0.36	0.46	2.71–5.84	2.97–6.41	1.09–1.82
HD6 (3 models)	0.067	0.24	0.32	8.58–18.51	9.42–20.33	2.35–3.93
HD7 (3 models)	0.034	0.17	0.22	27.19–58.67	29.87–64.45	5.08–8.48
HD8 (3 models)	0.014	0.11	0.15	86.19–186.00	94.68–204.32	10.95–18.29
HD9 (3 models)	0.004	0.08	0.10	273.23–589.61	300.14–647.69	23.63–39.47

Table 3. The densities of the central sub-clusters of our hierarchical cluster assembly models. Each central sub-cluster has a mass of $M_{\text{cl}} = 2.5 \times 10^5 M_\odot$ and consists of $N \sim 2.4 \times 10^5$ individual stars. The star cluster densities cover a range of four orders of magnitude in half-mass and central densities ρ_h and ρ_c as well as a factor of ~ 500 in half mass surface densities Σ_h . The total stellar mass within the hierarchically assembling regions is $M_\star \sim 10^6 M_\odot$ in $N = 1.8 \times 10^6$ individual stars.

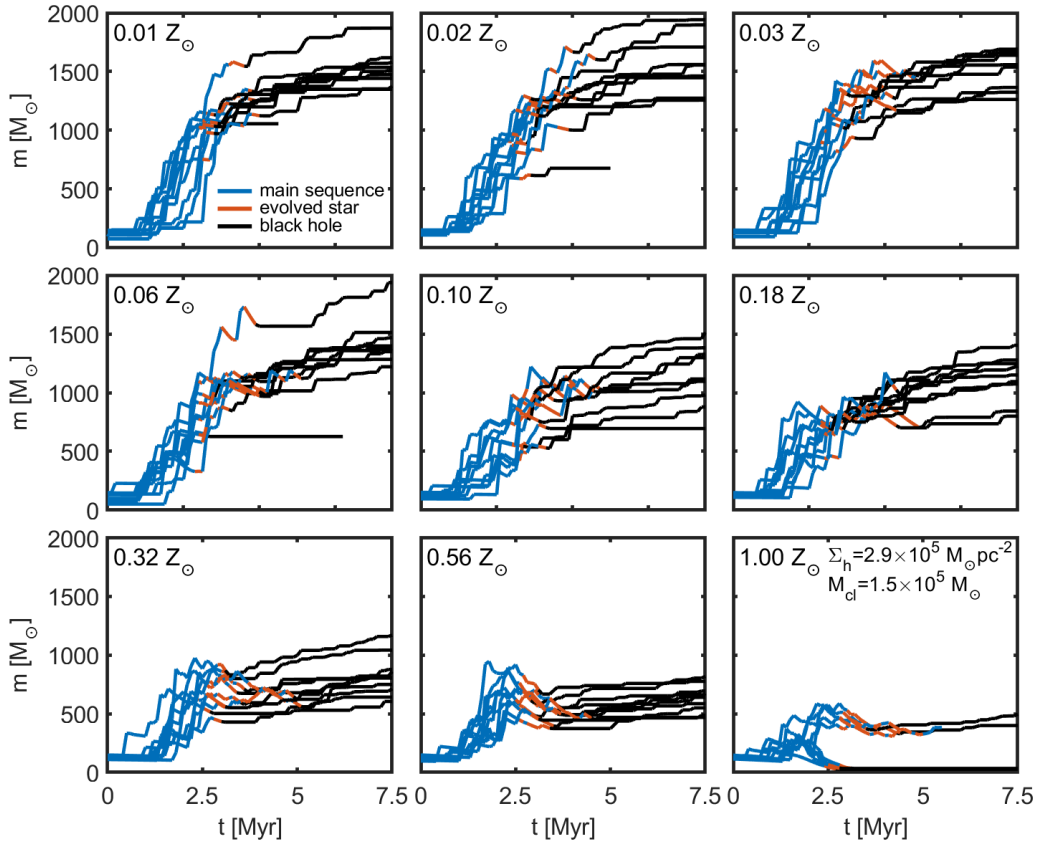


Figure 2. The mass growth histories of selected massive stars and IMBHs in the isolated dense star cluster models IM3D5Z1–9 with $M_{\text{cl}} = 1.5 \times 10^5$ and $\Sigma_h = 2.9 \times 10^5 M_\odot pc^{-2}$. Each line shows the growth history of a star that reached the highest mass in its host cluster during the simulation before collapsing into an IMBH. In a number of models the massive star is disrupted by a stellar BH or an IMBH, or the IMBH is ejected from its host cluster after merging with a stellar BH due to a GW recoil kick before the end of the simulations at $t = 7.5$ Myr. The metallicity increases in each panel starting from $Z = 0.01 Z_\odot$ on the top left. When increasing the metallicity from $Z = 0.01 Z_\odot$ to $Z = 0.10 Z_\odot$, the overall picture of the stellar mass growth remains similar while the maximum IMBH mass decreases from $M_\bullet \sim 1900 M_\odot$ to $1500 M_\odot$ in the models due to increased wind losses. Above $Z \gtrsim 0.2 Z_\odot$ the picture qualitatively changes as the stronger wind losses can quench the collision cascades, and the massive stars lose substantial amounts of mass before the ends of their lives. At solar metallicity, only few IMBHs can form.

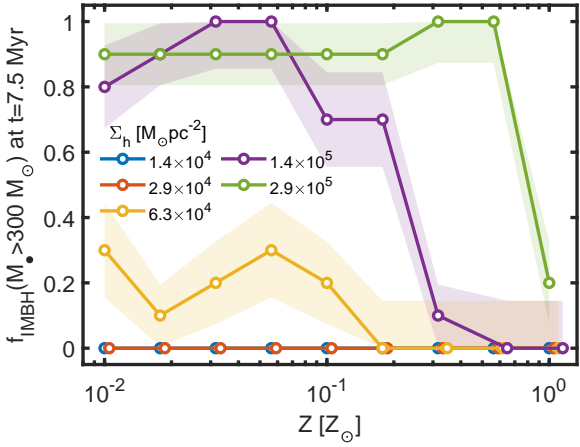


Figure 3. The fraction f_{IMBH} of star clusters forming an IMBH with $M_{>300} > 300 M_{\odot}$ via runaway collisions in the isolated setups and retaining it until $t = 7.5$ Myr with different densities and metallicities. In the models $M_{\text{cl}} = 1.5 \times 10^5 M_{\odot}$. The IMBH fraction sensitively depends on both cluster density and metallicity.

creasingly high cluster densities, the fraction of clusters with the runaway IMBH formation rapidly increases, and most high density cluster models almost always form a runaway IMBH. Above $\Sigma_h \gtrsim 1.4 \times 10^5 M_{\odot} \text{ pc}^{-2}$, $f_{\text{IMBH}} \gtrsim 0.8$ for models with a relatively low metallicity in the range of $Z \lesssim 0.06 Z_{\odot}$. At higher metallicities the IMBH formation fraction sharply decreases to $f_{\text{IMBH}} \sim 0.0\text{--}0.2$ after a critical metallicity that depends on the cluster (surface) density. For models with $\Sigma_h = 1.4 \times 10^5 M_{\odot} \text{ pc}^{-2}$ the critical metallicity threshold is between $0.10 Z_{\odot} \lesssim Z \lesssim 0.32 Z_{\odot}$ while for the most dense isolated models the threshold occurs above $Z \gtrsim 0.56 Z_{\odot}$.

3.2.2 The masses of the formed IMBHs

We present the masses of the most massive stellar BHs and IMBHs in all the random realizations of the models IM3D[1–5]Z[1–9] in Fig. 4. Furthermore, we display the IMBH masses from models with different metallicities and surface densities in Fig. 5 to allow for a straightforward comparison of the IMBH masses at different cluster surface densities. We note that while Fig. 2 focused on massive stars and IMBHs selected by their maximum mass in the stellar phase, for Fig. 4 and Fig. 5 we have selected the most massive (IM)BHs still present in their host clusters at $t = 7.5$ Myr. The figures also include the location of the metallicity dependent (P)PISN mass gap for BH masses assuming isolated single stellar evolution obtained from the PARSEC stellar tracks provided by the SEVN code. For metallicities above $Z \gtrsim 0.6 Z_{\odot}$, the high mass boundary of the (P)PISN mass gap is not captured by the available models limited to ZAMS masses below $Z \lesssim 600 M_{\odot}$. Thus, the exact extent of the (P)PISN mass gap and its upper edge at metallicities close to $Z = 1.0 Z_{\odot}$ is uncertain. Due to this and uncertainties in the wind loss rates (see Section 2.2.3) we emphasize that any formed IMBHs in this metallicity range $Z \gtrsim 0.6 Z_{\odot}$ should be regarded with caution. Finally, we note that Fig. 4 and Fig. 5 do not indicate how frequently the IMBHs with given masses form, but instead simply show the mass distribution of the most massive BHs and IMBHs in the models that formed IMBHs.

In the top two panels of Fig. 4, at low cluster surface densities below $\Sigma_h \lesssim 3 \times 10^4 M_{\odot} \text{ pc}^{-2}$ IMBHs rarely form. The only IMBHs at the low surface densities originate from individual collisions between components of massive initial binary systems which

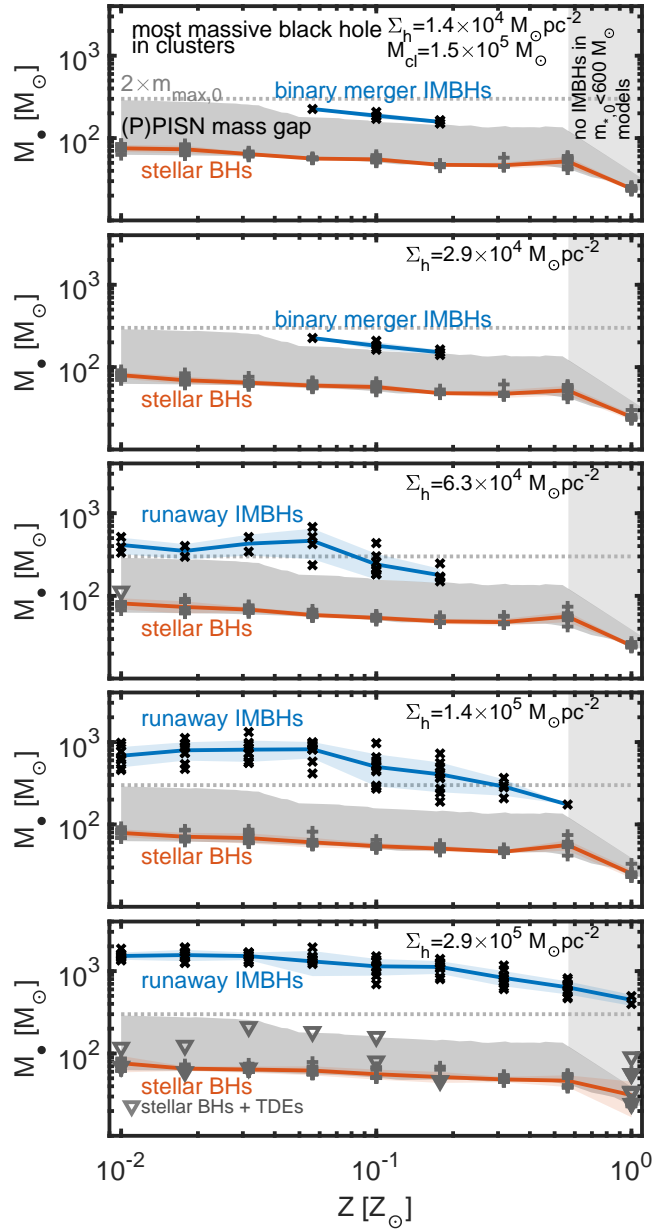


Figure 4. The masses $M_{>300}$ of the most massive stellar BHs and IMBHs in models with $M_{\text{cl}} = 1.5 \times 10^5 M_{\odot}$. From the top panel down the host cluster surface density increases from $\Sigma_h = 1.4 \times 10^4 M_{\odot} \text{ pc}^{-2}$ to $\Sigma_h = 2.9 \times 10^5 M_{\odot} \text{ pc}^{-2}$. In the two models with the lowest densities, no runaway collisions occur and IMBHs rarely form via a single massive binary merger. At $\Sigma_h \gtrsim 6.3 \times 10^4 M_{\odot} \text{ pc}^{-2}$ IMBHs form through stellar collision cascades with $M_{>300}$ increasing with increasing Σ_h especially at low metallicities $Z \lesssim 0.10 Z_{\odot}$. At higher metallicities the IMBH formation and their masses are suppressed due to the stellar wind mass losses. In the models with highest density, individual stellar BHs may grow into the (P)PISN mass gap via micro-TDEs.

predominantly occur at $t \gtrsim 2$ Myr in the simulations. By construction, $M_{>300} \lesssim 2 \times m_{\text{max},0} = 300 M_{\odot}$ for these relatively rare binary merger IMBHs, and the most massive stellar BHs lie near the lower edge of the (P)PISN mass gap. A number of stellar BHs in the setups grow via micro-TDEs (stellar BH TDEs; see e.g. Kremer et al. 2019; Rastello et al. 2025). Our assumed TDE accretion factor of

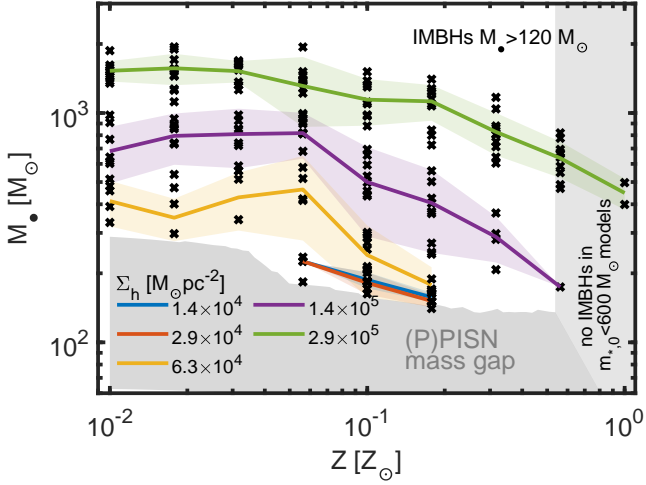


Figure 5. The maximum IMBH masses M_* in the simulations with $M_{\text{cl}} = 1.5 \times 10^5 M_{\odot}$ from Fig. 4. Above the critical surface density $\Sigma_h \gtrsim 6.3 \times 10^4 M_{\odot} \text{ pc}^{-2}$ IMBHs can form via runaway collision cascades, exceeding $M_* = 10^3 M_{\odot}$ in the models with $\Sigma_h = 2.9 \times 10^5 M_{\odot} \text{ pc}^{-2}$. At low metallicities $Z \lesssim 0.10 Z_{\odot}$ the stellar wind losses in the models are relatively weak and do not affect the final IMBH masses. However, above a critical metallicity threshold (e.g. $Z \sim 0.06 Z_{\odot}$ for $6.3 \times 10^4 M_{\odot} \text{ pc}^{-2} \lesssim \Sigma_h \lesssim 1.4 \times 10^5 M_{\odot} \text{ pc}^{-2}$) the masses of the formed IMBHs decline due to the wind mass losses of their progenitor stars before the ends of their lives.

0.5 is relatively high for micro-TDEs and thus the masses of BHs grown via this channel should be considered as upper limits.

This low density picture changes above surface densities $\Sigma_h \gtrsim 6.3 \times 10^4 M_{\odot} \text{ pc}^{-2}$. First, at low metallicities below $Z \lesssim 0.2 Z_{\odot}$, relatively short ($N_{\text{coll}} > 2$) collision sequences occur leading to the formation of IMBHs in the mass range of $300 M_{\odot} \lesssim M_* \lesssim 600 M_{\odot}$ from massive progenitor stars above the (P)PISN mass gap. These results are consistent with Mapelli (2016) who found remnant masses up to $\sim 250 M_{\odot}$ at somewhat lower initial cluster densities. Above the critical metallicity of $Z \gtrsim 0.2 Z_{\odot}$ no IMBHs form. The collision rates in the runaway cascades increase with increasing cluster surface density, and the maximum metallicity in which any IMBHs can form also increases accordingly. At $\Sigma_h = 1.4 \times 10^4 M_{\odot} \text{ pc}^{-2}$, the most massive IMBHs reach masses exceeding $M_* \sim 10^3 M_{\odot}$ at $Z < 0.10 Z_{\odot}$, well above the (P)PISN mass gap at metallicities below $Z \lesssim 0.2 Z_{\odot}$. Finally, the bottom panel of Fig. 4 shows our models with the highest initial densities. As already shown in Fig. 2, the maximum IMBH masses of the models M3D5Z[1–6] with $Z \lesssim 0.2 Z_{\odot}$ are in the range of $1.5 \times 10^3 M_{\odot} \lesssim M_* \lesssim 1.9 \times 10^3 M_{\odot}$. At higher metallicities ($Z \gtrsim 0.2 Z_{\odot}$) the IMBH masses considerably decrease due to the strong stellar winds.

Fig. 5 reveals two clear trends for the IMBH masses as a function of their host cluster metallicity and density. First, at low metallicities below $Z \lesssim 0.06 Z_{\odot}$, the IMBH masses steadily increase as a function of the host cluster mass above $\Sigma_h \gtrsim 6.3 \times 10^4 M_{\odot} \text{ pc}^{-2}$. This is due to the combination of increasingly lengthy collision cascades and relatively weak stellar winds at low metallicities. Second, the IMBH masses strongly decline towards higher metallicities in all dense cluster models. Most importantly, the metallicity threshold after which the IMBH masses strongly decline depends on the cluster surface density. For models with $\Sigma_h = 6.3 \times 10^4 M_{\odot} \text{ pc}^{-2} - 1.4 \times 10^5 M_{\odot} \text{ pc}^{-2}$ the IMBH masses begin to steadily decrease after $Z \gtrsim 0.06 Z_{\odot}$, and for the highest density models with

$\Sigma_h = 2.9 \times 10^5 M_{\odot} \text{ pc}^{-2}$ at $Z \gtrsim 0.2 Z_{\odot}$. Finally, we note that the final IMBH masses are affected by the uncertainties in the extremely massive star wind mass loss rates. We briefly explore this in Appendix B.

3.3 The combined effect of cluster mass, metallicity and surface density on the IMBH masses

3.3.1 Above a critical cluster mass threshold, Σ_h and Z determine the maximum M_* .

In the previous sections we have focused on our isolated star cluster models with $M_{\text{cl}} = 1.5 \times 10^5 M_{\odot}$. We now extend these results to our lower cluster masses of $M_{\text{cl}} = 2.3 \times 10^4 M_{\odot}$ and $M_{\text{cl}} = 5.9 \times 10^4 M_{\odot}$. We note that all the examined cluster setups are massive enough to potentially form IMBHs: our previous simulations (Rantala et al. 2024, 2025) have demonstrated that dense but low mass ($M_{\text{cl}} \lesssim 10^4 M_{\odot}$) clusters rarely produce an IMBH. As shown in Table 2, the surface density ranges for isolated cluster models of different masses largely overlap. We present the masses of the most massive stellar BHs and IMBHs formed in all our 1350 isolated star cluster models in Fig. 6. For stellar BHs the results of the lower mass cluster models agree with the $M_{\text{cl}} = 1.5 \times 10^5 M_{\odot}$ results presented in the previous section. The lowest cluster mass models with $M_{\text{cl}} = 2.3 \times 10^4 M_{\odot}$ produce somewhat less massive stellar BHs because of their lower IMF cut-off mass $m_{\text{max},0}$ in the initial conditions as indicated in Table 2. At metallicities below $Z \lesssim 0.2 Z_{\odot}$, IMBHs form in the models with different masses with a clear correlation between the cluster surface densities and the resulting IMBH masses. For a fixed metallicity Z and surface density Σ_h the cluster mass M_{cl} has a little effect on the final IMBH masses M_* . Thus, it seems that only two parameters, Z and Σ_h , are required to determine the maximum M_* in isolated setups. This is not unexpected as for our models Σ_h and M_{cl} are not completely independent but related through the shallow fixed power-law slope initial mass-radius relation of Eq. (7) of the clusters. Towards higher metallicities, the critical surface density threshold for IMBH formation increases, and above $Z \gtrsim 0.3 Z_{\odot}$ fewer IMBHs form, especially at solar metallicity.

3.3.2 A LOESS smoothed model for M_* as a function of host cluster properties

Motivated by the evident correlations between the maximum IMBH masses and Σ_h at each cluster metallicity in Fig. 6, we proceed to build a model for the formed IMBH masses as a function of their host cluster surface density and metallicity, i.e. $M_* = M_*(\Sigma_h, Z)$. However, even with our isolated simulation sample of 1350 models, our models do not uniformly sample the two-dimensional (Σ_h, Z) parameter space. Therefore, we produce a two-dimensional smoothed map $M_*(\Sigma_h, Z)$ employing the publicly available Locally Weighted Regression (LOESS) software package² of Cappellari et al. (2013). LOESS is an adaptive smoothing technique designed to recover mean trends from scattered data points with noise in one or two dimensions (Cleveland & Devlin 1988). The resulting smoothed map $M_*(\Sigma_h, Z)$ is presented in Fig. 7. We emphasize that the figure only displays the maximum masses of the IMBHs that can form in the clusters, not how frequently they form. As shown in Fig. 3, IMBHs rarely form at metallicities close to solar even in dense clusters.

² <https://users.physics.ox.ac.uk/~cappellari/software/>

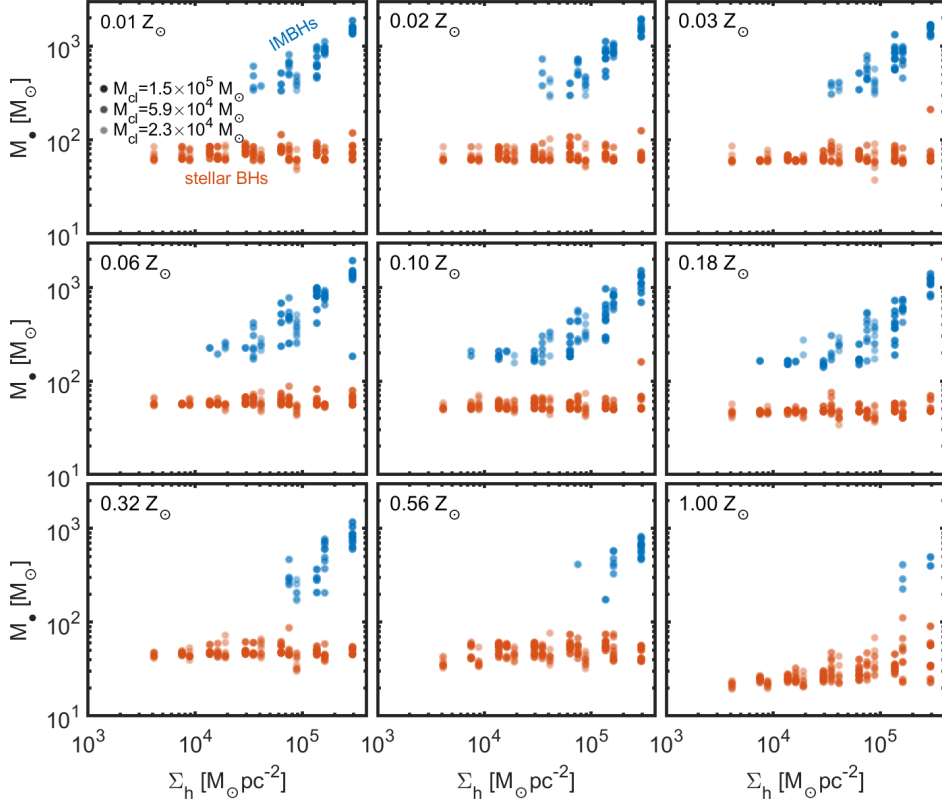


Figure 6. The most massive stellar BHs and IMBHs in the isolated simulations at $t = 7.5$ Myr at different metallicities as a function of the cluster half mass surface density Σ_h . The cluster masses $2.3 \times 10^4 M_\odot \lesssim M_\bullet \lesssim 1.5 \times 10^5 M_\odot$ are indicated by the increasingly dark shaded symbols. The maximum stellar BH masses typically lie close to the lower edge of the (P)PISN mass gap at each different metallicity. At high surface densities individual stellar BHs may grow via micro-TDEs as discussed in the main text. Especially at metallicities $Z \lesssim 0.32 Z_\odot$ there is a clear correlation between the IMBH masses and the host cluster half mass surface densities. For a fixed cluster half mass surface density Σ_h the cluster mass M_{cl} has little effect on M_\bullet .

Two separate regions are apparent in the smoothed map $M_\bullet(\Sigma_h, Z)$ of Fig. 7: stellar BHs at low densities and high metallicities, and IMBHs at high densities and low metallicities. At low surface densities the most massive BHs are always in the stellar mass regime with $M_\bullet \lesssim 100 M_\odot$. Above a critical metallicity, IMBHs can only form in sufficiently dense systems separated from the stellar BH regime by the surface density dependent critical metallicity. A metallicity threshold contour line $Z_{100 M_\odot} = Z(M_\bullet = 100 M_\odot)$ is presented in Fig. 7 and approximately follows the equation

$$\log_{10} \left(\frac{Z_{100 M_\odot}}{Z_\odot} \right) \approx \begin{cases} \leq \log_{10} \left(\frac{Z_{\text{crit}}}{Z_\odot} \right) & \text{if } \Sigma_h = \Sigma_{\text{crit}} \\ k_{\text{crit}} \log_{10} \left(\frac{\Sigma_h}{\Sigma_{\text{crit}}} \right) + \log_{10} \left(\frac{Z_{\text{crit}}}{Z_\odot} \right) & \text{if } \Sigma_{\text{crit}} < \Sigma_h \end{cases} \quad (8)$$

in which $\Sigma_{\text{crit}} \approx 2.79 \times 10^4 M_\odot \text{ pc}^{-2}$, $Z_{\text{crit}} \approx 0.14 Z_\odot$ and $k_{\text{crit}} \approx 1.20$. The contour line for $M_\bullet = 1000 M_\odot$ displayed in Fig. 7 shows a very similar angular shape as the contour for $Z_{100 M_\odot}$. Even at low metallicities, star cluster surface densities above $\Sigma_h \gtrsim 2 \times 10^5 M_\odot \text{ pc}^{-2}$ are required to produce a $M_\bullet = 10^3 M_\odot$ IMBH.

3.4 A parametrised fit model for estimating star cluster IMBH masses

The very regular shapes of the critical metallicity contour lines for IMBH masses $M_\bullet = 100 M_\odot$ and $M_\bullet = 1000 M_\odot$ in Fig. 7 and Eq. (8) suggest that it should be possible to construct a parametrized model for the IMBH masses $M_\bullet(\Sigma_h, Z)$ that follows a relatively simple functional form. We show that this is indeed the case, but special care is required to ensure that the parametrized model remains well-behaved outside the parameter space of the performed simulations especially towards increasingly high cluster surface densities.

In order to find a suitable parametrized fitting formula for the LOESS smoothed map $M_\bullet(\Sigma_h, Z)$ in Fig. 7 we first have to omit the stellar BH masses from the fitting process and focus on the IMBH regime on the right of the $M_\bullet = 100 M_\odot$ contour. This is because for each metallicity Z , $M_\bullet(\Sigma_h)$ has a sudden step function like jump from the lower edge of the (P)PISN mass gap into the IMBH mass regime at the critical surface density Σ_{crit} at which runaway stellar collisions first begin to occur. Such a step function feature is difficult to fit using continuous and well-behaved functions, and we instead choose to focus on the IMBH mass regime for the parametrization of $M_\bullet(\Sigma_h, Z)$. The stellar BH masses at low cluster surface densities and high metallicities can be obtained with any suitable fast stellar

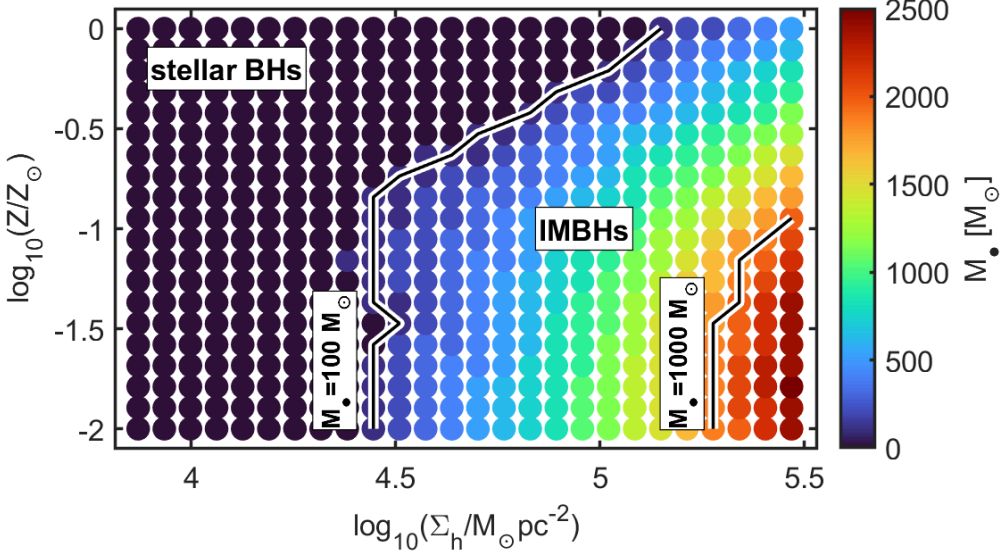


Figure 7. The LOESS smoothed map presenting the maximum IMBH mass as a function of their host star cluster half mass surface density Σ_h and metallicity Z . The contours for $M_\bullet = 100 M_\odot$ and $M_\bullet = 1000 M_\odot$ show very regular angular shapes. Stellar BHs occupy the parameter space towards lower surface densities and higher metallicities from the critical contour of $M_\bullet = 100 M_\odot$ while increasingly massive IMBHs are found towards the bottom right corner with the highest cluster densities and lowest metallicities.

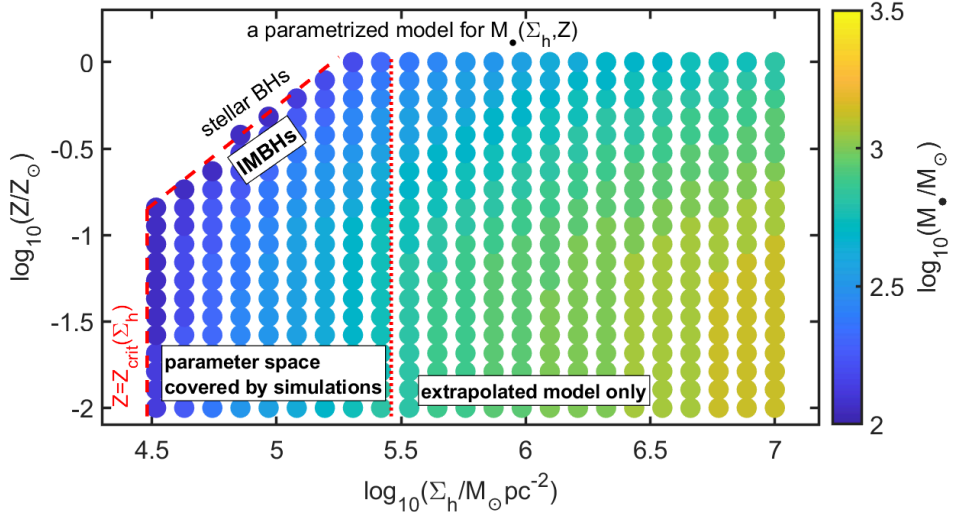


Figure 8. The parametrized model for IMBH masses as a function of their host cluster half mass surface densities Σ_h and metallicities Z . For the illustration we use Eq. (9) below $\log_{10}(\Sigma_h / M_\odot \text{ pc}^{-2}) < 5.45$, and Eq. (10) above it.

population synthesis model (Hurley et al. 2000, 2002; Iorio et al. 2023) instead.

Our aim is to find a relatively simple parametrized functional form for $M_\bullet(\Sigma_h, Z)$ which remains well behaved when extrapolated to higher star cluster surface densities beyond $\gtrsim 2.9 \times 10^5 M_\odot \text{ pc}^{-2}$. We provide two different parametrized functional forms: a simple formula that behaves well at high extrapolated cluster surface densities, and a somewhat more complex formula for the (Σ_h, Z) parameter space of our simulations. For both formulas, we first fit $M_\bullet(\Sigma_h)$ for each fixed metallicity Z , and then find a second parametric model to describe the fit parameters as a function of metallicity. After experimenting with various functional forms to be used within the

(Σ_h, Z) parameter space of our simulations we arrive at

$$\frac{M_\bullet}{M_\odot} = \theta_H\left(\Sigma_h - \Sigma_{\text{crit}}(Z)\right) \left\{ A(Z) \log_{10}\left(\frac{\Sigma_h}{M_\odot \text{ pc}^{-2}}\right) \right. \\ \left. + B(Z) \left[\log_{10}\left(\frac{\Sigma_h}{M_\odot \text{ pc}^{-2}}\right) \right]^2 + C(Z) \right\} \quad (9)$$

in which $\theta_H(x)$ is the Heaviside step function, and the coefficients $\Sigma_{\text{crit}}(Z)$, $A(Z)$, $B(Z)$ and $C(Z)$ are metallicity dependent. For example, the coefficient $A(Z)$ can be represented using a piecewise defined function of the form $A(Z) = A_1 \log_{10}(Z/Z_\odot) + A_2$ in three metallicity intervals: $Z/Z_\odot < 0.126$, $0.126 \leq Z/Z_\odot < 0.398$ and

Coeff.	$Z/Z_\odot < 0.126$	$0.126 \leq Z/Z_\odot < 0.398$	$Z/Z_\odot > 0.398$
A_1	-1790.07	+9707.84	+1147.68
A_2	-7392.65	+2627.71	-721.18
B_1	+162.46	-1015.72	-166.92
B_2	+829.42	-211.38	+126.15
C_1	+4734.11	-23585.20	-2002.25
C_2	+16556.82	-7814.04	+471.59
Σ_1	+0.0386	+0.91	+0.91
Σ_2	+4.53	+5.22	+5.22

Table 4. The parametrized coefficients for constructing $A(Z)$, $B(Z)$, $C(Z)$ and $\Sigma(Z)$ in Eq. (9). For example, $A(Z) = A_1 \log_{10}(Z/Z_\odot) + A_2$.

Coeff.	$Z/Z_\odot < 0.079$	$0.079 \leq Z/Z_\odot < 0.316$	$Z/Z_\odot > 0.316$
D_1	-37.37	-922.15	-611.27
D_2	+1452.33	+466.71	+628.40
E_1	+81.66	+4242.58	+2620.25
E_2	-6892.57	-2280.02	-3137.93

Table 5. The parametrized coefficients for constructing $D(Z)$ and $E(Z)$ in Eq. (10).

$Z > 0.398$. The coefficients $B(Z)$ and $C(Z)$ follow similar piecewise relations. We provide the metallicity dependent coefficients A_1 , A_2 , B_1 , B_2 , C_1 , C_2 , Σ_1 and Σ_2 for the parametrized formulas in Table 4.

An alternative fit parametrization for high star cluster surface densities above $\log_{10}(\Sigma_{\text{crit,max}} / M_\odot \text{ pc}^{-2}) = 5.2$ is

$$\frac{M_\bullet}{M_\odot} = \theta_H \left(\Sigma_h - \Sigma_{\text{crit,max}} \right) \left\{ D(Z) \log_{10} \left(\frac{\Sigma_h}{M_\odot \text{ pc}^{-2}} \right) + E(Z) \right\} \quad (10)$$

in which the parameters $D(Z)$ and $E(Z)$ are again metallicity dependent. The coefficients D_1 , D_2 , E_1 and E_2 to construct e.g. $D(Z)$ via $D(Z) = D_1 \log_{10}(Z/Z_\odot) + D_2$ can be found in Table 5. This second parametrized model for M_\bullet remains well behaved also at high star cluster surface densities. We present the model in Fig. 8 extrapolating the results for M_\bullet up to high surface densities of $\Sigma_h = 3.2 \times 10^6 M_\odot \text{ pc}^{-2}$, approximately an order of magnitude higher than our most dense models.

For using the models of Eq. (9) and Eq. (10) for seeding IMBHs into star clusters in semi-analytic galaxy evolution frameworks or high mass resolution ($\lesssim 10 M_\odot$) hydrodynamical simulations, the 3D half mass density ρ_h may be required instead of the projected Σ_h . For the Plummer model the 2D and 3D half mass densities are related as

$$\frac{\Sigma_h(\rho_h)}{6.99 \times 10^4 M_\odot \text{ pc}^{-2}} = \left(\frac{M_{\text{cl}}}{10^5 M_\odot} \right)^{1/3} \left(\frac{\rho_h}{10^5 M_\odot \text{ pc}^{-3}} \right)^{2/3}. \quad (11)$$

For simulation models that can track star cluster masses but not their densities (e.g. gravitationally softened hydrodynamical models with mass resolutions above $m_\star > 100 M_\odot$), one should assume the normalization of the cluster birth mass size relation f_h from Eq. (7) to use the IMBH mass fitting formulas. We will use the parametrized IMBH mass models to provide an estimate of the IMBH formation rate density in Section 6.

4 HIERARCHICAL STAR CLUSTER ASSEMBLY AND IMBH FORMATION AT $Z = 0.01 Z_\odot$ AND $Z = 0.1 Z_\odot$

4.1 IMBH formation in extremely dense hierarchically assembling star clusters

After our exploration of idealised, isolated cluster models initially in equilibrium we proceed to simulate hierarchically assembling massive star clusters. While the isolated setups can be regarded as useful numerical experiments to study IMBH formation in dense systems, the hierarchical models represent more realistic physically motivated initial setups for star cluster formation. We note that even the hierarchical N -body models have a degree of idealization as they do not take into account the extended star formation history a star cluster would have in reality. We perform in total 30 hierarchical star cluster assembly simulations as listed in Table 3 to explore the collisional massive star and IMBH formation as well as chemical enrichment by such massive stars in different metallicities and especially cluster densities. In total 27 models are simulated at $Z = 0.10 Z_\odot$ (models HD[1-9]Z2) while the three densest models are also run with $Z = 0.01 Z_\odot$ (models HD9Z1). The central clusters of the densest models initially have half mass densities up to $\rho_h \sim 6.5 \times 10^7 M_\odot \text{ pc}^{-3}$ corresponding to half mass surface densities of $\Sigma_h \sim 3.9 \times 10^6 M_\odot \text{ pc}^{-2}$. Our previous studies of the hierarchical cluster assembly (Rantala et al. 2024; Rantala & Naab 2025; Rantala et al. 2025) have focused on clusters at $Z = 0.01 Z_\odot$ with somewhat lower central densities up to $\rho_c \sim 1-2 \times 10^6 M_\odot \text{ pc}^{-3}$. The central sub-clusters of our intermediate density models HD5Z[1-2] closely resemble the simulated massive young star cluster of Lahén et al. (2025a) formed in a dwarf galaxy merger starburst.

We present the mass growth histories of the most massive star in our densest cluster models HD9Z1 and HD9Z2 in the left panel of Fig. 9. In all extremely dense models the cascade of runaway stellar collisions commences after $t \sim 0.1$ Myr and the stars rapidly reach twice the maximum initial IMF cut-off mass of $2 \times m_{\text{max},0} = 300 M_\odot$ by $t = 0.12-0.17$ Myr. The stars increase their mass via collisions and reach $m_\star = 1000 M_\odot$ by $t = 0.15-0.29$ Myr and $m_\star = 4000 M_\odot$ before $t = 1.04$ Myr. However, no massive star reaches $m_\star = 10000 M_\odot$ in our simulation sample despite the extremely high initial star cluster densities. This is due to the stellar wind mass losses being higher or comparable to the collisional mass gains of the extremely massive stars after $t > 1$ Myr. At $Z = 0.10 Z_\odot$, the maximum stellar masses are in the range of $4496 M_\odot \lesssim m_{\text{max}} \lesssim 5413 M_\odot$, and for $Z = 0.01 Z_\odot$, $6131 M_\odot \lesssim m_{\text{max}} \lesssim 7263 M_\odot$. The times for the peak collisional stellar masses occur between $t = 0.70-1.04$ Myr for $Z = 0.10 Z_\odot$ and somewhat later between $t = 1.18-1.99$ Myr in the models with $Z = 0.01 Z_\odot$. After the moment of peak collisional stellar mass, the masses of the stars either remain relatively constant until the end of the stellar lifetimes at $t = 3-4$ Myr ($Z = 0.01 Z_\odot$) or steadily decline ($Z = 0.10 Z_\odot$). The masses of the IMBHs at their formation are $2118 M_\odot \lesssim M_\bullet \lesssim 2302 M_\odot$ ($Z = 0.10 Z_\odot$) and $4747 M_\odot \lesssim M_\bullet \lesssim 5988 M_\odot$ ($Z = 0.01 Z_\odot$), respectively.

We examine the mass budget of the collisionally grown massive stars in our densest models in panels two to four of Fig. 9. At lower metallicities $Z = 0.01 Z_\odot$, the masses of the extremely massive stars remain relatively constant after reaching their peak masses. This balance between the mass gained in the stellar collisions (the second panel) and the losses via collisions (the third panel) and winds (the final fourth panel) is maintained for 2–3 Myr until the stars end their lives. The most massive star at $Z = 0.01 Z_\odot$ gains $m_{\text{gain}} = 17367 M_\odot$ of material during its lifetime, and loses $m_{\text{coll}} = 4883 M_\odot$ and $m_{\text{wind}} = 6590 M_\odot$ via collisions and winds,

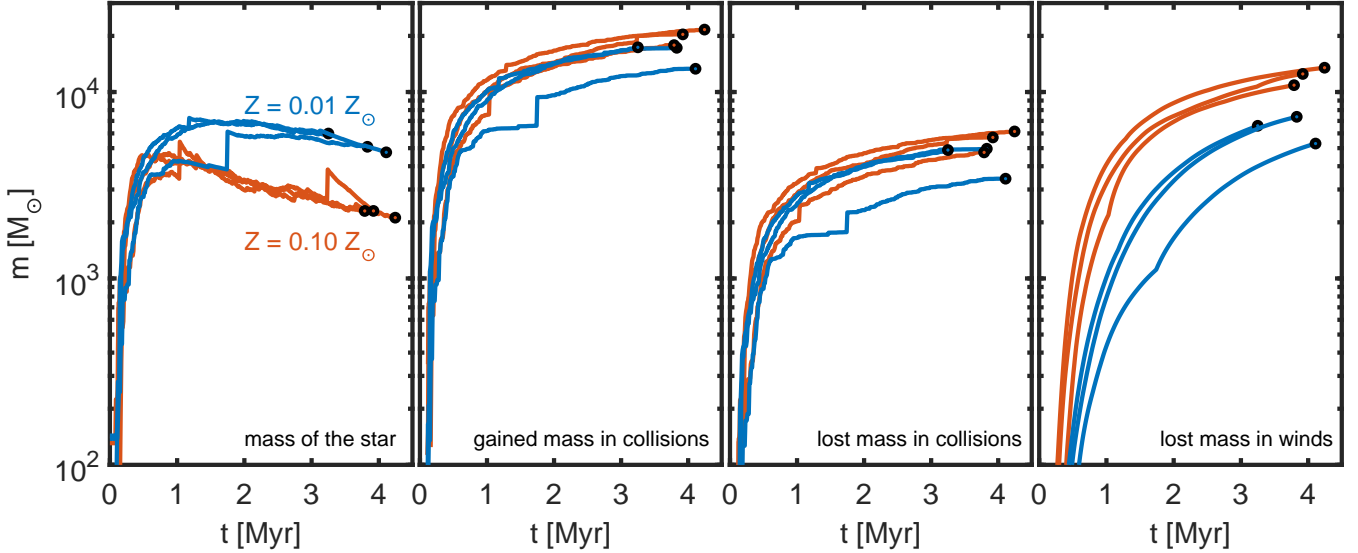


Figure 9. The mass growth and loss histories of six most massive stars formed in our densest hierarchical models HD9Z1 ($Z = 0.01 Z_{\odot}$) and HD9Z2 ($Z = 0.10 Z_{\odot}$). First panel: the masses of the stars as function of time. Second panel: the cumulative gained mass by the stars i.e. the sum of secondary impacting stars m_2 . Third and fourth panels: the cumulative mass lost in collisions and stellar winds. While the gained masses are comparable in models with different metallicities, the higher wind loss rates at $Z = 0.10 Z_{\odot}$ lead to earlier quenching of the runaway mass growth. Note that the runaway collisions still proceed after $t \gtrsim 1$ Myr even though the mass growth of the stars plateaus or turns into decline. No star in our densest models reaches $m_{\star} = 10000 M_{\odot}$ while the total gained mass in stellar collisions can exceed $m_{\text{gain}} \gtrsim 21600 M_{\odot}$.

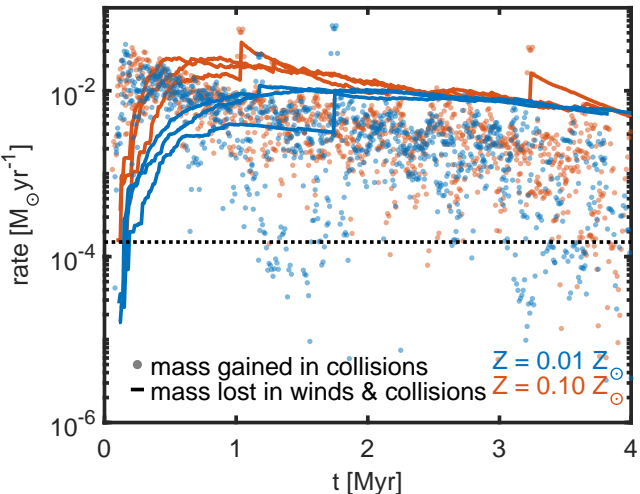


Figure 10. The rates for gained (dots) and total lost mass (solid lines) from the most massive stars in our densest hierarchical models with $Z = 0.10 Z_{\odot}$ (HD9Z2) and $Z = 0.01 Z_{\odot}$ (HD9Z1). While the collisional mass gain rates at different metallicities are comparable, the total mass loss rates peak and exceed the mass gain rates earlier, and are in general higher in the models with $Z = 0.10 Z_{\odot}$. This is mainly due to the higher wind loss rates at higher metallicities.

respectively. The considerable amount of collisional mass loss is consistent with our estimates in Appendix A. Both the collisional and wind mass losses are comparable to the mass of the formed IMBH ($M_{\bullet} = 5988 M_{\odot}$). In Fig. 10 we compare the total rates for stellar mass gain (via collisions) and mass loss (via collisions and winds). The collisional mass gain rates are calculated over time bins of $\Delta t = 0.1$ Myr. The collisional mass gain rate peaks early

with $\dot{m}_{\text{gain}} \sim 2 \times 10^{-2} M_{\odot} \text{yr}^{-1}$, between $0.1 \text{ Myr} \lesssim t \lesssim 0.2 \text{ Myr}$ after which it steadily declines. Collisions with other collisionally grown very massive stars are seen as brief peaks in the mass gain rate, although these collisions are relatively rare. For $Z = 0.01 Z_{\odot}$ the combined mass loss rate balances the mass gain rate around $t \sim 0.8\text{--}1.7$ Myr, consistent with the plateau in the mass growth history of the stars in the left panel of Fig. 9.

The most massive star at $Z = 0.10 Z_{\odot}$ gains $m_{\text{gain}} = 21621 M_{\odot}$ of material during its lifetime, and loses $m_{\text{coll}} = 6144 M_{\odot}$ and $m_{\text{wind}} = 13500 M_{\odot}$ via collisions and winds for an IMBH mass of $M_{\bullet} = 2302 M_{\odot}$. In Fig. 10 we show that the collisional mass growth rates are comparable at different metallicities despite the metallicity dependence of our stellar models, including their radii and wind rates. Due to the higher wind loss rates at higher metallicities, the combined collision and wind loss rates reach and exceed the mass gain rates already around $0.27 \text{ Myr} \lesssim t \lesssim 0.51 \text{ Myr}$. This explains why the masses of the collisionally grown stars with $Z = 0.1 Z_{\odot}$ reach their peak masses earlier than their counterparts with $Z = 0.01 Z_{\odot}$ in the left panel of Fig. 9 and result in lower overall IMBH masses at the end of the simulations.

4.2 Comparison to the dense model of Vergara et al. (2025a): the effect of wind loss rates

Recently, Vergara et al. (2025a,b) modelled the formation of a collisionally grown massive star of $\gtrsim 50000 M_{\odot}$ and an IMBH in an extremely dense isolated star cluster using NBODY6++GPU and MOCCA. Even though their cluster mass of $M_{\text{cl}} = 5.86 \times 10^5 M_{\odot}$ is by a factor ~ 2.3 higher compared to the masses of central sub-cluster of our densest models, the half mass density of their model $\rho_h = 6.99 \times 10^7 M_{\odot} \text{ pc}^{-3}$ is less than 10% higher compared to ours. The initial stellar mass function of the two models is the same while our models initially also include stars in primordial binary systems. Despite the similar initial stellar densities of our models, Vergara

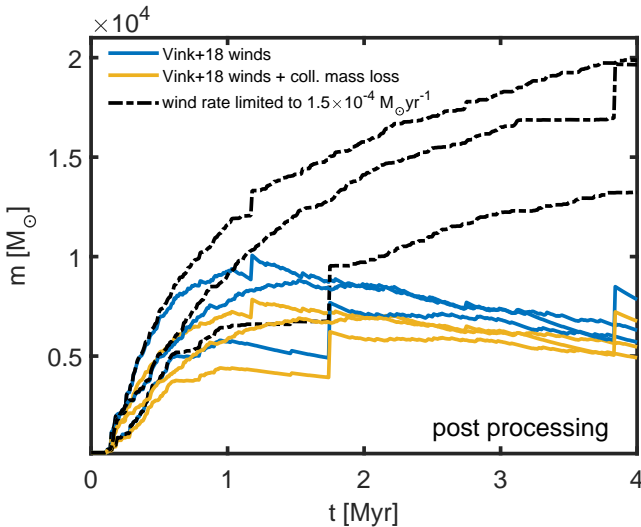


Figure 11. The post processed stellar mass evolution models from our densest simulations exploring the effect of the upper wind mass loss limit on the maximum stellar masses. The solid lines indicate simple models with collisions with and without collisional mass loss including Vink (2018) winds, capturing the overall behaviour of our full N -body models. Placing an upper limit for the stellar wind loss rate (dashed line) results in monotonic stellar mass growth beyond $20000 M_{\odot}$.

et al. (2025a) reach by a factor of ~ 7 higher peak stellar masses compared to our simulations. The growth history of their massive star is closely comparable to our models until $t \sim 0.3\text{--}0.4$ Myr. While the mass growth histories of our most massive stars plateau or turn into decline soon after this, the star of Vergara et al. (2025a) continues to monotonically grow until the end of its life at $t > 4$ Myr. Such growth history considerably differs from our models.

We identify three differences in the extremely massive star models currently employed in NBODY6++GPU, MOCCA and BIFROST to explain the differences of the maximum stellar masses in the comparably dense cluster models. These are: 1) winds, 2) collisional mass loss from the primary stars 3) the extremely massive star radii at late evolutionary stages. The assumed wind loss rates are by far the dominant driver of the differences. In Fig. 9 and Fig. 10 we showed that the mass growth of our most massive stars is quenched due to collisional and especially wind losses even though the runaway collisions continue after $t > 1$ Myr. In their level C stellar evolution for massive main sequence stars (see Kamlah et al. 2022) Vergara et al. (2025a) employ the hot O and B type line driven winds of Vink et al. (2001). Most importantly, their massive and extremely luminous stars beyond the Humphreys-Davidson limit (Humphreys & Davidson 1994) ($L_{\star}/L_{\odot} > 6 \times 10^5$ and $10^{-5} \times R_{\star}/R_{\odot} (L/L_{\odot})^{1/2} > 1$) undergo luminous blue variable (LBV) like mass loss with wind loss rates of $\dot{m}_{\text{LBV}} = 1.5 \times 10^{-4} M_{\odot} \text{yr}^{-1}$ (Belczynski et al. 2010), independent of stellar mass and metallicity. This effective ceiling sets the maximum main sequence wind mass loss rate in their models. In the Vink (2018) wind model used in our study there is no such upper limit, and increasingly massive stars have increasingly high wind loss rates in the model.

We show that applying such a upper wind rate limit of $\dot{m}_{\text{LBV}} = 1.5 \times 10^{-4} M_{\odot} \text{yr}^{-1}$ in our models results in a qualitatively similar stellar mass growth as in Vergara et al. (2025a). In Fig. 11 we perform a post processing analysis of the stars of our densest models with $Z = 0.01 Z_{\odot}$. Starting from the initial stars, we add infalling

secondary star masses m_2 at the times they collided with the massive primary in the simulations. In the basic post processed model we only apply mass gain by collisions, and wind losses according to Vink (2018). The stars are evolved using the simple model until $t = 4$ Myr. In Fig. 11 this model leads to a qualitatively similar behaviour compared to our N -body simulations: the masses of the stars reach a plateau and decrease before the end of their lives. Next, we employ a wind rate limit of $\dot{m}_{\text{max}} = 1.5 \times 10^{-4} M_{\odot} \text{yr}^{-1}$ in the simple model. For $Z = 0.01 Z_{\odot}$, the limiting wind rate is reached in our models around $m_{\star} \sim 1700 M_{\odot}$. Applying the wind rate limit we cover a qualitatively similar behaviour as seen in the model of Vergara et al. (2025a): the stars monotonically grow until the end of the lives, the most massive one reaching $20000 M_{\odot}$.

We note that our post-processed model with $m_{\text{max}} = 20000 M_{\odot}$ only represents a lower limit for the maximum stellar mass. In a full N -body simulation the increased mass of the star (compared to models in which the mass growth is quenched) would increase both the radii and gravitational focusing cross section of the star, further enhancing its growth via collisions. To verify this, we perform three isolated very dense cluster simulations in Appendix C and Fig. C1. The most massive star of the three models reaches $m_{\star} > 25000 M_{\odot}$. These test simulations strongly support our findings in the post-processed model: including the maximum wind rate limit enables monotonic collisional stellar mass growth well into the SMS regime above $\gtrsim 20000 M_{\odot}$.

The second difference between the massive star prescriptions in NBODY6++GPU, MOCCA and BIFROST is the mass loss in collisions. Vergara et al. (2025a) only apply collisional mass loss for the secondary star, and only for hyperbolic collisions. Even though their model takes the velocity of the hyperbolic collision into account while our simple model does not, their model never applies mass loss for the primary star of the collision. We have shown in Appendix A that even $< 10\%$ mass loss per collision can result in a substantial cumulative collisional mass loss during the lifetime of an extremely massive star, if collisional losses from the primary are also included in the models.

In our most dense models the collisional losses can become almost comparable to wind losses at $Z = 0.01 Z_{\odot}$. In the models without collisional mass loss, higher wind loss rates immediately after collisions compensate for the absence of the collisional ejecta. In Fig. 11, we further include the primary mass loss in stellar collisions in the simple post-processed model. The inclusion of collisional mass loss from the primary in the models only somewhat decreases the final stellar masses at $t = 4$ Myr: without the collisional mass loss the final masses are 15–16% higher.

Finally, the radii of extremely massive stars in the models included in NBODY6++GPU, MOCCA and BIFROST considerably differ late in the evolution of the stars. However, this occurs only at $t > 2$ Myr and thus does not affect the differences of mass growth between $0.3 \text{ Myr} \lesssim t \lesssim 2$ Myr discussed above. The peak stellar masses in our models are always reached before $t < 2$ Myr. At this point the radii of the extremely massive stars have their maximum values of $R_{\star} \sim 107 R_{\odot}$, consistent with the star of Vergara et al. (2025a) that has a radius of $R_{\star} \sim 100 R_{\odot}$ at $t = 1.60$ Myr. However, after this point the radius of the star begins to increase in NBODY6++GPU and MOCCA, reaching $200 R_{\odot}$, $1000 R_{\odot}$ and $10000 R_{\odot}$ at $t = 2.36$ Myr, $t = 3.25$ Myr and $t = 3.91$ Myr, respectively. The maximum radius of the $50000 M_{\odot}$ star is $2 \times 10^5 R_{\odot}$, approximately by a factor 100–1000 of larger than in our models (see Section 2.2.2). This leads to a very large difference between the collisional cross sections (by a factor of $> 10^4$) late in the evolution of the extremely massive stars between NBODY6++GPU and BIFROST, and contributes

Hierarchical model	Σ_c [10 ⁵ M _⊙ pc ⁻²]	ρ_c [10 ⁵ M _⊙ pc ⁻³]	N_{IMBH} (max)
HD1Z2	0.11	0.21	0
HD2Z2	0.17	2.04	0
HD3Z2	0.38	3.88	0–1
HD4Z2	0.54	4.90	3–5
HD5Z2	0.93	9.16	4–6
HD6Z2	1.12	13.47	4–7
HD7Z2	1.41	14.01	5–7
HD8Z2	1.96	26.9	6–9
HD9Z2	3.15	121.1	8–9

Table 6. The central stellar surface densities Σ_c and central 3D stellar densities ρ_c of the hierarchically assembled star cluster models with $Z = 0.10 Z_\odot$ at $t = 7.5$ Myr. We also show the maximum number of IMBHs with masses exceeding $M_\bullet \gtrsim 300 M_\odot$ (at any moment of time in the simulations) as N_{IMBH} . As expected, denser models result in more efficient IMBH formation. The densest low metallicity comparison simulations with $Z = 0.01 Z_\odot$ formed 9–12 IMBHs.

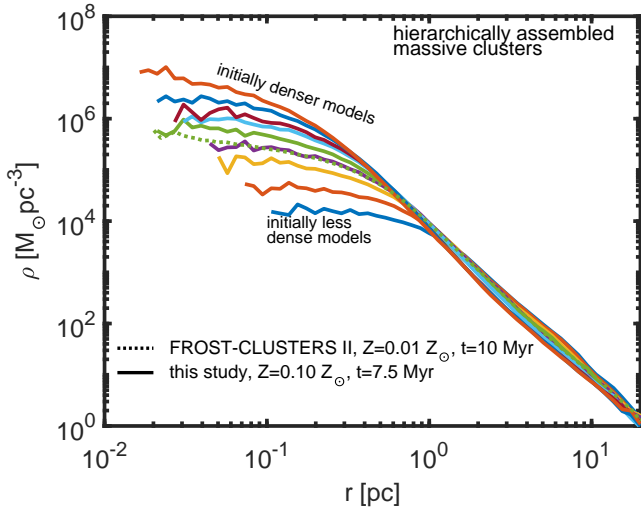


Figure 12. The 3D stellar density profiles (solid lines) of the assembling massive central star cluster at $t = 7.5$ Myr. We show for comparison the medium density low metallicity model HB-150 at $t = 10$ Myr from our previous study (Rantala et al. 2025) as the dotted line. Initially denser models result in higher final central densities, as expected, however the central densities decrease in our densest models during the simulations due to strong two body relaxation effects.

to the sustained high collisional mass gains of the extremely massive stars of Vergara et al. (2025a).

4.3 Final cluster central densities

Next, we examine the densities of the hierarchically assembled star clusters. At $Z = 0.10 Z_\odot$, the hierarchical star cluster assembly proceeds as at lower metallicities (see e.g. figure 3 of Rantala & Naab 2025). At the end of the simulations at $t = 7.5$ Myr all the sub-clusters have not merged yet with the central growing massive cluster especially in dense models in which the sub-clusters are less vulnerable for disruption. As the assembled clusters still have sub-structure and are out of equilibrium, the measured effective radii using the same recipe as in our previous study (Rantala et al.

2025) does not reliably correspond the final sizes of the assembled clusters. As the merging sub-clusters mainly deposit their stars in the outskirts of the massive central cluster later in its evolution, we can instead focus on the central stellar profiles of the assembled clusters which are less vulnerable to change compared to the outer parts.

We show the stellar density profiles of the massive assembling clusters at $t = 7.5$ Myr in Fig. 12. The illustrated profiles are averages of three random realizations of each hierarchical model. Our medium density model HD5Z2 ($Z = 0.10 Z_\odot, t = 7.5$ Myr) has initial conditions closely resembling our previous model HB-150 in Rantala et al. (2025). We show this profile from Rantala et al. (2025) at $Z = 0.01 Z_\odot, t = 10$ Myr in Fig. 12 to illustrate the profile evolution of the assembling clusters from $t = 7.5$ Myr to $t = 10$ Myr. In 2.5 Myr, the central density in the models HD5Z2 decreases (see figure 5 of Rantala et al. 2024) due to relaxation effects and stellar evolution mass losses while the remaining substructure is erased in the outer parts of the cluster. The densest assembled models reach high central densities of $\rho_c \gtrsim 10^7 M_\odot pc^{-3}$ measured within the central ~ 0.03 pc. We list the central stellar densities ρ_c and the central surface densities Σ_c in Table 6. Initially denser models have larger final central densities, as expected. The central densities of the initially dense models above $\rho_{c,\text{init}} \gtrsim 8 \times 10^5 M_\odot pc^{-3}$ decrease during the cluster assembly. For extremely dense clusters the central density initially decreases due to strong two-body relaxation effects (Binney & Tremaine 2008) at high stellar densities. This rapid evolutionary phase lasts until $t \sim 1.5$ –1.75 Myr after which the central densities more gradually decline due to relaxation and stellar evolution effects, star cluster mergers and IMBH interactions in their aftermath. The final central densities of the initially densest clusters still remain high after the cluster assembly which allows sustained TDE rates after the IMBH formation. We will discuss the TDE rates in Section 4.6.

4.4 IMBH formation and GW mergers

We list the total maximum number of IMBHs formed in each hierarchical simulation in Table 6. As expected, low density models up to HD3Z2 produce $\lesssim 1$ IMBHs per simulation. At higher densities IMBHs form more efficiently: our densest models produce $N_{\text{IMBH}} = 8$ –9 ($Z = 0.10 Z_\odot$) or $N_{\text{IMBH}} = 9$ –12 ($Z = 0.01 Z_\odot$) IMBHs depending on metallicity. The mild metallicity dependence is consistent with our results from the isolated star cluster parameter study. Even in the densest models low mass clusters below $M_{\text{cl}} \lesssim 6 \times 10^3 M_\odot$ do not form IMBHs. This highlights the critical role of massive stars ($m_\star \gtrsim 100 M_\odot$), which the low mass cluster models lack, in initiating the runaway collision cascades. However, above this critical mass threshold the IMBH masses are well described only by the cluster surface density and metallicity as seen in our isolated parameter study and Rantala et al. (2025).

Before $t = 7.5$ Myr, in total eight GW driven mergers occur in our hierarchical simulations. These all occur in the setups with the two highest densities: H8D9Z2, H8D9Z1 and H8D9Z2. In the models HD8Z2 there is a single IMBH-IMBH merger with masses $M_\bullet = 744 M_\odot$ and $M_\bullet = 562 M_\odot$ ($q = 0.76$). The rest of the seven GW driven mergers occur between stellar BHs and IMBHs with primary IMBH masses in the range of $743 M_\odot \lesssim M_\bullet \lesssim 3384 M_\odot$ with mass ratios $0.02 \lesssim q \lesssim 0.06$. However, the IMBH interaction phase and merger phase is just beginning at $t = 7.5$ Myr. In our previous studies (e.g. figures 6–8 in Rantala et al. 2024) a large fraction of black hole interactions and GW driven mergers occurred between $7.5 \text{ Myr} \leq t \leq 50 \text{ Myr}$ in the simulations.

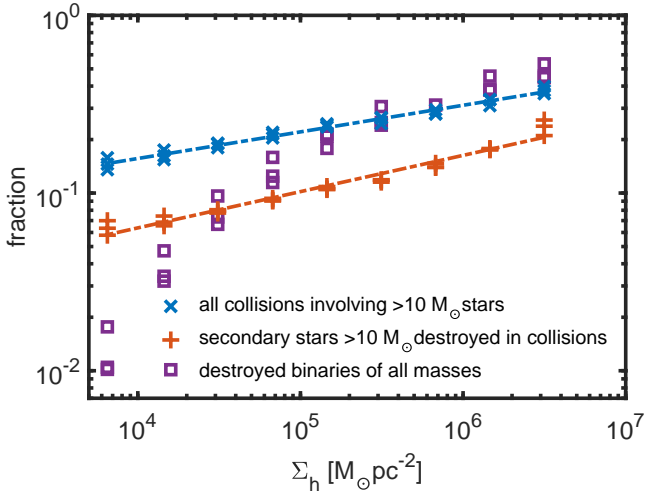


Figure 13. The fraction of destroyed binary systems (square symbols) and potential supernova progenitors (plus symbols) as a function of the host star cluster surface density. Up to $\sim 40\%$ of all supernova progenitors (cross symbols) can experience a stellar collision in the densest clusters.

At $t = 7.5$ Myr, the centres of the low density $Z = 0.10 Z_{\odot}$ setups HD1Z2–HD3Z2 do not contain any IMBHs. For the intermediate density models HD4–HD7 the typical cluster centre contains an IMBH-IMBH binary (58% of the models), a single IMBH (25%) or no IMBHs (17%). In the highest density models central IMBH binaries and triples are the most common central IMBH configurations. Triple systems can occur more frequently in denser models as they produce the largest number of IMBHs, and dense stellar environments enable short sinking timescales in the aftermath of star cluster mergers. Rapid GW driven mergers in these densest models are expected as especially the triples are efficient in driving IMBH-IMBH mergers (e.g. Liu et al. 2024; Rantala & Naab 2025). Moreover, the high central stellar densities up to $\rho_c \gtrsim 10^7 M_{\odot} pc^{-3}$ enable faster stellar dynamical hardening of IMBH-IMBH binaries by stellar three body ejections compared to lower density clusters (Sovaitzis et al. 2025).

4.5 Destruction of massive stellar binaries and supernova progenitors

The extremely dense models of massive star clusters are particularly hostile environments for the longevity of massive initial (primordial) stellar binaries. In our initial conditions we use the same stellar binary population properties regardless the star cluster density. The higher destruction rate of more massive stellar binaries in denser models originates from the shorter mass segregation and dynamical friction timescales in denser environments. In our models, $> 90\%$ of stars with $m_{\star} \geq 10 M_{\odot}$ are initially members of binary systems. At the centres of the clusters, the frequent interactions with stars and later stellar BHs and IMBHs can unbind binary components, or drive them into merging with each other. The surviving massive stellar binaries evolve into BH-BH binaries which are potential future gravitational wave sources in their host clusters. Whereas our lowest density models HD1Z2 contain 81 stellar BH-BH binaries at $t = 7.5$ Myr, the corresponding highest density models HD9Z2 only have 2–3. Moreover, stellar binaries with both components in a BH progenitor mass range of $\gtrsim 19 M_{\odot}$ are ~ 5 times more numerous in the models HD1Z2 compared to HD9Z2. A similar trend is

observable in the overall stellar binary content of the assembled star clusters. We illustrate this is in Fig. 13. In our densest models 53% of the binaries are destroyed during the first $t = 7.5$ Myr, especially in the inner parts of the assembled clusters (see figure 10 of Rantala et al. 2025). Meanwhile, the least dense models only have 1–2% of their binaries destroyed.

We note that stellar mergers in stellar mass binaries or with the extremely massive stars can destroy a substantial number of the massive stars ($\geq 10 M_{\odot}$) initially present in the clusters. This can lead to depletion of single stellar BH (Paiella et al. 2025) and core collapse supernova progenitors in the clusters. We show in Fig. 13 both the fraction of $\geq 10 M_{\odot}$ stars that participated in any collisions, and $\geq 10 M_{\odot}$ stars which were destroyed as the secondary stars of the stellar mergers. As our models contain close initial binaries, the fraction of destroyed $\geq 10 M_{\odot}$ stars is 6–7% for our low density models with $\Sigma_h \lesssim 10^4 M_{\odot} pc^{-2}$. However, the fraction of destroyed massive stars rapidly increases as a power-law function of increasing cluster surface density, and 21–26% of the $\geq 10 M_{\odot}$ secondary stars are destroyed in our densest models. In total, up to $\sim 40\%$ of stars more massive than $\geq 10 M_{\odot}$ participate in a collision as a primary or a secondary star. The destruction of $> 10 M_{\odot}$ stars is compensated (up to $\sim 50\%$ in the densest models) by the generation of new $> 10 M_{\odot}$ stars in the collisions of lower mass stars.

The overall stellar wind and collisional ejecta losses are enhanced by the stellar collisions in dense environments while simultaneously the supernova energy budget may be decreased by 20–40% in the densest systems. Furthermore, in addition to being suppressed, the release of supernova energy is on average delayed in high density clusters. Between $t = 3$ Myr and 5 Myr, the number of stars that reach the end of their lives is only 10%–40% in the dense models HD9Z2 compared to the low density models HD1Z2. Similarly, the early radiation feedback from massive interacting binary stars is prevented in the densest environments as the binaries merge or become unbound. Overall, the enhanced enrichment together with the suppressed and delayed feedback may help to produce enriched stellar populations in dense environments. However, we note that the suppression and delay of the supernova energy release and binary star radiation feedback is accompanied by the extreme radiation field of $> 100 M_{\odot}$ – $1000 M_{\odot}$ produced in the collisions. The cumulative wind and collisional ejecta budgets of the models are examined in Section 5.

4.6 Rates for stellar collisions and TDEs

We show the very and extremely massive star ($m_{\star,1} + m_{\star,2} > 150 M_{\odot}$) collision rates Γ_{coll} and the IMBH ($M_{\bullet} > 100 M_{\odot}$) TDE rates Γ_{TDE} as a function of time in Fig. 14. At comparable cluster densities of $\Sigma_h \sim 1$ – $2 \times 10^5 M_{\odot} pc^{-2}$, both the maximum very massive star collision rates and the TDE rates are by a factor of few lower in our models HD5Z2 compared to our previous studies (models HB-150 in Rantala et al. 2025). This is mostly due to the somewhat lower IMBH masses in the current runs as we now assume stronger winds and collisional mass loss at $Z = 0.10 Z_{\odot}$ compared to our setups in Rantala & Naab (2025) and Rantala et al. (2025).

In the hierarchical low density models (HD1Z2–HD2Z2) the only collisions beyond the mass limit of $150 M_{\odot}$ occur after $t > 2.25$ Myr when individual binaries merge late in their evolution. In models with intermediate densities (HD3Z2–HD4Z2) the peak VMS and EMS collision rate occur between ~ 1.5 Myr $\lesssim t \lesssim 3$ Myr as in our previous studies. However, in our densest models (HD6Z2

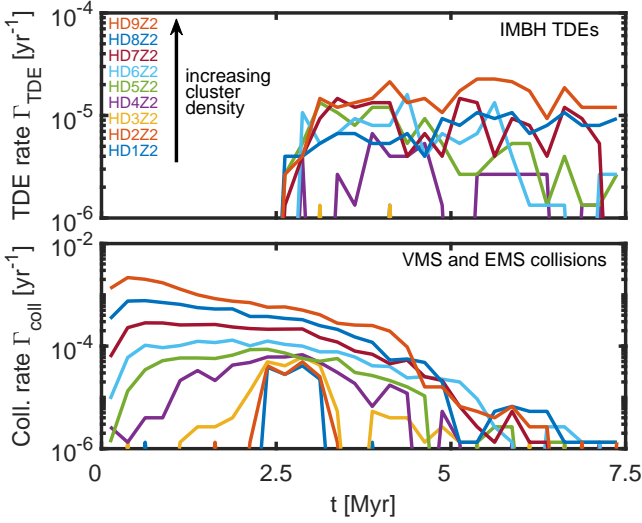


Figure 14. Top panel: the IMBH TDE rates Γ_{TDE} in the hierarchical models HD1Z2–HD9Z2. In the densest models the TDE rates $\Gamma_{\text{TDE}} > 10^{-5} \text{ yr}^{-1}$ can be sustained from the IMBH formation until the end of the simulations at $t = 7.5$ Myr. Bottom panel: the rates of VMS and EMS collisions in the hierarchical models. In the densest models the maximum collision rates reach $\Gamma_{\text{coll}} \sim 2 \times 10^{-3} \text{ yr}^{-1}$.

and denser) the collision rates are already initially high due to the extremely high stellar densities of the models. The peak VMS collision rate in our densest hierarchical models HD9Z2 reach $\Gamma_{\text{coll}} \sim 2.2 \times 10^{-3} \text{ yr}^{-1}$ per assembling cluster. The VMS collision rates rapidly decline after $t \gtrsim 4$ –5 Myr after the most massive stars end their lives. Similarly, IMBH TDEs commence after $t \gtrsim 2.5$ Myr after the IMBH formation commences. The maximum collision and TDE rates by IMBHs in models HD9Z2 are $\Gamma_{\text{coll}} \sim 2.2 \times 10^{-3} \text{ yr}^{-1}$ and $\Gamma_{\text{TDE}} \sim 2.3 \times 10^{-5} \text{ yr}^{-1}$ per assembling cluster. While in Rantala et al. (2025) our peak TDE rates rapidly declined after 1–2 Myr of the IMBH formation, the TDE rates remain relatively constant after the IMBH formation in our densest models until the end of the simulations. The sustained TDE rates compared to our previous studies are enabled by up to an order of magnitude higher maximum central stellar densities in this study. The central (≤ 0.1 pc) cluster densities of $\rho_c \gtrsim 10^7 \text{ M}_\odot \text{ pc}^{-3}$ and velocity dispersions of $\gtrsim 30 \text{ km s}^{-1}$ may be high enough to sustain long term runaway IMBH growth via TDEs (Rizzuto et al. 2023; Stone et al. 2017), enabling TDE driven IMBH growth beyond $M_\bullet > 10^4 \text{ M}_\odot$ (see e.g. Alexander & Bar-Or 2017b).

5 WIND AND COLLISIONAL EJECTA MASS LOSS BUDGETS

5.1 Cumulative rates of winds and collisional ejecta

5.1.1 Winds

As shown in Section 4.1, the very massive stars built up by stellar collisions may lose up $\sim 20000 \text{ M}_\odot$ via winds and collisional ejecta during their lifetimes, the total lost masses exceeding the final IMBH masses by a factor of few. We now examine the total budget of mass loss from the entire stellar population of the assembling clusters in more detail.

We present the total cumulative losses in winds and collisions in the hierarchical cluster assembly models in Fig. 15. There are

in total 27 clustered setups at $Z = 0.10 \text{ Z}_\odot$ with nine different initial densities, three random realizations each. The densest model is also simulated using a lower metallicity of $Z = 0.01 \text{ Z}_\odot$. In the left panel of Fig. 15, at low and intermediate cluster densities (models HD1Z2–HD5Z2 with $Z = 0.10 \text{ Z}_\odot$) the total cumulative wind losses are very similar. The cumulative wind losses gradually increase until $t \sim 2.4$ Myr after which the wind rates rapidly rise as massive stars reach the final stages of their lives. In a hierarchical system of $M_\star = 10^6 \text{ M}_\odot$, the total wind losses at $t = 7.5$ Myr are $m_{\text{wind}} \sim 3$ – $4 \times 10^4 \text{ M}_\odot$. Even though stars can grow by collisions and IMBHs form in the models HD3Z2–HD5Z2, the total wind output of these massive stars is still small comparable to the rest of the stellar population. In denser systems the situation changes. Starting from HD6Z2 a small number of individual extremely massive stars comprise a large fraction of the wind mass loss budget, and the cumulative loss histories of the clusters begin to deviate from the low density clusters when extremely massive stars first form and exceed $\gtrsim 600 \text{ M}_\odot$. This behaviour is especially visible in the densest initial setups. The maximum cumulative wind mass reached by $t = 7.5$ Myr is $m_{\text{wind}} \sim 4.8 \times 10^4 \text{ M}_\odot$ with a single extremely massive star contributing almost 30% of this. In the dense low metallicity models (HD9Z1 with $Z = 0.01 \text{ Z}_\odot$) the cumulative wind masses are initially by a factor of ~ 5 lower compared to the $Z = 0.10 \text{ Z}_\odot$ setups. By the end of the simulations the maximum wind losses can still reach $\sim 3 \times 10^4 \text{ M}_\odot$, a factor of ~ 1.6 lower compared to the higher metallicity models. The relatively high total wind output in the low metallicity model is due to the fact that at low metallicities the runaway collisions and total losses are balanced at higher stellar masses. The higher m_\star compensates for the lower Z in the wind loss rates.

Young massive star clusters are expected to expel their remaining gas content around $t \sim 3$ Myr due to the first supernovae exploding in the systems. We show the cumulative wind losses at $t = 3.0$ Myr in Fig. 16 as a function of the central sub-cluster half mass surface density Σ_h for $Z = 0.10 \text{ Z}_\odot$ and for the densest model also at $Z = 0.01 \text{ Z}_\odot$. The results are normalized by the total initial stellar mass of the clusters in the region $M_{\text{cl},0} \sim 10^6 \text{ M}_\odot$. For comparison, we display the expected total wind losses at $Z = 0.01 \text{ Z}_\odot$ and 0.10 Z_\odot in the case of no collisions, assuming the stellar masses in our initial conditions and single stellar evolution using the PARSEC stellar tracks in SEVN. At $Z = 0.01 \text{ Z}_\odot$, $m_{\text{wind}}/M_{\text{cl},0}$ for the single population without collisions is ~ 5 – 6×10^{-4} while at $Z = 0.10 \text{ Z}_\odot$, $m_{\text{wind}}/M_{\text{cl},0} \sim 5 \times 10^{-3}$. In the actual simulations the total wind losses are somewhat higher ($m_{\text{wind}}/M_{\text{cl},0} \sim 7 \times 10^{-3}$) due to binary star mergers forming more massive stars in the models. Above $\Sigma_h \gtrsim 1$ – $2 \times 10^5 \text{ M}_\odot$ the relative wind losses increase, reaching $m_{\text{wind}}/M_{\text{cl},0} \sim 0.02$ by $t = 3.0$ Myr. For models with $Z = 0.01 \text{ Z}_\odot$ the relative wind losses at $t = 3.0$ Myr are somewhat lower, $m_{\text{wind}}/M_{\text{cl},0} \sim 9 \times 10^{-3}$.

5.1.2 Collisional ejecta

Substantial amounts of stellar material can be lost via ejecta in stellar collisions, decreasing the masses of the formed IMBHs but simultaneously providing enriched material processed by the stars. Whereas the total cumulative wind losses are very similar in low and intermediate density clusters the cumulative collisional ejecta rates show a strong dependence on the initial cluster densities. We illustrate this in the right panel of Fig. 15 first focusing on the models with $Z = 0.10 \text{ Z}_\odot$. In our models with the lowest initial density, stellar collisions occur predominantly in evolved massive binaries late in their evolution with final cumulative collisional ejecta masses

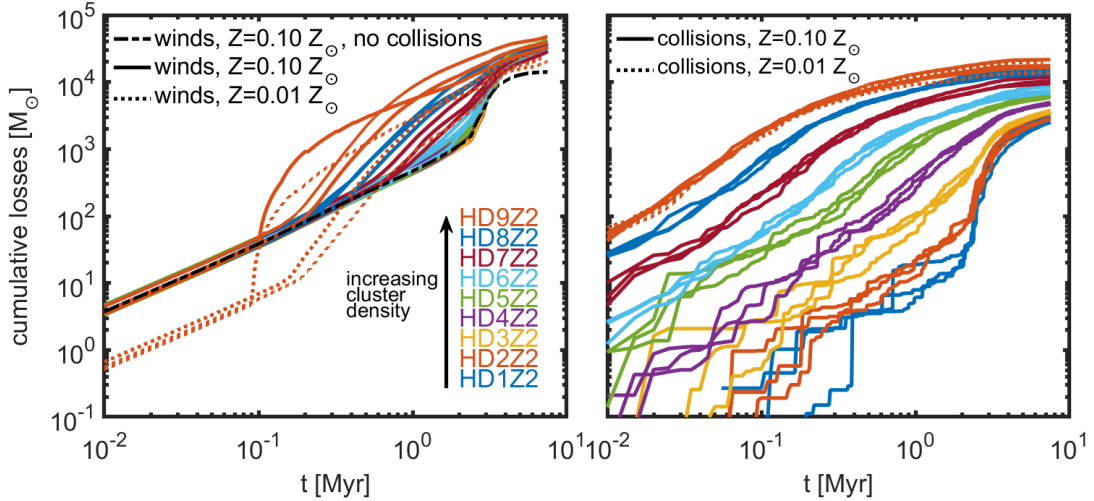


Figure 15. The cumulative mass loss rates from the stars through winds (left panel) and by collisional ejecta (right panel) in the hierarchical setups of different initial densities. The nine models with $Z = 0.10 Z_{\odot}$ are displayed using the solid line while the densest comparison setup with $Z = 0.01 Z_{\odot}$ is shown as the dotted line. At $0.10 Z_{\odot}$ the total wind losses in the models are very similar at different densities until the setup HD6Z2 after which individual extremely massive stars begin to dominate over the mass loss budget of the stellar population. At the low metallicity the wind losses are weaker, as expected. The cumulative amount of collisional ejecta strongly depends on the cluster density, and at early times and in the low metallicity model exceeds the total mass of the wind material. The collisional losses are very similar in the models with $Z = 0.10 Z_{\odot}$ and $0.01 Z_{\odot}$.

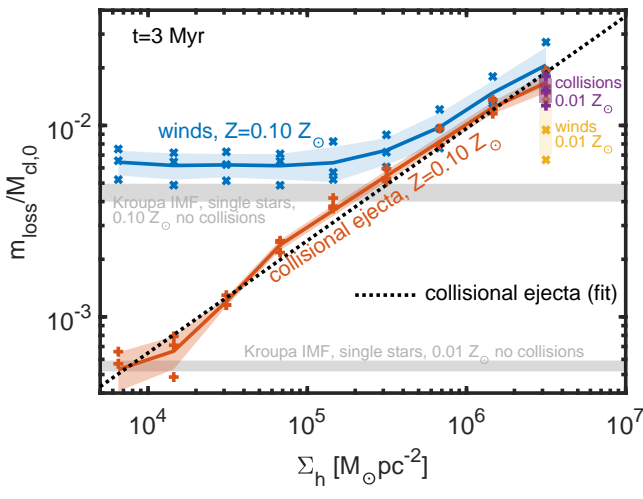


Figure 16. The total mass losses in winds and stellar collisions per initial stellar mass $m_{\text{loss}}/M_{\text{cl},0}$ as a function of the central cluster surface density Σ_h in the models with $Z = 0.10 Z_{\odot}$. In low density models up to $\Sigma_h \sim 1 - 2 \times 10^5 M_{\odot} \text{ pc}^{-2}$ the wind losses are relatively constant ($m_{\text{loss}}/M_{\text{cl},0} \sim 7 \times 10^{-3}$) after which the total losses rise due to extremely massive star formation at high cluster densities. The collisional losses scale with the cluster densities following a power-law relation. In the densest models with $Z = 0.01 Z_{\odot}$ (top right corner) the amount of collisional ejecta exceeds the wind losses. We also show the expected amount of mass loss for a single population without any collisions as the horizontal shaded regions.

reaching $m_{\text{coll}} \sim 2500 M_{\odot}$ at $t = 7.5$ Myr. With increasing cluster densities the cumulative ejecta masses steadily increase and shift towards earlier times, reflecting the mass segregation timescales of the clusters. Whereas the wind output of the stellar populations

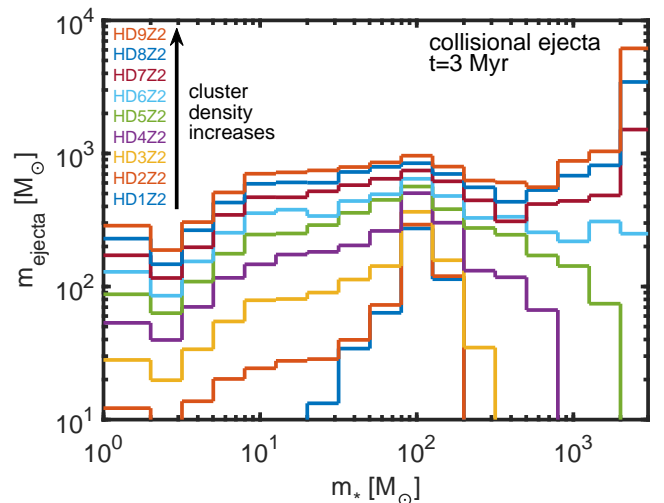


Figure 17. The amount of collisional ejecta originating from stars of different (ZAMS) masses. The shown lines are averages of three random realizations of each modelled cluster density. The amount of collisional ejecta steadily increases with increasing density in each stellar mass bin, starting from $\sim 100 M_{\odot}$ stars, extending to low mass stars first and after the model HD4Z2 towards the high mass stars. Most notably, in very dense models (HD6Z2 and above), the largest contribution to the collisional ejecta budget comes from extremely massive stars above $\gtrsim 2000 M_{\odot}$.

increases after a few Myr as massive stars evolve, the situation is opposite for the collisional ejecta. The highest rates of collisional ejecta losses coincide with the peak collision rates that occur early before $t < 2$ Myr (see Fig. 10). By $t = 7.5$ Myr, the densest models output in total $m_{\text{coll}} \gtrsim 21500 M_{\odot}$. While the cumulative wind

losses showed a substantial dependence on the cluster metallicity, the collisional ejecta losses in the models with $Z = 0.01 Z_{\odot}$ and $Z = 0.10 Z_{\odot}$ follow almost identical evolution.

We show the cluster surface density dependence of the total collisional ejecta masses at $t = 3$ Myr normalized by the zero age stellar mass of the clustered region $M_{\text{cl},0}$ in Fig. 16. At $Z = 0.10 Z_{\odot}$, the $m_{\text{coll}}/M_{\text{cl},0}$ monotonically increases with the cluster surface density and can be well fitted with a power-law of

$$\log_{10} \left(\frac{m_{\text{coll}}}{M_{\text{cl},0}} \right) = 0.59 \log_{10} \left(\frac{\Sigma_{\text{h}}}{M_{\odot} \text{ pc}^{-2}} \right) - 5.53. \quad (12)$$

Below surface densities of $\Sigma_{\text{h}} \lesssim 2-3 \times 10^5 M_{\odot} \text{ pc}^{-2}$ at $Z = 0.10 Z_{\odot}$ the winds are always the most important enrichment channel. In the densest models the final relative ejecta losses are $m_{\text{coll}}/M_{\text{cl},0} \sim 0.016$, comparable to the total wind losses in the models. At $Z = 0.01 Z_{\odot}$ the results for the ejecta are very similar, however, the wind losses are by a factor of few lower in our low metallicity models. As the collisional ejecta rates show little metallicity dependence, we expect that our models with $Z = 0.01 Z_{\odot}$ closely follow Eq. (12) for the ejecta as well. Thus, at $t = 3.0$ Myr at $Z = 0.01 Z_{\odot}$ the collisional ejecta is likely the dominant enrichment channel in all but the few lowest density models.

Finally, we note that only $\sim 50\%$ of the initial stellar mass of the hierarchical cluster assembly region ends up in the central regions of the final assembled star clusters (Rantala et al. 2025). As massive stars sink to the centres of their host sub-clusters, the wind losses and collisions occur in environments that most likely end up in the central assembling cluster as opposed to being stripped up to the diffuse outer envelope of the system. Thus, we expect that the total wind and collision losses normalized by the final cluster mass are approximately two times larger than $m_{\text{wind}}/M_{\text{cl},0}$ and $m_{\text{coll}}/M_{\text{cl},0}$, up to $\sim 4-5\%$ in the densest clusters, together reaching up to 10% at $Z = 0.10 Z_{\odot}$.

5.2 Which stars pollute via collisional ejecta?

In the previous section we analyzed the total amount of collisional ejecta from stellar collisions regardless from which stars the ejecta originates from. The masses of the stars responsible for the ejecta are important as their mass and age determines the central stellar temperature, the occurring nuclear fusion processes, and ultimately the surface composition of the stars. While a detailed element-by-element enrichment calculation is beyond the scope of this work, we next examine the mass distribution of the stars from which the collisional ejecta originates from. For the stellar mass label we always use the ZAMS mass of the star, fixed by the initial conditions or determined by the stellar collision routines via the SEVN track switcher. For the analysis we use 15 logarithmically spaced stellar mass bins between $2 M_{\odot} \lesssim m_{\star} \lesssim 2000 M_{\odot}$ and one bin below ($m_{\star} \lesssim 2 M_{\odot}$) and above ($m_{\star} \gtrsim 2000 M_{\odot}$) the mass range.

The resulting histogram for the cumulative collisional ejecta losses is shown at $t = 3.0$ Myr in Fig. 17. At low densities (model HD1Z2) most of the ejecta originates from $m_{\star} \sim 100 M_{\odot}$ stars as the most massive stars. Towards higher densities, the distribution first extends towards lower stellar masses (models HD2Z2 and HD3Z2), and after model HD4Z2 also towards the extremely massive star range as they begin to form in numbers at sufficiently high densities. This picture changes around the model HD6Z2 with an initial threshold surface density of $\Sigma_{\text{h}} \sim 2-4 \times 10^5 M_{\odot} \text{ pc}^{-2}$. After this threshold surface density the extremely massive stars dominate the ejecta mass budget, and most of the collisional ejecta origi-

nates from few stars colliding with a large number of low mass companions.

5.3 Discussion: peculiar GC enrichment patterns

The increased mass-loss rates enabled by the collisionally growing stars over just a few Myr may have important implications for chemical enrichment in the cluster-forming regions (e.g. Wang et al. 2020a). Lahén et al. (2024) argued, based on an extrapolation of a hydrodynamical star-formation simulation, that wind enrichment on a level of a few per cent in a $M_{\text{cl}} = 2 \times 10^5 M_{\odot}$ cluster could produce some notably chemically peculiar stars ($\Delta \text{Na/Fe} \gtrsim 0.2-0.3$) in the core region of the cluster even with normal VMS winds. For a single EMS or SMS the chemical enrichment would indeed occur very concentrated in the core of the cluster. The chemical output of convective EMSs or SMSs (Denissenkov & Hartwick 2014; Charbonnel et al. 2023) mixed with the pristine ISM would provide a good match to the range of chemical variations in multiple populations of massive star clusters. In our models such transition from mostly VMS wind pollution to the regime dominated by individual EMSs (and SMSs depending on the wind rate model) occurs at cluster surface densities around $\Sigma_{\text{h}} \sim 2-4 \times 10^5 M_{\odot} \text{ pc}^{-2}$. Using the star-by-star distribution of wind mass fractions per cluster obtained in Lahén et al. (2024), assuming that 2% (5%) of the cluster mass is recycled, and that the most extreme abundance ratios for [Al/Fe] describe the SMS wind composition, we approximate that 4% (7%) of the stars in such a cluster would be considered as second population with $\Delta \text{Na/Fe} \gtrsim 0.3$. The number of stars with large offsets from the pristine composition would still be sub-dominant unless the mass fraction of recycled material was even larger or a fraction of the pristine stars were removed e.g. due to dynamical evolution, to change the number ratio. On the other hand, such peculiar stars have been observed to be the minority in GCs of relatively low initial mass (Gratton et al. 2019). A more direct abundance analysis with long-term dynamical evolution model for the cluster would be needed to quantify this population ratio in more detail.

6 THE COSMIC FORMATION RATE OF IMBHs CREATED BY RUNAWAY COLLISIONS

6.1 Model assumptions

Estimates for the cosmic BH and IMBH formation rate density via different channels and the BH-BH merger rate have been widely provided using semi-analytic and Monte Carlo approaches (Mapelli et al. 2017; Arca Sedda & Mastrobuono-Battisti 2019; Arca Sedda et al. 2020; Santoliquido et al. 2020, 2021; Sicilia et al. 2022; Arca Sedda et al. 2023a) including Pop-III models (Tanikawa et al. 2021, 2022). We now proceed to formulate such a model for the volumetric IMBH formation rate based on our simulations. In Section 4 we demonstrated that the runaway stellar collisions can lead to the formation of IMBHs in dense, clustered environments at $Z = 0.1 Z_{\odot}$. Our isolated simulation results in Section 3 suggest that the process should in principle be possible up to metallicities at least $0.2-0.3 Z_{\odot}$. As star formation at $Z = 0.1 Z_{\odot}$ is considerably more common than at $Z = 0.01 Z_{\odot}$ throughout the history of the Universe (e.g. Moster et al. 2018; Chrušlińska & Nelemans 2019; Pakmor et al. 2022), it is plausible that most IMBHs could form in environments of relatively high metallicities, provided that the star clusters at formation are dense enough. In this section we present a simple model to qualitatively explore this possibility.

Our model for the cosmic IMBH formation rate density ($\mathcal{R}_{\text{IMBH}}$) is based on the following assumptions. First, we need a model for the cosmic star formation rate (SFR) density (SFRD; Hopkins & Beacom 2006; Madau & Dickinson 2014) up to $z = 15$ and its metallicity dependence SFRD(Z). For this, we use the recent models of Chruścińska et al. (2025), which extend and validate the observation-based framework of Chruścińska & Nelemans (2019); Chruścińska et al. (2021) against more recent and additional empirical constraints. Chruścińska et al. 2025 describe the cosmic SFRD as a function of iron abundance (i.e. the element governing metallicity effects on stellar evolution) and introduce several model variations to bracket the main uncertainties in their estimates. For our fiducial SFRD(Z), we select their model variation that assumes no evolution in the low-mass end of the galaxy stellar mass function (GSMF) at high redshifts, and otherwise combines assumptions that maximise the fraction of SFRD occurring at low metallicity. The selected model variation adopts a logarithmic slope $\alpha_{\text{SFR}} = 0.8$ for the galaxy stellar mass–SFR relation, along with the mass - gas-phase (oxygen) metallicity relation with a low-normalization at low redshift from Curti et al. (2020). To convert gas-phase oxygen abundances to iron abundances, it further employs the relation between the oxygen-to-iron abundance ratio and the specific SFR of galaxies (Chruścińska et al. 2024), following the "slow" iron enrichment scenario from Chruścińska et al. 2025. The SFRD(Z) at $10 < z < 15$ is obtained by extrapolating the Chruścińska et al. (2025) models. Furthermore, we assume that all high redshift ($z > 10$) star formation occurs at metallicities below $\lesssim 0.10 Z_{\odot}$.

There is considerable uncertainty in the metallicity dependence of the cosmic SFRD. In particular, the assumed GSMF slope becomes important when galaxies with stellar masses $M_{\star} < 10^8 M_{\odot}$ (which may considerably contribute to low metallicity SFR) are taken into account in the SFRD(Z) models. The fixed GSMF slope leads to a strong decline of the SFRD at redshifts $z > 2$ even when the models are extrapolated to galaxy masses of $M_{\star} = 10^6 M_{\odot}$ (see the bold dashed line in the right panel of figure 6 in Chruścińska et al. 2025). However, recent studies point to steepening of the low-mass GSMF slope with redshift (Davidzon et al. 2017; Weibel et al. 2024; Navarro-Carrera et al. 2024), which leads to a much more gradual decrease in SFRD at high redshifts and higher integrated stellar mass formed at low metallicity. We examine the consequences of uncertainties in the SFRD(Z) models to the cosmic IMBH formation rate densities in Appendix D.

Next, we select the cluster formation efficiency Γ , or the fraction of stellar mass formed in clusters. For simplicity we treat Γ as a constant and set $\Gamma = 0.3$ (e.g. Chandar et al. 2017) even though observations indicate that Γ might vary in different environments (Adamo et al. 2020) and likely increases towards high redshifts (Vanzella et al. 2025). The $\mathcal{R}_{\text{IMBH}}$ model results linearly depend on the cluster formation efficiency and can be obtained for any other Γ via simple linear scaling, including redshift dependence. We assume that the star clusters follow the universal power-law -2 mass function (Elmegreen & Efremov 1996; Zhang & Fall 1999; Adamo et al. 2020; Lahén et al. 2020) from $M_{\text{cl}} = 150 M_{\odot}$ up to $M_{\text{cl}} = 10^7 M_{\odot}$. We further assume that any massive star cluster above $M_{\text{cl}} \geq 10^4 M_{\odot}$ assembled hierarchically from sub-clusters that also followed a universal power-law -2 mass function. Most importantly, our estimates require assuming the mass size relation of the star clusters at birth, i.e. their initial stellar (surface) density. Besides the metallicity, this assumption has a major effect on the number density of the formed IMBHs. While the half-light radii of local young ($\lesssim 10\text{--}100$ Myr) massive star clusters (e.g. Brown & Gnedin 2021) as well as lensed proto GCs up to $z \sim 10$ (Adamo

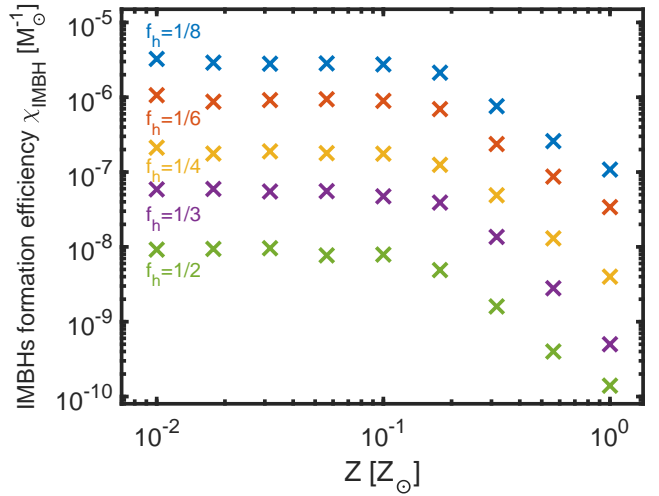


Figure 18. The IMBH formation efficiency χ_{IMBH} per unit of star formation as a function of metallicity Z calculated using the model from Section 6. The IMBH formation efficiency, but not its dependence on metallicity, sensitively depends on the normalization of the cluster mass radius relation f_h . For a fixed f_h , χ_{IMBH} remains at low metallicities constant up to $Z = 0.1 Z_{\odot}$ above which it steadily declines by a factor of ~ 30 towards $Z = 1.0 Z_{\odot}$.

et al. 2024; Abdurro'uf et al. 2025) can be determined, the direct observations of the star cluster birth radii remain challenging even in the local Universe. Still, the comparison of local YMC and ancient GC densities suggests that the initial stellar densities of star clusters formed at early cosmic epochs were higher than at present day. Consequently, we adopt a two-stage approach. In our first set of models we assume that the cluster mass-size relation at birth (and consequently the cluster densities for fixed M_{cl}) is the same at all redshifts. Specifically, we explore the different normalizations $f_h = 1, 1/2, 1/4$ and $1/8$ of the $M_{\text{cl}}-R_e$ relation as in Eq. (7). In a second set of models we assume that the normalization of this relation evolves with redshift (e.g. Messa et al. 2024) following a simple parametrization as $f_h(z) = f_h(z = 0) + k_z z$ with k_z chosen such a way that clusters at $z = 10$ are up to by a factor of 8 more compact at birth than their $z = 0$ counterparts. For redshifts above $z > 10$ we use the model for the cluster mass size relation at $z = 10$. Finally, we populate the star clusters with IMBHs using the fitting formulas from our N -body simulations. For the probability of IMBH formation we use an approach based on the logistic function motivated by Fig. 3. For the IMBH masses in each sub-cluster we use our models of Eq. (9) and Eq. (10).

6.2 The IMBH formation efficiency in the model

We show the IMBH formation efficiency χ_{IMBH} , i.e. the number of IMBHs formed per solar mass of star formation, as function of metallicity in Fig. 18. The IMBH formation efficiency sensitively depends on the assumed normalization of the cluster mass – radius relation. With the normalization $f_h = 1/8$, $\chi_{\text{IMBH}} \sim 3 \times 10^{-6} M_{\odot}^{-1}$ below $Z \lesssim 0.10 Z_{\odot}$. Towards $Z = 1.0 Z_{\odot}$ the IMBH formation efficiency drops by a factor of $\gtrsim 30$. With increasing initial cluster sizes, the IMBH formation efficiency, even at metallicities below $Z \lesssim 0.10 Z_{\odot}$, decreases, approximately by a factor of 15–20 per a factor of 2 in f_h . For $f_h = 1/4$, $\chi_{\text{IMBH}} \sim 1.9 \times 10^{-7} M_{\odot}^{-1}$, and for $f_h = 1/2$, $\chi_{\text{IMBH}} \sim 8.8 \times 10^{-9} M_{\odot}^{-1}$. The low metallicity cluster density dependence can be characterized with an empirical

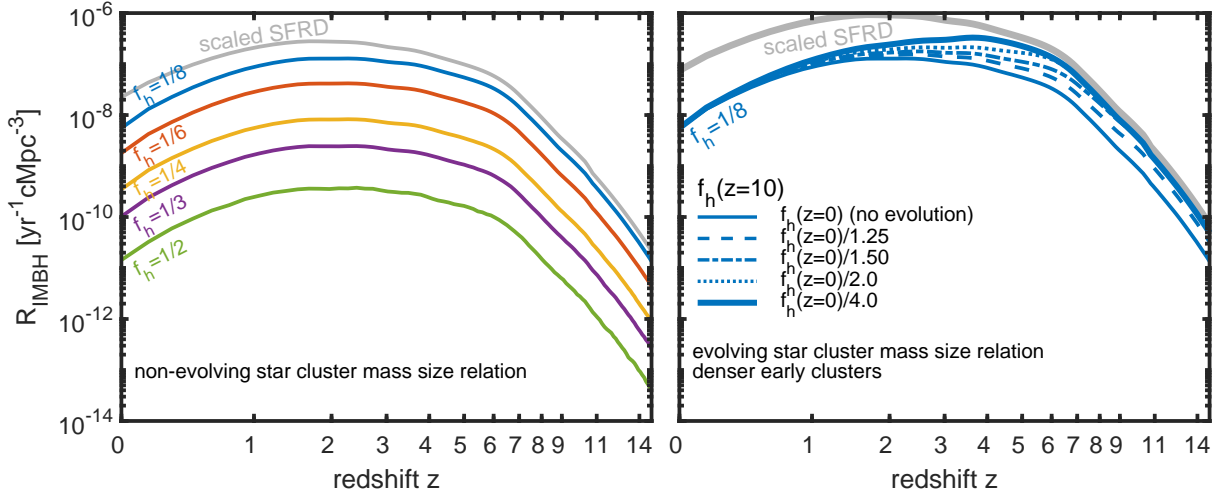


Figure 19. The cosmic formation rate densities of IMBHs $\mathcal{R}_{\text{IMBH}}$. Left panel: the case of the fixed non-evolving normalization f_h of the star cluster birth mass radius relation. The $\mathcal{R}_{\text{IMBH}}$ sensitively depends on the initial cluster densities through f_h . With $f_h = 1/8$, $\max \mathcal{R}_{\text{IMBH}} \sim 10^{-7} \text{ yr}^{-1} \text{ cMpc}^{-3}$, and the maximum $\mathcal{R}_{\text{IMBH}}$ declines over by and order of magnitude per a factor of 2 in f_h . The overall $\mathcal{R}_{\text{IMBH}}$ history follows the low metallicity SFRD, not the total SFRD, but still peaks around the cosmic noon at $z \sim 2.3$. Right panel: fixed $f_h(z = 0) = 1/8$ with five models with increasingly small cluster birth radii towards $z = 10$. In the evolving models the highest IMBH formation rates are boosted by a factor of $\sim 2\text{--}3$, and the $\mathcal{R}_{\text{IMBH}}$ peak becomes narrower as well as gradually move towards $z = 4$.

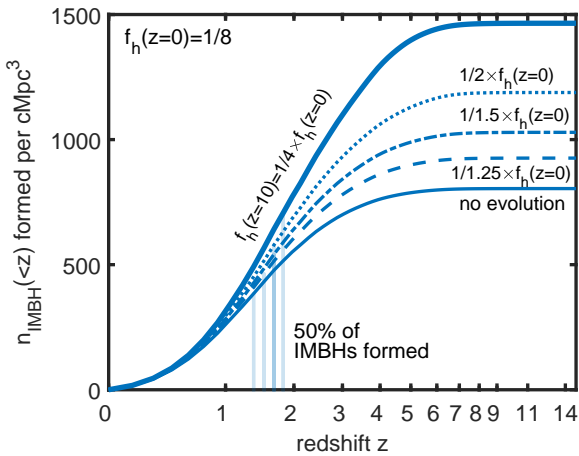


Figure 20. The total volumetric integrated number density of IMBHs $n_{\text{IMBH}}(< z)$ formed below redshift z . In all the shown models $f_h(z = 0) = 1/8$ while we display model variants with increasingly dense clusters forming at high redshifts. For a fixed cluster mass size relation (thin solid line), $n_{\text{IMBH}} \sim 804 \text{ Mpc}^{-3}$ IMBHs form below $z < 15$, while for the model with the densest early clusters we have $n_{\text{IMBH}} \sim 1465 \text{ Mpc}^{-3}$. Note that 50% of the IMBHs form at relatively low redshifts below $z \lesssim 1.5\text{--}2.0$.

relation $\log_{10}(\chi_{\text{IMBH}}(< 0.10 Z_{\odot})) = -4.17 \log_{10}(f_h) - 9.28$. For a Brown & Gnedin (2021) like cluster mass – size relation at birth ($f_h = 1$), IMBH formation is very rare with $\chi \lesssim 10^{-9}$ even at low metallicities.

6.3 Estimating the volumetric IMBH formation rate

We combine the IMBH formation efficiencies as a function of metallicity and the normalization of the cluster birth mass radius relations from Fig. 18 with a metallicity dependent SFRD model (Chruścińska et al. 2025; Chruścińska 2025) to obtain estimates for the cosmic IMBH formation rate density $\mathcal{R}_{\text{IMBH}}$. These estimates are displayed in Fig. 19. First, in the left panel, we assume that

the normalization of the cluster mass size relation does not depend on redshift. As the IMBH formation efficiency in our models is $\gtrsim 30$ times higher at metallicities below $\lesssim 0.10 Z_{\odot}$ compared to $Z = 1.0 Z_{\odot}$, the $\mathcal{R}_{\text{IMBH}}$ follows the rate density of low metallicity star formation, not the total SFRD. For the mass size relation normalization $f_h = 1/8$, $\mathcal{R}_{\text{IMBH}} \sim 2 \times 10^{-11} \text{ yr}^{-1} \text{ cMpc}^{-3}$ at $z = 15$, and $\mathcal{R}_{\text{IMBH}} \sim 9 \times 10^{-10} \text{ yr}^{-1} \text{ cMpc}^{-3}$ at $z = 10$. At later times the $\mathcal{R}_{\text{IMBH}}$ increases with the increasing low metallicity SFRD, the highest IMBH formation rate is $\mathcal{R}_{\text{IMBH}} \sim 1.3 \times 10^{-7} \text{ yr}^{-1} \text{ cMpc}^{-3}$, reached at $z \sim 2.3$, around the cosmic noon. The $\mathcal{R}_{\text{IMBH}}$ afterwards again decreases towards $\mathcal{R}_{\text{IMBH}} \sim 6 \times 10^{-9} \text{ yr}^{-1} \text{ cMpc}^{-3}$ at $z = 0$. As with the IMBH formation efficiency, the volumetric IMBH formation rates sensitively depend on the normalization of the star cluster mass size relation. The maximum $\mathcal{R}_{\text{IMBH}}$ follows an empirical relation of $\max(\mathcal{R}_{\text{IMBH}}) \sim -4.19 \log_{10}(f_h) - 10.64$. In all the models the $\mathcal{R}_{\text{IMBH}}$ peak around the cosmic noon is wide, with $\mathcal{R}_{\text{IMBH}} > 0.9 \max(\mathcal{R}_{\text{IMBH}})$ between $1.4 \lesssim z \lesssim 2.7$, and for $\mathcal{R}_{\text{IMBH}} > 0.5 \max(\mathcal{R}_{\text{IMBH}})$, $0.9 \lesssim z \lesssim 4.5$. We show in Appendix D that the $\mathcal{R}_{\text{IMBH}}$, its peak redshift and the width of the peak depend on the assumed model for the SFRD(Z). However, we note that the poorly constrained birth densities of the star clusters especially at high redshifts dominate the uncertainties in $\mathcal{R}_{\text{IMBH}}$.

We examine the effect of the evolving cluster mass radius relation normalization $f_h(z)$ on the $\mathcal{R}_{\text{IMBH}}$ in the right panel of Fig. 19. For all the displayed models $f_h(z = 0) = 1/8$, but we increase the high redshift cluster birth densities by allowing 1.25–4.0 times more compact clusters at $z = 10$ compared to $z = 0$. Increasingly dense high redshift cluster models increase the IMBH formation rate density by a factor of $\sim 2\text{--}3$ up to $\mathcal{R}_{\text{IMBH}} \sim 3 \times 10^{-7} \text{ yr}^{-1} \text{ cMpc}^{-3}$. The peak of the $\mathcal{R}_{\text{IMBH}}$ also shifts towards $z \sim 4$, and becomes narrower compared to the case of the non-evolving cluster mass size relation. In the models that allow more compact early star clusters, the $\mathcal{R}_{\text{IMBH}}$ and SFRD histories show increasingly distinct overall shapes, deviating from each other.

Finally, we show the total number of IMBHs formed below redshift z in a co-moving volume of space (n_{IMBH}) integrated over look-back time in Fig 20. For the cluster mass-size relation normal-

ization $f_h(z=0) = 1/8$ we have $804 \text{ cMpc}^{-3} \lesssim n_{\text{IMBH}} \lesssim 1465 \text{ cMpc}^{-3}$ IMBH formed below $z=15$, depending on the evolution of the star cluster mass radius relation at high redshifts. For less dense cluster models in the non-evolving case $\sim 51 \text{ cMpc}^{-3}$ IMBHs form below $z=15$ for $f_h=1/4$, and $\lesssim 2 \text{ cMpc}^{-3}$ for $f_h=1/2$.

6.4 Not all IMBHs form at early times?

Despite the large uncertainties in the volumetric IMBH formation rates mainly originating from the uncertain cluster birth densities, it is possible to draw a number of relatively robust conclusions from our models. IMBH formation can proceed in environments with a wide range of metallicities below $Z \lesssim 0.7 Z_\odot$. However, there is a characteristic metallicity below which the IMBH formation is the most abundant: most of the IMBHs form at metallicities below $0.10 Z_\odot$ – $0.2 Z_\odot$. At lower metallicities, less star formation is available even for the early dense models, and at higher metallicities the high wind mass loss rates strongly inhibit the IMBH formation. As briefly discussed in Appendix D, the metallicity dependence of the IMBH formation varies between models with different SFRD(Z) histories.

Second, we highlight that in the dense models that can form IMBHs, 50% of the IMBHs form below redshifts $z \lesssim 1.5$ – 2 . The exact redshift below which 50% of the IMBHs are produced somewhat depends on the assumed SFRD(Z), but is $z \lesssim 3$ for the SFRD histories we examined as shown in Appendix D. While the choice of SFRD(Z) and especially the normalization of the cluster mass size relation f_h strongly affect the volumetric rates of IMBH formation, the redshift below which 50% of IMBHs form is considerably less affected by the uncertainties. Our results indicate that if star clusters in the Universe are dense enough at birth to form IMBHs, the IMBH formation is not solely restricted to high redshifts, but approximately a half of them can be expected to form at redshifts below $z \lesssim 1.5$ – 3 . Still, this scenario might be potentially avoided if the star cluster birth densities at high redshifts are extremely high, and rapidly decrease below $z \lesssim 10$, or if high wind loss rates prevent IMBH formation in all but the lowest metallicity environments.

6.5 The IMBH mass function

We show the overall mass function of IMBHs formed over cosmic time in an average co-moving volume of space in Fig. 21. As before, the IMBH mass function sensitively depends on the normalization of the star cluster birth mass size relation. Overall, the shape of the mass function is not well described by a simple power law, but rather a Schechter like function with a power law shape at $M_\bullet \lesssim 1000 M_\odot$ followed by an exponential decline at high IMBH masses that is sharper than in the Schechter function. In addition, we study the effect of GW mergers between the formed IMBHs and stellar BHs on the IMBH mass function in < 10 Myr star clusters. As early GW mergers between IMBHs and stellar BHs seem to be common (Rantala et al. 2024, 2025), we merge each IMBH in the mass function with a $50 M_\odot$ stellar BH to see if the IMBH would be retained in its birth sub-cluster. For the merger procedure we assume relatively low spin magnitudes ($a_{\text{BH}} = 0.2$) motivated by the Geneva model (Belczynski et al. 2020) and random spin orientations. Consequently, the IMBH mass function below $M_\bullet \lesssim 200 M_\odot$ – $600 M_\odot$ is strongly suppressed by the GW recoil kicks as up to 80–90% of low mass IMBHs are removed from their host clusters. The large fraction of the removed IMBHs is due to the Schechter like shape of the IMBH mass function: most

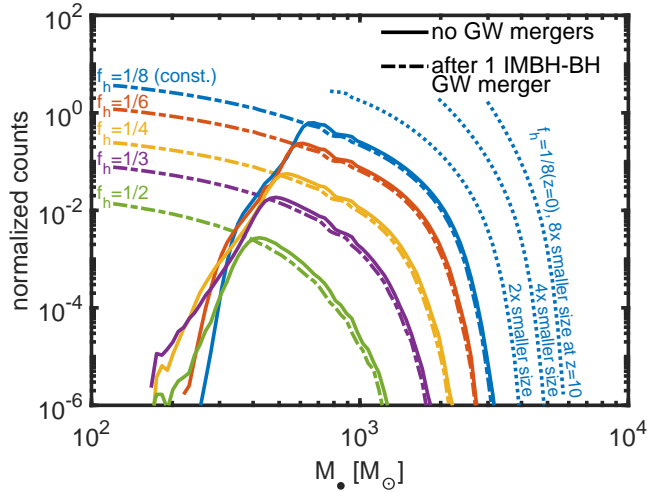


Figure 21. The cumulative IMBH mass function formed in an average volume of space. The IMBH mass function (solid lines) sensitively depends on the cluster mass radius relation normalization f_h . Without IMBH-BH GW kicks, the model variants follow a Schechter like function with a power law shape at $M_\bullet < 1000 M_\odot$ followed by a sharp exponential decline. Including GW kicks in the models (dot-dashed lines) efficiently suppresses the low mass end of the IMBH mass function below $M_\bullet \lesssim 200 M_\odot$ – $600 M_\odot$, the exact location of the turnaround depending on the cluster densities. Allowing the cluster birth mass radius relation to evolve to up to 8 times smaller clusters at $z=10$ (dotted lines) shifts the IMBH mass function to towards higher mass IMBHs up to $M_\bullet \sim 6000 M_\odot$ in the densest early models.

IMBHs have relatively low masses below $M_\bullet \lesssim 500 M_\odot$. The exact location of this turnaround point in the mass function depends on the competition between the increasing escape velocities in more dense and massive clusters, their more massive IMBHs, and larger kick velocity magnitudes for spinning massive BHs. Again, both the overall normalization and the high-mass extent of the IMBH mass function sensitively depend on the cluster birth radii and densities. For the case of the non-evolving cluster mass size relation (left panel of Fig. 21), the most massive IMBHs in dense clusters ($f_h = 1/8$) can reach $M_\bullet \gtrsim 3100 M_\odot$ while the typical IMBH mass is lower, of the order of $M_\bullet \sim 1000 M_\odot$. In lower density clusters ($f_h = 1/4$ and $1/2$) the maximum IMBH masses are $M_\bullet \sim 2200 M_\odot$ and $M_\bullet \sim 1400 M_\odot$, respectively. In the models with an evolving cluster mass size relation and denser high redshift clusters the IMBH mass distribution extends towards higher IMBH masses with the peak of the mass distribution remaining near $M_\bullet \sim 1000 M_\odot$. The densest early models reach $M_\bullet \sim 5500 M_\odot$ in IMBH mass. We emphasize that when IMBH-BH GW kicks are included, most of the IMBHs have masses around the turnaround point of the mass function, and more massive IMBHs are increasingly rare due to the shape of the mass function. For example, for $f_h = 1/8$, compared to $M_\bullet = 1000 M_\odot$ IMBHs, IMBHs with $M_\bullet = 2000 M_\odot$ are over 20 times more rare while $M_\bullet = 3000 M_\odot$ over 10^4 times less common.

We note that the IMBH mass functions of Fig. 21 are optimistic in a sense that additional GW mergers with stellar BHs and the resulting recoil kicks would remove further IMBHs from their host clusters, especially in the low mass end (e.g. Arca Sedda et al. 2023b). In addition, we have shown that IMBH-IMBH mergers are very common in hierarchically assembling clusters (Rantala & Naab 2025). The close to equal mass ratios of IMBHs (compared to IMBH-BH mergers) promote higher recoil kick velocities beyond $v_{\text{kick}} > 100 \text{ km s}^{-1}$ which are high enough to unbind the remnant

IMBHs from all but most massive star clusters. Based on Rantala et al. (2024) and Rantala et al. (2025) we estimate that up to 50% of formed IMBHs could be removed from their birth environments by such IMBH-IMBH mergers early in their evolution in clusters that form 2–5 IMBHs. In massive clusters of $M_{\text{cl}} \sim 10^7 M_{\odot}$, which could in principle form tens of IMBHs in their sub-clusters, IMBH-IMBH mergers are not guaranteed due to chaotic multi-body interactions (Partmann et al. 2024). Most of the mergers between the formed IMBHs are not massive enough to be detectable by LISA, but are promising targets for the next generation ground-based GW observatories such as the Einstein Telescope (Abac et al. 2025a; Lee et al. 2025). Nevertheless, only massive IMBHs ($M_{\bullet} \geq 10^4 M_{\odot}$) are guaranteed to be retained in their birth clusters (Arca Sedda et al. 2021), and detailed long term (1–10 Gyr) integrations would be needed to evaluate the fraction of lower mass IMBHs surviving in their host clusters until the present day.

6.6 The runaway seed channel and the number density of high redshift SMBHs

Provided that IMBHs can be retained in their birth environments, for our fiducial cluster birth mass size relation normalization $f_h = 1/8$, typical IMBHs formed at $z \sim 15$ would have enough time to reach masses of $M_{\bullet} \sim 10^5 M_{\odot}$ by $z = 10$ and $M_{\bullet} \gtrsim 5 \times 10^7 M_{\odot}$ by $z = 7$, assuming growth at the Eddington rate. In order to explain individual record-holding high redshift AGN such as the GN-z11 (Maiolino et al. 2024a) starting from IMBHs at $z \sim 15$, seed masses above $M_{\bullet} \gtrsim 10^4 M_{\odot}$ are required. As demonstrated in Rantala et al. (2025), early IMBH-IMBH mergers can provide a plausible channel to form such $M_{\bullet} \sim 10^4 M_{\odot}$ IMBHs through GW driven mergers of lower mass IMBHs. Assuming that each assembled star cluster in our model retains exactly one IMBH (see Rantala et al. 2024) and subsequent Eddington rate growth for the IMBH, we estimate the number density of $M_{\bullet} \gtrsim 10^7 M_{\odot}$ SMBHs at $z = 7$ to be $\sim 10^{-4} \text{ cMpc}^{-3}$, overall consistent with the number density of *JWST* little red dots (Greene et al. 2024; Kocevski et al. 2025; Kokorev et al. 2024). We emphasize that our estimate relies on several simplified assumptions, and should be regarded as an upper limit for the number density of high redshift SMBHs originating from runaway star cluster IMBH seeds. Still, it seems that runaway star cluster IMBH seeds could in principle grow into the observed high redshift AGN, especially the $z \sim 6$ –7.5 population (Inayoshi et al. 2020), and that the scenario does not result in severe under- or overproduction of massive black holes at high redshifts.

7 SUMMARY AND CONCLUSIONS

We have performed a large sample of direct N -body simulations using the BIFROST code including stellar evolution and post-Newtonian BH dynamics to explore the hierarchical assembly and the early evolution of massive star clusters. While the competition of stellar wind mass losses and stellar collisional growth has been previously studied (e.g. Mapelli 2016), we systematically examine the effect of initial star cluster masses ($10^4 M_{\odot} \lesssim M_{\text{cl}} \lesssim 10^6 M_{\odot}$), densities ($4 \times 10^3 M_{\odot} \text{pc}^{-2} \lesssim \Sigma_h \lesssim 4 \times 10^6 M_{\odot} \text{pc}^{-2}$) and metallicities ($0.01 Z_{\odot} \lesssim Z \lesssim 1.0 Z_{\odot}$) on the extremely massive star and IMBH formation through runaway stellar collisions in a set of more than $N_{\text{sim}} \geq 1440$ direct simulations. Our key findings can be summarized as follows.

Our simulation results demonstrate that the formation of IMBHs with masses in the range of $300 M_{\odot} \lesssim M_{\bullet} \lesssim 6000 M_{\odot}$

via runaway stellar collisions is plausible in massive, dense clusters at metallicities up to $Z \sim 0.2$ –0.3 Z_{\odot} . Below this critical threshold metallicity, the initial star cluster density, rather than the metallicity, determines the IMBH masses. At higher metallicities especially above $\gtrsim 0.5 Z_{\odot}$ the IMBH formation becomes increasingly improbable, and the masses of the IMBHs that form are systematically lower than at low metallicities because of the higher stellar wind mass loss rates. We find that for massive star clusters above $M_{\text{cl}} \gtrsim 10^4 M_{\odot}$ it is possible to formulate relatively simple empirical models that describes the maximum IMBH masses $M_{\bullet} = M_{\bullet}(\Sigma_h, Z)$ as a function of the metallicity and surface density of their host clusters. We provide two such models that can be both used within the (Σ_h, Z) parameter space of our simulations, and also be used at higher initial star cluster surface densities beyond $\Sigma_h \gtrsim 10^6 M_{\odot} \text{pc}^{-2}$.

We have performed the densest models of hierarchically assembling star clusters to date up to initial sub-cluster half mass surface densities of $\Sigma_h \sim 4 \times 10^6 M_{\odot} \text{pc}^{-2}$ including models at $Z = 0.01 Z_{\odot}$ and $Z = 0.10 Z_{\odot}$. Increasingly dense cluster models produce increasingly massive collisionally grown stars and IMBHs as well as result in high rates of mass loss from the stars. The substantial amount of wind and collisional mass loss up to $\sim 20000 M_{\odot}$ per extremely massive star may also contribute to the extreme abundance variations possible in the future generation stars with total stellar mass loss budgets up to ~ 5 –10% of the final assembled cluster mass in the densest models. At $Z = 0.10 Z_{\odot}$, the collisional ejecta losses become comparable to the total wind losses at $\Sigma_h \sim 3 \times 10^5 M_{\odot} \text{pc}^{-2}$ while at low metallicity ($Z = 0.01 Z_{\odot}$) the collisional losses always dominate. We find that the stellar population mass loss budget transforms from being VMS driven into being dominated by individual extremely massive (or even supermassive) stars at a threshold surface density of $\Sigma_h \sim 2$ – $4 \times 10^5 M_{\odot} \text{pc}^{-2}$. In the densest models, the central stellar densities up to $\rho_c \gtrsim 10^7 M_{\odot} \text{pc}^{-3}$ can support sustained IMBH TDE rates above $\Gamma_{\text{TDE}} \gtrsim 10^{-5} \text{ yr}^{-1}$ per cluster close to the regime in which runaway IMBH growth via TDEs becomes possible (Stone et al. 2017; Rizzuto et al. 2023). Our densest hierarchical models also result in the destruction of both supernova progenitors (up to ~ 26 –40%) and binary stars (up to $\gtrsim 50\%$) during the first $t = 7.5$ Myr of cluster evolution, potentially considerably affecting the stellar feedback budget of the stellar populations in extremely dense star clusters.

Despite the high stellar collision rates exceeding $\gtrsim 10^{-3} \text{ yr}^{-1}$, none of the collisionally grown stars reach a mass of $10000 M_{\odot}$ or above with our standard adopted wind prescription (Vink 2018) due to the high wind mass loss rates. The uncertainties in the modelling assumptions for the extremely massive and supermassive stars translate into large uncertainties in the final IMBH masses. We highlight the effect of wind model and rate uncertainties, the recipes for collisional mass loss and the radii of collisionally grown stars. We show that different but widely used models for extremely massive star wind rates (Humphreys & Davidson 1994; Vink et al. 2001; Belczynski et al. 2010 versus Vink 2018) result in final IMBH masses differing by a factor of ~ 4 . In our idealised comparison simulation with the wind rates resembling the rates adopted by Vergara et al. (2025a), we reach high stellar and IMBH masses exceeding $25000 M_{\odot}$. We emphasize that EMS stellar wind models are decisive in determining whether the runaway collisional channel can result in SMBHs seeds of $M_{\bullet} \gtrsim 10^4 M_{\odot}$ or above.

Finally, we provide an estimate of the cosmic volumetric formation rate of IMBHs ($\mathcal{R}_{\text{IMBH}}$) due to runaway stellar collisions in young, dense star clusters. Starting from the metallicity (iron abundance) dependent star formation rate density models of Chruścińska

et al. (2024, 2025), we build our model by assuming the fraction of stellar mass formed in clusters, the universal power-law -2 cluster mass function and the hierarchical assembly of the sub-clusters. Most importantly, we examine multiple different normalizations f_h of the initial cluster mass size relation which determines the birth radii and densities of the clusters. The assumption of the initial cluster densities proves to be the crucially important as the IMBH formation efficiency $\chi = \mathcal{R}_{\text{IMBH}}/\text{SFRD}$ and the volumetric IMBH formation rates $\mathcal{R}_{\text{IMBH}}$ sensitively depend on the cluster birth densities. In models with an intermediate SFRD(Z) and a fixed non-evolving cluster mass size relation normalization f_h , we have $\max(\mathcal{R}_{\text{IMBH}}) \sim 10^{-7} \text{ yr}^{-1} \text{cMpc}^{-3}$ for the standard initial cluster density assumption $f_h = 1/8$ from our earlier studies (Rantala et al. 2024; Rantala & Naab 2025; Rantala et al. 2025). The highest values for the $\mathcal{R}_{\text{IMBH}}$ are reached around a broad peak around $z \sim 1.4\text{--}2.7$ when the star formation at metallicities near $z \sim 0.10Z_\odot$ is the most abundant. At $z = 0$, we have $\mathcal{R}_{\text{IMBH}} \sim 6 \times 10^{-9} \text{ yr}^{-1}$ for the non-evolving $f_h = 1/8$. For increasingly large cluster birth radii (lower initial densities) the volumetric IMBH formation rates considerably decrease. In models in which we allow denser star clustered star formation at high redshifts, $\max(\mathcal{R}_{\text{IMBH}}) \sim 3 \times 10^{-7} \text{ yr}^{-1} \text{cMpc}^{-3}$, and the peak of the $\mathcal{R}_{\text{IMBH}}$ is narrower, and shifts towards $z \sim 4$. We also find that the $\mathcal{R}_{\text{IMBH}}$ depends on the assumed SFRD(Z) model we specifically assume by a factor up to an order of magnitude, our fiducial model resulting in somewhat higher IMBH formation rate densities than typical models. Still, the SFRD(Z) model uncertainty is sub-dominant to the cluster birth radius uncertainty.

We note that our simple $\mathcal{R}_{\text{IMBH}}$ model is based on the volume averaged SFRD and not individual evolving galaxies. Improved $\mathcal{R}_{\text{IMBH}}$ estimates and more thorough explorations of model uncertainties could be performed by including our models for IMBH masses $M_\bullet(\Sigma_h, Z)$ into detailed semi-analytic galaxy formation frameworks that include models for massive star clusters or cluster based SMBH seeding (e.g. L-Galaxies; Spinosa et al. 2023; Hoyer et al. 2025, CAT; Valiante et al. 2011; Trinca et al. 2022, Delphi; Dayal et al. 2019).

Despite the various model uncertainties, a number of conclusions can be drawn from our cosmic IMBH formation rate density models. First, our model estimates demonstrate that the runaway star cluster SMBH seed channel does not lead to considerable under- or overproduction of seed black holes, and is consistent with the *JWST* little red dot AGN number densities of $10^{-4} \text{ cMpc}^{-3}$ at $z \sim 7$. Second, if star cluster birth densities are high enough to form IMBHs, 50% of them form in our models at redshifts below $1.7 \lesssim z \lesssim 2.9$. In this emerging picture, the vast majority of IMBHs do not belong to the same population as the potential early runaway SMBH seeds that formed in the first star clusters at $z > 10\text{--}20$ and challenges the picture of any IMBHs found at low redshift being failed SMBH seeds from the $z > 10$ Universe. Instead, we highlight the importance of the continuing observational pursuit to uncover IMBHs in the GCs of the Milky Way and in the Local Group of galaxies for which the IMBH masses and the star cluster ages, and thus the IMBH formation redshifts, could be in principle relatively reliably determined.

For improved runaway collisional IMBH formation rate predictions more accurate information of the massive cluster birth radii and densities would be required. Unfortunately, well resolved birth radii of young (\lesssim a few Myr) still embedded clusters are challenging to obtain even in the local Universe. Interestingly, local young massive star clusters rarely reach as compact sizes and high mean stellar densities as high-redshift proto-GCs (e.g. Ryon et al. 2017; Levy et al. 2024). Moreover, the current high resolution cosmological

GC formation simulations still rely on gravitational softening, suppressing strong small-scale gravitational interactions, which would be essential to self-consistently model the initial formation phase of the clusters. Our results highlight the need for star-by-star resolution star cluster formation simulations at different metallicities including both hydrodynamics and non-softened stellar dynamics, preferentially in their galactic and cosmological environments for informed estimates of the initial cluster birth densities. We have recently taken the first steps towards such models in the galactic context (Lahén et al. 2025b,a) by including the accurate small-scale dynamics module KETJU (Rantala et al. 2017, 2020; Mannerkoski et al. 2023) into the star-by-star resolution hydrodynamical galaxy formation framework GRIFFIN (Lahén et al. 2020).

DATA AVAILABILITY STATEMENT

The data relevant to this article will be shared on reasonable request to the corresponding author.

ACKNOWLEDGMENTS

AR thanks Abbas Askar, Rainer Spurzem and Marcelo Vergara for useful discussions on N -body model comparisons, and Angela Adamo, Adélaïde Claeysens as well as Vasily Belokurov for motivating the plausible star cluster densities at low and high redshifts, as well as Daniel Schaefer and Miroslava Dessauges-Zavadsky for the encouraging discussion on the SMBH seed number densities. The numerical simulations were performed using facilities in Germany hosted by the Max Planck Computing and Data Facility (MPCDF) and the Leibniz Supercomputing Centre (LRZ) in Garching, and the JUWELS Booster of the Jülich supercomputing centre (GCS project 59949 frost-smbh-origins). TN acknowledges support from the Deutsche Forschungsgemeinschaft (DFG, German Research Foundation) under Germany's Excellence Strategy - EXC-2094 - 390783311 from the DFG Cluster of Excellence "ORIGINS". NL was supported by a Gliese Fellowship at the Zentrum für Astronomie, Universität Heidelberg, Germany. BR acknowledges support by the European Research Council via ERC Consolidator grant KETJU (no. 818930). The development of the SEVN code was enabled by M. Mapelli's ERC Consolidator grant DEMOBLACK by the European Research Council under contract no. 770017.

REFERENCES

- Aarseth S. J., 2003, Gravitational N-Body Simulations. Cambridge University Press
- Abac A., et al., 2025a, arXiv e-prints, p. arXiv:2503.12263
- Abac A. G., et al., 2025b, *ApJ*, 993, L25
- Abbott D. C., 1982, *ApJ*, 259, 282
- Abbott B. P., et al., 2017, *Phys. Rev. Lett.*, 118, 221101
- Abdurro'uf et al., 2025, arXiv e-prints, p. arXiv:2512.08054
- Adamo A., et al., 2020, *Space Sci. Rev.*, 216, 69
- Adamo A., et al., 2024, *Nature*, 632, 513
- Alexander T., Bar-Or B., 2017a, *Nature Astronomy*, 1, 0147
- Alexander T., Bar-Or B., 2017b, *Nature Astronomy*, 1, 0147
- Amaro-Seoane P., et al., 2012, *Classical and Quantum Gravity*, 29, 124016
- Angus C. R., et al., 2024, *ApJ*, 977, L41
- Arca Sedda M., Mastrobuono-Battisti A., 2019, arXiv e-prints, p. arXiv:1906.05864
- Arca Sedda M., Mapelli M., Spera M., Benacquista M., Giacobbo N., 2020, *ApJ*, 894, 133

Arca Sedda M., Amaro Seoane P., Chen X., 2021, [A&A](#), **652**, A54

Arca Sedda M., Mapelli M., Benacquista M., Spera M., 2023a, [MNRAS](#), **520**, 5259

Arca Sedda M., Kamlah A. W. H., Spurzem R., Rizzato F. P., Naab T., Giersz M., Berczik P., 2023b, [MNRAS](#), **526**, 429

Arca Sedda M., et al., 2024, [MNRAS](#), **528**, 5119

Banerjee S., Belczynski K., Fryer C. L., Berczik P., Hurley J. R., Spurzem R., Wang L., 2020, [A&A](#), **639**, A41

Barber J., Antonini F., 2025, [MNRAS](#), **538**, 639

Baumgardt H., 2017, [MNRAS](#), **464**, 2174

Baumgardt H., Klessen R. S., 2011, [MNRAS](#), **413**, 1810

Bekki K., Freeman K. C., 2003, [MNRAS](#), **346**, L11

Belczynski K., Banerjee S., 2020, [A&A](#), **640**, L20

Belczynski K., Bulik T., Fryer C. L., Ruiter A., Valsecchi F., Vink J. S., Hurley J. R., 2010, [ApJ](#), **714**, 1217

Belczynski K., et al., 2020, [A&A](#), **636**, A104

Belkus H., Van Bever J., Vanbeveren D., 2007, [ApJ](#), **659**, 1576

Belokurov V., Kravtsov A., 2022, [MNRAS](#), **514**, 689

Bernard Y., Moraux E., Price D. J., Motte F., Louvet F., Joncour I., 2025, [arXiv e-prints](#), p. [arXiv:2508.05296](#)

Binney J., Tremaine S., 2008, Galactic Dynamics: Second Edition. Princeton University Press, Princeton, NJ USA

Bradač M., et al., 2025, [arXiv e-prints](#), p. [arXiv:2509.20446](#)

Bressan A., Marigo P., Girardi L., Salasnich B., Dal Cero C., Rubele S., Nanni A., 2012, [MNRAS](#), **427**, 127

Bromm V., Ferrara A., Coppi P. S., Larson R. B., 2001, [MNRAS](#), **328**, 969

Brown G., Gnedin O. Y., 2021, [MNRAS](#), **508**, 5935

Bunker A. J., et al., 2023, [A&A](#), **677**, A88

Cameron A. J., Katz H., Rey M. P., Saxena A., 2023, [MNRAS](#), **523**, 3516

Cao L., Lu Y., Zhao Y., 2018, [MNRAS](#), **474**, 4997

Cappellari M., et al., 2013, [MNRAS](#), **432**, 1862

Castor J. I., Abbott D. C., Klein R. I., 1975, [ApJ](#), **195**, 157

Chandar R., Fall S. M., Whitmore B. C., Mulia A. J., 2017, [ApJ](#), **849**, 128

Charbonnel C., Schaefer D., Prantzos N., Ramírez-Galeano L., Fragos T., Kuruvanthodi A., Marques-Chaves R., Gieles M., 2023, [A&A](#), **673**, L7

Chatterjee S., Rodriguez C. L., Rasio F. A., 2017, [ApJ](#), **834**, 68

Chattopadhyay D., Hurley J., Stevenson S., Raidani A., 2022, [MNRAS](#), **513**, 4527

Chen Y., Bressan A., Girardi L., Marigo P., Kong X., Lanza A., 2015, [MNRAS](#), **452**, 1068

Chilingarian I. V., Katkov I. Y., Zolotukhin I. Y., Grishin K. A., Beletsky Y., Boutsia K., Osip D. J., 2018, [ApJ](#), **863**, 1

Chin S. A., 1997, [Physics Letters A](#), **226**, 344

Chin S. A., 2007, [arXiv e-prints](#), p. [arXiv:0704.3273](#)

Chin S. A., Chen C. R., 2005, [Celestial Mechanics and Dynamical Astronomy](#), **91**, 301

Chon S., Ono H., Omukai K., Schneider R., 2022, [MNRAS](#), **514**, 4639

Chruścińska M., 2025, Data accompanying the paper "Trading oxygen for iron II. Oxygen- versus iron-dependent cosmic star formation history" (Chruslinska et al. 2025), doi:10.5281/zenodo.18018783, <https://doi.org/10.5281/zenodo.18018783>

Chruścińska M., Nelemans G., 2019, [MNRAS](#), **488**, 5300

Chruścińska M., Nelemans G., Boco L., Lapi A., 2021, [MNRAS](#), **508**, 4994

Chruścińska M., Pakmor R., Matthee J., Matsuno T., 2024, [A&A](#), **686**, A186

Chruścińska M., Curti M., Pakmor R., De Cia A., Matthee J., Bhagwat A., Monty S., 2025, [arXiv e-prints](#), p. [arXiv:2511.15782](#)

Claeyssens A., Adamo A., Messa M., Dessauges-Zavadsky M., Richard J., Kramarenko I., Matthee J., Naidu R. P., 2025, [MNRAS](#), **537**, 2535

Cleveland W., Devlin S., 1988, [Journal of the American Statistical Association](#), **83**, 596

Colbert E. J. M., Mushotzky R. F., 1999, [ApJ](#), **519**, 89

Costa G., Bressan A., Mapelli M., Marigo P., Iorio G., Spera M., 2021, [MNRAS](#), **501**, 4514

Costa G., Ballone A., Mapelli M., Bressan A., 2022, [MNRAS](#), **516**, 1072

Costa G., et al., 2025, [A&A](#), **694**, A193

Crowther P. A., Schnurr O., Hirschi R., Yusof N., Parker R. J., Goodwin S. P., Kissim H. A., 2010, [MNRAS](#), **408**, 731

Curti M., Mannucci F., Cresci G., Maiolino R., 2020, [MNRAS](#), **491**, 944

Davidzon I., et al., 2017, [A&A](#), **605**, A70

Dayal P., Maiolino R., 2025, [arXiv e-prints](#), p. [arXiv:2506.08116](#)

Dayal P., Rossi E. M., Shiralilou B., Piana O., Choudhury T. R., Volonteri M., 2019, [MNRAS](#), **486**, 2336

Dehnen W., Hernandez D. M., 2017, [MNRAS](#), **465**, 1201

Della Croce A., Pascale R., Giunchi E., Nipoti C., Cignoni M., Dalessandro E., 2024, [A&A](#), **682**, A22

Denissenkov P. A., Hartwick F. D. A., 2014, [MNRAS](#), **437**, L21

Di Carlo U. N., Mapelli M., Bouffanais Y., Giacobbo N., Santoliquido F., Bressan A., Spera M., Haardt F., 2020a, [MNRAS](#), **497**, 1043

Di Carlo U. N., et al., 2020b, [MNRAS](#), **498**, 495

Dong R., Greene J. E., Ho L. C., 2012, [ApJ](#), **761**, 73

Dorozsmai A., Toonen S., 2024, [MNRAS](#), **530**, 3706

Ebihara S., Fujii M. S., Saitoh T. R., Hirai Y., Isobe Y., Nagae C., 2026, [arXiv e-prints](#), p. [arXiv:2601.04344](#)

Elmegreen B. G., Efremov Y. N., 1996, [ApJ](#), **466**, 802

Elmegreen B. G., Elmegreen D. M., 2005, [ApJ](#), **627**, 632

Elmegreen B. G., Elmegreen D. M., Fernandez M. X., Lemonias J. J., 2009, [ApJ](#), **692**, 12

Farrell S. A., Webb N. A., Barret D., Godet O., Rodrigues J. M., 2009, [Nature](#), **460**, 73

Fragione G., Loeb A., Kocsis B., Rasio F. A., 2022, [ApJ](#), **933**, 170

Fregeau J. M., Cheung P., Portegies Zwart S. F., Rasio F. A., 2004, [MNRAS](#), **352**, 1

Freitag M., Rasio F. A., Baumgardt H., 2006, [MNRAS](#), **368**, 121

Fryer C. L., Kalogera V., 2001, [ApJ](#), **554**, 548

Fryer C. L., Belczynski K., Wiktorowicz G., Dominik M., Kalogera V., Holz D. E., 2012, [ApJ](#), **749**, 91

Fujii M. S., Portegies Zwart S., 2013, [MNRAS](#), **430**, 1018

Fujii M. S., Wang L., Tanikawa A., Hirai Y., Saitoh T. R., 2024, [Science](#), **384**, 1488

Fujimoto S., et al., 2024, [arXiv e-prints](#), p. [arXiv:2402.18543](#)

Gaburov E., Gualandris A., Portegies Zwart S., 2008, [MNRAS](#), **384**, 376

Garmany C. D., Conti P. S., 1985, [ApJ](#), **293**, 407

Gebhardt K., Rich R. M., Ho L. C., 2002, [ApJ](#), **578**, L41

Genzel R., et al., 2008, [ApJ](#), **687**, 59

Genzel R., et al., 2011, [ApJ](#), **733**, 101

Giacobbo N., Mapelli M., 2018, [MNRAS](#), **480**, 2011

Giacobbo N., Mapelli M., Spera M., 2018, [MNRAS](#), **474**, 2959

Gieles M., et al., 2018, [MNRAS](#), **478**, 2461

Gieles M., Padoan P., Charbonnel C., Vink J. S., Ramírez-Galeano L., 2025, [MNRAS](#), **544**, 483

Glebbeek E., Pols O. R., 2008, [A&A](#), **488**, 1017

Glebbeek E., Gaburov E., de Mink S. E., Pols O. R., Portegies Zwart S. F., 2009, [A&A](#), **497**, 255

Glebbeek E., Gaburov E., Portegies Zwart S., Pols O. R., 2013, [MNRAS](#), **434**, 3497

González Prieto E., Kremer K., Fragione G., Martinez M. A. S., Weatherford N. C., Zevin M., Rasio F. A., 2022, [ApJ](#), **940**, 131

González Prieto E., Weatherford N. C., Fragione G., Kremer K., Rasio F. A., 2024, [ApJ](#), **969**, 29

Goswami S., Umbreit S., Bierbaum M., Rasio F. A., 2012, [ApJ](#), **752**, 43

Gratton R., Bragaglia A., Carretta E., D'Orazi V., Lucatello S., Sollima A., 2019, [A&ARv](#), **27**, 8

Greene J. E., Ho L. C., 2007, [ApJ](#), **656**, 84

Greene J. E., Strader J., Ho L. C., 2020, [ARA&A](#), **58**, 257

Greene J. E., et al., 2024, [ApJ](#), **964**, 39

Gürkan M. A., Freitag M., Rasio F. A., 2004, [ApJ](#), **604**, 632

Häberle M., et al., 2024, [Nature](#), **631**, 285

Haemmerlé L., Woods T. E., Klessen R. S., Heger A., Whalen D. J., 2018, [MNRAS](#), **474**, 2757

Haster C.-J., Wang Z., Berry C. P. L., Stevenson S., Veitch J., Mandel I., 2016, [MNRAS](#), **457**, 4499

Hénon M. H., 1971, [Ap&SS](#), **14**, 151

Hopkins A. M., Beacom J. F., 2006, [ApJ](#), **651**, 142

Hosokawa T., Omukai K., Yorke H. W., 2012, [ApJ](#), **756**, 93

Hoyer N., et al., 2025, [arXiv e-prints](#), p. [arXiv:2504.12079](#)

Humphreys R. M., Davidson K., 1994, [PASP](#), **106**, 1025

Hurley J. R., Pols O. R., Tout C. A., 2000, *MNRAS*, **315**, 543
 Hurley J. R., Tout C. A., Pols O. R., 2002, *MNRAS*, **329**, 897
 Ibata R., et al., 2009, *ApJ*, **699**, L169
 Inayoshi K., Visbal E., Haiman Z., 2020, *ARA&A*, **58**, 27
 Iorio G., et al., 2023, *MNRAS*, **524**, 426
 Isobe Y., et al., 2023, *ApJ*, **959**, 100
 Isobe Y., et al., 2025, *arXiv e-prints*, p. [arXiv:2502.12091](https://arxiv.org/abs/2502.12091)
 Jalali B., Baumgardt H., Kissler-Patig M., Gebhardt K., Noyola E., Lützendorf N., de Zeeuw P. T., 2012, *A&A*, **538**, A19
 Ji X., et al., 2024, *MNRAS*, **535**, 881
 Ji X., Belokurov V., Maiolino R., Monty S., Isobe Y., Kravtsov A., Mc-Clymont W., Übler H., 2025, *arXiv e-prints*, p. [arXiv:2505.12505](https://arxiv.org/abs/2505.12505)
 Juodžbalis I., et al., 2024, *Nature*, **636**, 594
 Juodžbalis I., et al., 2025, *arXiv e-prints*, p. [arXiv:2508.21748](https://arxiv.org/abs/2508.21748)
 Kaaret P., Prestwich A. H., Zezas A., Murray S. S., Kim D. W., Kilgard R. E., Schlegel E. M., Ward M. J., 2001, *MNRAS*, **321**, L29
 Kamann S., et al., 2016, *A&A*, **588**, A149
 Kamlah A. W. H., et al., 2022, *MNRAS*, **516**, 3266
 Kim M., López K. M., Jonker P. G., Ho L. C., Im M., 2020, *MNRAS*, **493**, L76
 Kippenhahn R., Weigert A., Weiss A., 2013, *Stellar Structure and Evolution*. Springer Berlin Heidelberg, doi:10.1007/978-3-642-30304-3
 Kocevski D. D., et al., 2025, *ApJ*, **986**, 126
 Kochanek C. S., 1992, *ApJ*, **385**, 604
 Kokorev V., et al., 2024, *ApJ*, **968**, 38
 Kremer K., Lu W., Rodriguez C. L., Lachat M., Rasio F. A., 2019, *ApJ*, **881**, 75
 Kremer K., et al., 2020, *ApJ*, **903**, 45
 Kroupa P., 2001, *MNRAS*, **322**, 231
 Krumholz M. R., McKee C. F., Bland-Hawthorn J., 2019, *ARA&A*, **57**, 227
 Kuruvanthodi A., Schaefer D., Messa M., Adamo A., Usher C., Charbonnel C., Marques-Chaves R., 2023, *A&A*, **674**, A140
 Lahén N., Naab T., Johansson P. H., Elmegreen B., Hu C.-Y., Walch S., Steinwandel U. P., Moster B. P., 2020, *ApJ*, **891**, 2
 Lahén N., Naab T., Szécsi D., 2024, *MNRAS*, **530**, 645
 Lahén N., Naab T., Rantala A., Partmann C., 2025a, *arXiv e-prints*, p. [arXiv:2504.18620](https://arxiv.org/abs/2504.18620)
 Lahén N., Rantala A., Naab T., Partmann C., Johansson P. H., Hislop J. M., 2025b, *MNRAS*, **538**, 2129
 Lanzoni B., et al., 2013, *ApJ*, **769**, 107
 Lee Y. W., Joo J. M., Sohn Y. J., Rey S. C., Lee H. C., Walker A. R., 1999, *Nature*, **402**, 55
 Lee S., Lee H. M., Kim J.-h., Spurzem R., Hong J., Chung E., 2025, *ApJ*, **988**, 15
 Leonard P. J. T., 1989, *AJ*, **98**, 217
 Levy R. C., et al., 2024, *ApJ*, **973**, L55
 Liu S., Wang L., Hu Y.-M., Tanikawa A., Trani A. A., 2024, *MNRAS*, **533**, 2262
 Lombardi Jr. J. C., Warren J. S., Rasio F. A., Sills A., Warren A. R., 2002, *ApJ*, **568**, 939
 Lützendorf N., Kissler-Patig M., Noyola E., Jalali B., de Zeeuw P. T., Gebhardt K., Baumgardt H., 2011, *A&A*, **533**, A36
 Mackey A. D., Gilmore G. F., 2003, *MNRAS*, **338**, 85
 Madau P., Dickinson M., 2014, *ARA&A*, **52**, 415
 Madau P., Rees M. J., 2001, *ApJ*, **551**, L27
 Maiolino R., et al., 2024a, *Nature*, **627**, 59
 Maiolino R., et al., 2024b, *A&A*, **691**, A145
 Maiolino R., et al., 2025, *arXiv e-prints*, p. [arXiv:2505.22567](https://arxiv.org/abs/2505.22567)
 Mannerkoski M., Rawlings A., Johansson P. H., Naab T., Rantala A., Springel V., Irodotou D., Liao S., 2023, *MNRAS*, **524**, 4062
 Mapelli M., 2016, *MNRAS*, **459**, 3432
 Mapelli M., Bressan A., 2013, *MNRAS*, **430**, 3120
 Mapelli M., Zampieri L., Ripamonti E., Bressan A., 2013, *MNRAS*, **429**, 2298
 Mapelli M., Giacobbo N., Ripamonti E., Spera M., 2017, *MNRAS*, **472**, 2422
 Mapelli M., Spera M., Montanari E., Limongi M., Chieffi A., Giacobbo N., Bressan A., Bouffanais Y., 2020, *ApJ*, **888**, 76
 Marks M., Kroupa P., 2012, *A&A*, **543**, A8
 Marks M., Kroupa P., Dabringhausen J., Pawłowski M. S., 2012, *MNRAS*, **422**, 2246
 Marques-Chaves R., et al., 2024, *A&A*, **681**, A30
 Matsumoto H., Tsuru T. G., Koyama K., Awaki H., Canizares C. R., Kawai N., Matsushita S., Kawabe R., 2001, *ApJ*, **547**, L25
 Mazzolo G., et al., 2014, *Phys. Rev. D*, **90**, 063002
 McLaughlin D. E., van der Marel R. P., 2005, *ApJS*, **161**, 304
 Mehta A. K., Buonanno A., Gair J., Miller M. C., Farag E., deBoer R. J., Wiescher M., Timmes F. X., 2022, *ApJ*, **924**, 39
 Messa M., Dessauges-Zavadsky M., Adamo A., Richard J., Claeysens A., 2024, *MNRAS*, **529**, 2162
 Mezcua M., 2017, *International Journal of Modern Physics D*, **26**, 1730021
 Mezcua M., Roberts T. P., Sutton A. D., Lobanov A. P., 2013, *MNRAS*, **436**, 3128
 Mezcua M., Roberts T. P., Lobanov A. P., Sutton A. D., 2015, *MNRAS*, **448**, 1893
 Mezcua M., Civano F., Marchesi S., Suh H., Fabbiano G., Volonteri M., 2018, *MNRAS*, **478**, 2576
 Miller M. C., Hamilton D. P., 2002, *MNRAS*, **330**, 232
 Moe M., Di Stefano R., 2017, *ApJS*, **230**, 15
 Moster B. P., Naab T., White S. D. M., 2018, *MNRAS*, **477**, 1822
 Mowla L., et al., 2024, *Nature*, **636**, 332
 Muijres L., Vink J. S., de Koter A., Hirschi R., Langer N., Yoon S.-C., 2012, *A&A*, **546**, A42
 Naab T., Johansson P. H., Ostriker J. P., 2009, *ApJ*, **699**, L178
 Naidu R. P., et al., 2025, *arXiv e-prints*, p. [arXiv:2505.11263](https://arxiv.org/abs/2505.11263)
 Nandal D., Chon S., 2025, *arXiv e-prints*, p. [arXiv:2511.08516](https://arxiv.org/abs/2511.08516)
 Navarro-Carrera R., Rinaldi P., Caputi K. I., Iani E., Kokorev V., van Mierlo S. E., 2024, *ApJ*, **961**, 207
 Nguyen C. T., et al., 2022, *A&A*, **665**, A126
 Nieuwenhuijzen H., de Jager C., 1990, *A&A*, **231**, 134
 Noyola E., Gebhardt K., Kissler-Patig M., Lützendorf N., Jalali B., de Zeeuw P. T., Baumgardt H., 2010, *ApJ*, **719**, L60
 Offner S. S. R., Moe M., Kratter K. M., Sadavoy S. I., Jensen E. L. N., Tobin J. J., 2023, in Inutsuka S., Aikawa Y., Muto T., Tomida K., Tamura M., eds, *Astronomical Society of the Pacific Conference Series* Vol. 534, *Protostars and Planets VII*. p. 275 ([arXiv:2203.10066](https://arxiv.org/abs/2203.10066)), doi:10.48550/arXiv.2203.10066
 Omelyan I. P., 2006, *Phys. Rev. E*, **74**, 036703
 Paiella L., Arca Sedda M., Mestichelli B., Ugolini C., 2025, *arXiv e-prints*, p. [arXiv:2511.00200](https://arxiv.org/abs/2511.00200)
 Pakmor R., et al., 2022, *MNRAS*, **512**, 3602
 Partmann C., Naab T., Rantala A., Genina A., Mannerkoski M., Johansson P. H., 2024, *MNRAS*, **532**, 4681
 Partmann C., Naab T., Lahén N., Rantala A., Hirschmann M., Hislop J. M., Petersson J., Johansson P. H., 2025, *MNRAS*, **537**, 956
 Pasham D. R., Strohmayer T. E., Mushotzky R. F., 2014, *Nature*, **513**, 74
 Patruno A., Portegies Zwart S., Dewi J., Hopman C., 2006, *MNRAS*, **370**, L6
 Pauldrach A. W. A., Vanbeveren D., Hoffmann T. L., 2012, *A&A*, **538**, A75
 Pechetti R., et al., 2022, *ApJ*, **924**, 48
 Petersson J., et al., 2025, *arXiv e-prints*, p. [arXiv:2504.08035](https://arxiv.org/abs/2504.08035)
 Plummer H. C., 1911, *MNRAS*, **71**, 460
 Popesso P., et al., 2023, *MNRAS*, **519**, 1526
 Portegies Zwart S. F., Makino J., McMillan S. L. W., Hut P., 1999, *A&A*, **348**, 117
 Portegies Zwart S. F., Baumgardt H., Hut P., Makino J., McMillan S. L. W., 2004, *Nature*, **428**, 724
 Portegies Zwart S. F., McMillan S. L. W., Gieles M., 2010, *ARA&A*, **48**, 431
 Puls J., Vink J. S., Najarro F., 2008, *A&ARv*, **16**, 209
 Ramírez-Galeano L., Charbonnel C., Fragos T., Tazakkati Z., Roman-Garza J., Gieles M., 2025, *A&A*, **699**, A223
 Rantala A., Naab T., 2025, *arXiv e-prints*, p. [arXiv:2503.21879](https://arxiv.org/abs/2503.21879)
 Rantala A., Pihajoki P., Johansson P. H., Naab T., Lahén N., Sawala T., 2017, *ApJ*, **840**, 53

Rantala A., Pihajoki P., Mannerkoski M., Johansson P. H., Naab T., 2020, *MNRAS*, **492**, 4131

Rantala A., Naab T., Springel V., 2021, *MNRAS*, **502**, 5546

Rantala A., Naab T., Rizzato F. P., Mannerkoski M., Partmann C., Lautenschütz K., 2023, *MNRAS*, **522**, 5180

Rantala A., Naab T., Lahén N., 2024, *MNRAS*, **531**, 3770

Rantala A., Lahén N., Naab T., Escobar G. J., Iorio G., 2025, *MNRAS*, **543**, 2130

Rastello S., Iorio G., Gieles M., Wang L., 2025, *arXiv e-prints*, p. arXiv:2509.07067

Reali L., Cotesta R., Antonelli A., Kritoš K., Strokov V., Berti E., 2024, *Phys. Rev. D*, **110**, 103002

Rees M. J., 1984, *ARA&A*, **22**, 471

Regan J. A., Visbal E., Wise J. H., Haiman Z., Johansson P. H., Bryan G. L., 2017, *Nature Astronomy*, **1**, 0075

Reines A. E., 2022, *Nature Astronomy*, **6**, 26

Reinozo B., Schleicher D. R. G., Fellhauer M., Klessen R. S., Boekholt T. C. N., 2018, *A&A*, **614**, A14

Reinozo B., Klessen R. S., Schleicher D., Glover S. C. O., Solar P., 2023, *MNRAS*, **521**, 3553

Rinaldi S., Del Pozzo W., Mapelli M., Lorenzo-Medina A., Dent T., 2024, *A&A*, **684**, A204

Rizzato F. P., et al., 2021, *MNRAS*, **501**, 5257

Rizzato F. P., Naab T., Rantala A., Johansson P. H., Ostriker J. P., Stone N. C., Liao S., Irodotou D., 2023, *MNRAS*, **521**, 2930

Ryon J. E., et al., 2017, *ApJ*, **841**, 92

Sabahhit G. N., Vink J. S., Sander A. A. C., Higgins E. R., 2023, *MNRAS*, **524**, 1529

Santoliquido F., Mapelli M., Bouffanais Y., Giacobbo N., Di Carlo U. N., Rastello S., Artale M. C., Ballone A., 2020, *ApJ*, **898**, 152

Santoliquido F., Mapelli M., Giacobbo N., Bouffanais Y., Artale M. C., 2021, *MNRAS*, **502**, 4877

Schaerer D., Marques-Chaves R., Xiao M., Korber D., 2024, *A&A*, **687**, L11

Schaerer D., Marques-Chaves R., Atek H., Prantzos N., Charbonnel C., Talia M., Morel I., Dessauges-Zavadsky M., 2025, *arXiv e-prints*, p. arXiv:2512.16549

Schneider R., Ferrara A., Natarajan P., Omukai K., 2002, *ApJ*, **571**, 30

Scholtz J., et al., 2024, *A&A*, **687**, A283

Schulze S., et al., 2024, *A&A*, **683**, A223

Shepherd K. G., et al., 2025, *A&A*, **701**, A126

Shin E.-j., Sijacki D., Smith M. C., Bourne M. A., Koudmani S., 2025, *arXiv e-prints*, p. arXiv:2504.18384

Sicilia A., et al., 2022, *ApJ*, **924**, 56

Simonato F., Tornamenti S., Mapelli M., Iorio G., Boco L., De Domenico-Langer F., Sgalletta C., 2025, *A&A*, **703**, A215

Soltan A., 1982, *MNRAS*, **200**, 115

Souvatzis L., Rantala A., Naab T., 2025, *MNRAS*, **539**, 45

Spera M., Mapelli M., 2017, *MNRAS*, **470**, 4739

Spera M., Mapelli M., Bressan A., 2015, *MNRAS*, **451**, 4086

Spinoso D., Bonoli S., Valiante R., Schneider R., Izquierdo-Villalba D., 2023, *MNRAS*, **518**, 4672

Spurzem R., Kamlah A., 2023, *Living Reviews in Computational Astrophysics*, **9**, 3

Stefanom M., Bouwens R. J., Labbé I., Illingworth G. D., Gonzalez V., Oesch P. A., 2021, *ApJ*, **922**, 29

Stone N. C., Küpper A. H. W., Ostriker J. P., 2017, *MNRAS*, **467**, 4180

Strohmayer T. E., Mushotzky R. F., 2003, *ApJ*, **586**, L61

Tanikawa A., Susa H., Yoshida T., Trani A. A., Kinugawa T., 2021, *ApJ*, **910**, 30

Tanikawa A., Yoshida T., Kinugawa T., Trani A. A., Hosokawa T., Susa H., Omukai K., 2022, *ApJ*, **926**, 83

Tassis K., Gnedin N. Y., Kravtsov A. V., 2012, *ApJ*, **745**, 68

Tornamenti S., Mapelli M., Boco L., Simonato F., Iorio G., Korb E., 2025, *arXiv e-prints*, p. arXiv:2510.12465

Trani A. A., Mapelli M., Bressan A., 2014, *MNRAS*, **445**, 1967

Trinca A., Schneider R., Valiante R., Graziani L., Zappacosta L., Shankar F., 2022, *MNRAS*, **511**, 616

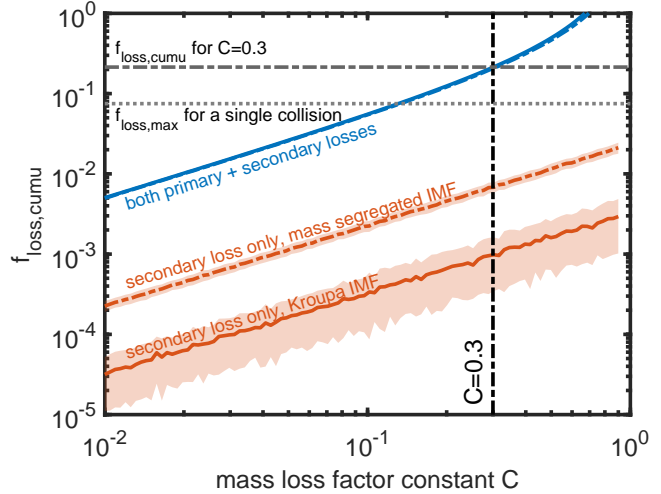


Figure A1. The cumulative mass loss fraction $f_{\text{loss,cumu}}$ as a function of the mass loss factor constant C of Eq. (2). When including mass loss from both the primary and secondary colliding stars, the cumulative fractional mass loss in a collision cascade can be higher compared to the maximum mass loss fraction in a single collision.

APPENDIX A: THE CUMULATIVE MASS LOSS IN MULTIPLE STELLAR COLLISIONS

As an example of cumulative mass loss in a large number of stellar collisions, we consider an extremely massive star with $m_{1,\text{init}} = 1000 M_{\odot}$ doubling its mass to reach $m_{1,\text{final}} = 2000 M_{\odot}$ via collisional mass growth. In the collisional mass loss model adopted for this study, each collision with a secondary star with a mass of m_2 leads to a mass loss of $m_{\text{loss}} = f_{\text{loss}}(m_1 + m_2)$. Following Eq. (2) $f_{\text{loss}} = Cq/(1+q)^2$ with a fiducial free parameter value of $C = 0.3$. We evaluate the total mass loss $m_{\text{loss,tot}} = \sum_i f_{\text{loss},i}(m_{1,i} + m_{2,i})$ during a series of collisions doubling the mass of $m_{1,\text{init}}$ and finally evaluate $f_{\text{loss,cumu}} = m_{\text{loss,tot}}/m_{1,\text{final}}$. We examine two different mass functions for the secondary stars: the Kroupa (2001) IMF ($0.08 M_{\odot} \leq m_{\star} \leq 150 M_{\odot}$) and one produced by mass segregation in which massive stars beyond $\gtrsim 5 M_{\odot}$ are over-represented (see e.g. figure 11 of Rantala et al. 2024). For the recipe including mass loss from both of the colliding stars (primary and secondary), the cumulative mass loss factor $f_{\text{loss,cumu}}$ is almost independent of the mass function of the secondary stars m_2 . This is because most of the ejected mass originates from the primary star. We show the $f_{\text{loss,cumu}}$ as a function of the constant C of the model in Fig. A1. As expected, increasing the value of C increases $f_{\text{loss,cumu}}$. For the fiducial value of $C = 0.3$, the cumulative mass loss fraction $f_{\text{loss,cumu}} \sim 0.214$, approximately ~ 2.85 times the maximum mass loss fraction $f_{\text{loss,max}} = 0.075$ in a single equal-mass collision. Compared to a collision with $q = 150 M_{\odot}/1000 M_{\odot}$, $f_{\text{loss,cumu}}$ is 6.29 times larger. Overall, the cumulative mass loss fractions increase with increasing $m_{1,\text{final}}/m_{1,\text{init}}$.

For N -body simulation models that only include mass loss from the secondary star the situation is different. In Fig. A1 we show that in the case of secondary star losses only the cumulative mass loss fraction depends on the mass function of the colliding stars in the absence of mass loss from the primary. The on average more massive stars from the mass segregated IMF lead to larger mass loss compared to the standard Kroupa IMF. Overall, models with primary star mass loss lead to more efficient collisional mass loss by 1–2 orders of magnitude depending on the mass function of the colliding stars. For $C = 0.3$, $f_{\text{loss,cumu}} \sim 10^{-3}$ for Kroupa IMF and $\sim 7 \times 10^{-3}$ for the mass segregated mass function.

APPENDIX B: MASSIVE STAR WIND LOSS RATE UNCERTAINTIES

In order to estimate how sensitive the IMBH masses in our simulations are to the stellar wind rate uncertainties, we perform 60 additional isolated star cluster simulations in which we artificially boost or weaken the winds of $> 600 M_{\odot}$ stars. The additional models are all based on the isolated setup I3D5Z5 with a cluster mass of $M_{\text{cl}} = 1.5 \times 10^5 M_{\odot}$, half mass surface density $\Sigma_{\text{h}} = 2.9 \times 10^5 M_{\odot} \text{ pc}^{-2}$ and metallicity of $Z = 0.10 Z_{\odot}$. In the models we multiply the Vink (2018) wind mass loss rate by a boost factor f_{wind} in the range of $0.125 \leq f_{\text{wind}} \leq 8.0$. The final IMBH masses in the simulations are shown in Fig. B1. The dependence of the mean IMBH masses for a given f_{wind} follows the empirical relation of

$$\log_{10}(M_{\bullet,\text{mean}}) = (-0.12 \pm 0.01) \times \log_{10}(f_{\text{wind}}) + (3.07 \pm 0.01) \quad (\text{B1})$$

while for the maximum IMBH masses we have

$$\log_{10}(M_{\bullet,\text{max}}) = (-0.08 \pm 0.02) \times \log_{10}(f_{\text{wind}}) + (3.18 \pm 0.01). \quad (\text{B2})$$

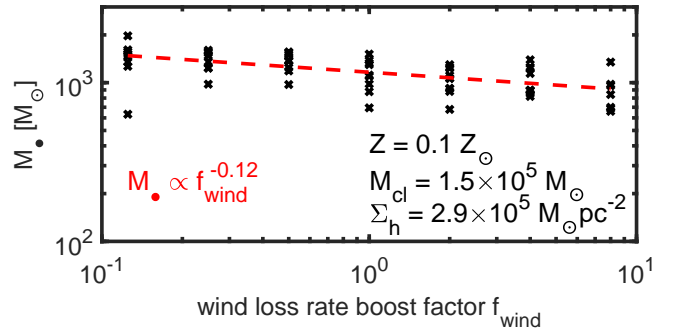


Figure B1. The effect of weakened or boosted winds on the maximum final IMBH masses in the isolated models. In the simulations the wild mass loss rate of Vink (2018) multiplied by the boost factor f_{wind} . For star clusters with intermediate mass ($M_{\text{cl}} = 1.5 \times 10^5 M_{\odot}$) and density ($\Sigma_{\text{h}} = 2.9 \times 10^5 M_{\odot} \text{ pc}^{-2}$) the final IMBH masses depend on the boost factor relatively weakly as $M_{\bullet} \propto f_{\text{wind}}^{-0.12}$.

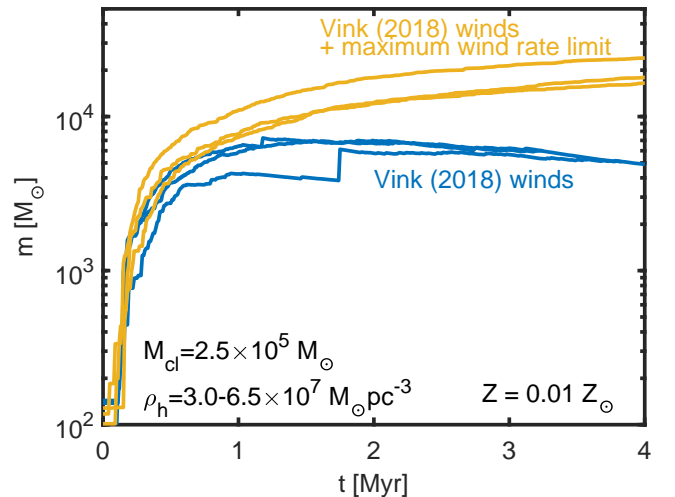


Figure C1. The effect of assuming a maximum wind loss rate limit on the collisional stellar growth histories in extremely dense star clusters. With the fiducial Vink (2018) winds the collisional runaway mass growth is quenched at $\sim 7000 M_{\odot}$ even at $Z = 0.01 Z_{\odot}$, including the maximum wind loss rate of $\text{max}(\dot{m}_{\text{wind}}) = 1.5 \times 10^{-4} M_{\odot} \text{ yr}^{-1}$ leads to monotonic growth into the SMS regime beyond $25000 M_{\odot}$.

Both the mean and maximum IMBH masses depend on the wind boost factor relatively weakly, at least for the models I3D5Z5.

APPENDIX C: THE EFFECT OF THE MAXIMUM WIND RATE LIMIT

We perform three additional isolated simulations of the extremely dense central sub-clusters of the models HD9Z1 to study the effect of a maximum wind mass loss rate limit on the maximum masses of the collisionally grown stars. While our models based on [Vink \(2018\)](#) do not include such an upper limit for the wind loss rates, recent *N*-body studies such as [Vergara et al. \(2025a,b\)](#) feature such a limit in their models reaching collisional stellar masses of $50000 M_{\odot}$. In Fig. 11 we showed using simulation post-processing that such a maximum wind rate limit allows for monotonic collisional stellar growth well into the SMS regime ($\gtrsim 20000$) while without the limit the maximum stellar masses plateau at $\sim 7000 M_{\odot}$ for $Z = 0.01 Z_{\odot}$. We proceed to test this scenario in a direct simulation instead of post-processing only. Following [Vergara et al. \(2025a\)](#), we set $\max(\dot{m}_{\text{wind}}) = 1.5 \times 10^{-4} M_{\odot} \text{yr}^{-1}$ in the additional test simulations. The mass growth histories of three most massive stars in the models, with and without the maximum wind rate limit, are displayed in Fig. C1. In the wind limited models the collisional mass growth proceeds well into the SMS regime, just as in the post-processed models, the most massive SMS reaching $25000 M_{\odot}$ during the first $t = 4$ Myr of its life. We do not reach the $50000 M_{\odot}$ star of [Vergara et al. \(2025a\)](#) even in out wind rate limited models, which we attribute to the smaller EMS and SMS radii in late stellar evolutionary stages, and the lower host star cluster mass we have.

APPENDIX D: THE EFFECT OF SFRD(Z) MODEL ASSUMPTIONS AND UNCERTAINTIES

We briefly examine the effect of the uncertainties and modelling assumptions of the metallicity dependent SFRD on the volumetric IMBH formation rates. Major uncertainties at high redshifts arise from the evolution of the slope of the galaxy stellar mass function. While the evolution of the GSMF slope is uncertain, there is a consensus that it steepens towards higher redshifts ([Davidzon et al. 2017; Stefanon et al. 2021; Navarro-Carrera et al. 2024; Weibel et al. 2024](#)), implying a progressively larger contribution from low mass galaxies to the SFRD at earlier cosmic times. If the low-mass slope is allowed to steepen with redshift and low mass galaxies down to $M_{\star} = 10^6 M_{\odot}$ are taken into account in the SFRD modelling, then the decline of the star formation history at $z > 2-3$ is much more gradual than in the widely used estimates (e.g. [Madau & Dickinson 2014](#); see section 5 in [Chrušlińska et al. 2025](#) for the discussion). Depending on the SFR of galaxies below $M_{\star} = 10^8 M_{\odot}$, the SFRD either follows a plateau like feature or steady decline.

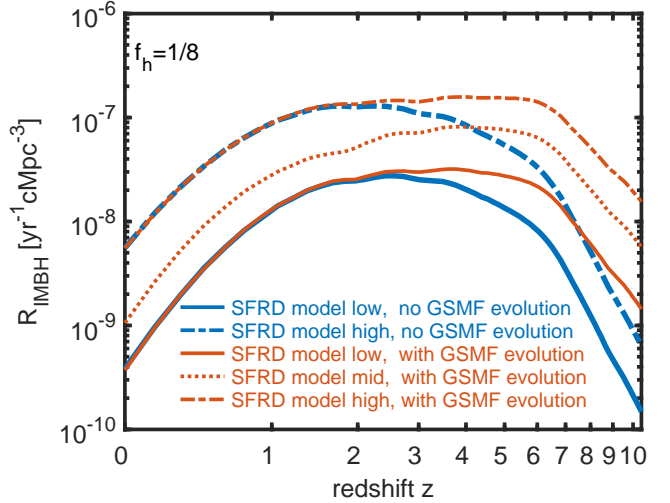


Figure D1. The effect of the assumed SFRD on the cosmic IMBH formation rate density $\mathcal{R}_{\text{IMBH}}$. The models that assume an evolving high redshift galaxy stellar mass function (GSMF) from [Chrušlińska et al. \(2025\)](#) show a broader $\mathcal{R}_{\text{IMBH}}$ peak extending from the cosmic noon to $z \sim 5-6$ due to increased low metallicity star formation in the models at higher redshifts. The difference between the bracketing low and high models is approximately an order of magnitude.

In Fig. D1, we compare three variations of the SFRD(Z) from [Chrušlińska et al. \(2025\)](#) leading to low, intermediate (model mid) or high fraction of star formation at low metallicities. The 'mid' SFRD(Z) model is identical to the 'example variation' from [Chrušlińska et al. 2025](#). The low (high) model variation adopts (i) the galaxy main sequence from [Popesso et al. \(2023\)](#) with a logarithmic slope $a_{\text{SFR}} = 1$ ($a_{\text{SFR}} = 0.8$) at low masses, (ii) the galaxy mass - gas-phase (oxygen) metallicity relation with a high (low) normalization (as given in Table C.1 in [Chrušlińska et al. 2025](#)), (iii) the oxygen-to-iron abundance ratio - specific SFR relation of galaxies following the "fast" ("slow") iron enrichment scenario from [Chrušlińska et al. 2025](#), (iv) fixed (evolving) fundamental metallicity relation at redshift > 3 and (v) negligible contribution of starbursts. We additionally compare variations of the low and high models with and without the redshift evolution of the GSMF slope. The high model variant without the GSMF slope evolution was used in our estimates throughout Section 6. The GSMF slope evolution affects the shape of the $\mathcal{R}_{\text{IMBH}}$ above $z \gtrsim 2$, and results in a plateau in the $\mathcal{R}_{\text{IMBH}}$ that extends up to $z \sim 6$. At $z = 10$, the SFRD models with an evolving GSMF slope result in \sim an order of magnitude higher $\mathcal{R}_{\text{IMBH}}$. Meanwhile, the difference between the low and high models mainly affects the normalization of the $\mathcal{R}_{\text{IMBH}}$ but not its overall shape. In all examined SFRD models the majority of IMBH formation still occurs at metallicities below $Z \sim 0.10 Z_{\odot}-0.20 Z_{\odot}$. Finally, we show in Fig. D2 that in the all explored SFRD(Z) models with various assumptions about the GSMF evolution as well as in cluster birth radius evolution models 50% of the IMBHs still form at redshifts below $z \lesssim 1.5-3$.

This paper has been typeset from a $\text{\TeX}/\text{\LaTeX}$ file prepared by the author.

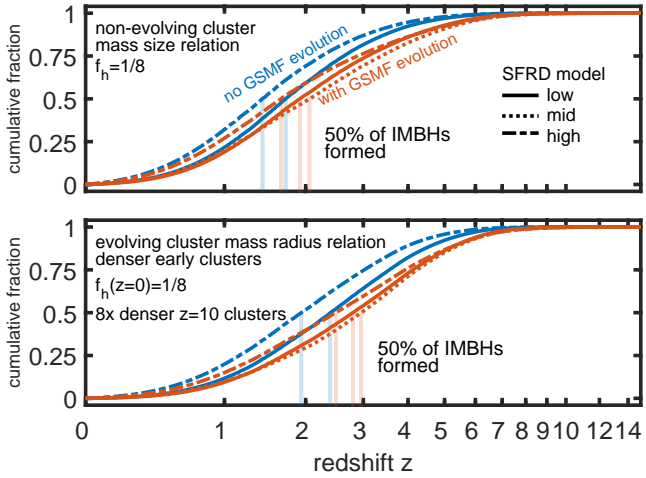


Figure D2. The cumulative fraction of IMBHs formed below redshift z . The different lines correspond to SFRD(Z) model variations. In all explored models 50% of IMBHs form below redshifts $z \lesssim 1.5$ –3.